

UCSF

UC San Francisco Electronic Theses and Dissertations

Title

EPIGENETIC CONTROL OF NEURAL CREST DEVELOPMENT AND NEURAL CREST DERIVED TUMORS

Permalink

<https://escholarship.org/uc/item/40f4d016>

Author

Casey-Clyde, Timothy

Publication Date

2024

Supplemental Material

<https://escholarship.org/uc/item/40f4d016#supplemental>

Peer reviewed|Thesis/dissertation

Epigenetic control of neural crest development and neural crest derived tumors

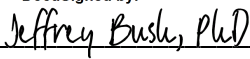
by
Timothy Casey-Clyde

DISSERTATION
Submitted in partial satisfaction of the requirements for degree of
DOCTOR OF PHILOSOPHY

in
Cell Biology

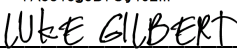
in the
GRADUATE DIVISION
of the
UNIVERSITY OF CALIFORNIA, SAN FRANCISCO

Approved:

DocuSigned by:

367536768C42487... Jeffrey Bush, PhD
Chair

DocuSigned by:

DocuSigned by:402... David Raleigh


71F73C69F83C48B... LUKE GILBERT

Committee Members

Copyright 2024

by

Timothy Casey-Clyde

This dissertation is dedicated to:

My mom, Dr. Louise Casey, and my dad, Dr. Robin Clyde,
who taught me a life dedicated to learning is a life full of joy,
my sister, Dr. Lauren Casey-Clyde, and my brother, Dr. Andrew Casey-Clyde,
who taught me to find the meaning in the journey,
and
my community in San Francisco who made this city home.

Acknowledgments

I would first like to thank my mentor Dr. David Raleigh. David is beyond his years in his ability to wear many hats: that of a brilliant scientist, lab-head, project manager, publishing extraordinaire, advocate for patients, father, and friend. However, what I will remember most about David, is his keen ability to adapt his mentoring style in a personalized way that connected with me and allowed me to develop as a researcher. David liked to use the phrase “it’s time to cook with gas” during periods when it was time to bring multiple experiments to the finish line. As someone who loves cooking outside of lab, this phrase was always motivating, and exemplified David’s keen ability to mentor in an individualized manner. His mentoring style, grounded in patience, understanding, thoughtfulness, and equity, has been truly invaluable. We have shared countless illuminating one-on-ones, memorable lab meetings, conferences, lab outings, and cold brews on the 4th floor Helen Diller balcony. I will forever be grateful for David’s unwavering commitment to my scientific training and personal and professional growth over the last five years.

I will never forget March of 2020. In the throes of the infamous TETRAD class “BioReg” and the final week of my rotation in the Raleigh lab, the COVID-19 pandemic struck prompting Mayor London Breed to shut down San Francisco and deploy a shelter in place order. Sitting in my white Jeep Liberty in the Mission Bay parking lot, I received an email from David: “I’ve gotta admit, Tim: a lab rotation abbreviated by a global pandemic is not something I was anticipating.” Feeling deflated and scared, I wondered when or if I would ever start my PhD research. Amidst months of lockdown, scheduled lab time, constant masking and social distancing, and too many zoom meetings to count,

we slowly returned to a new normal, with all of us forever changed. I am *not* thanking the once in a generation COVID-19 pandemic but would be remiss to not acknowledge the tenacity that lab workers at UCSF demonstrated to keep the labs operating and the science moving forward.

I extend my deepest gratitude to the many individuals who have contributed to my journey in the Raleigh lab. First, I thank Charlotte Eaton for her pivotal role during my rotation and continued mentorship over the years. It was an honor to be back-to-back bay mates and I will be forever grateful for our morning banter and memories we made outside of lab. I am grateful to Kyounghee Seo for her indispensable support in maintaining lab operations and her keen sense of humor. Special thanks to Sydney Lastella and Zora Arum for their meticulous and tireless work in genotyping thousands (literally, thousands!) of my mice.

I appreciate Abrar Choudhury, Vikas Daggubati, Addie Cady, and Kyla Foster for their camaraderie and support as fellow PhD students navigating life together in the Raleigh lab. Special shoutout to Vikas, for his unwavering friendship over the years. Shoutout to Kyla as well, for bringing so much joy to the culture of the lab.

John Liu took me under his wing on the schwannoma project and taught me everything I know today about cancer functional genomics and CRISPRi tools. I am so grateful for his generous collaboration and advocacy. Harish Vasudevan played a crucial role in the conception of my thesis work and generously provided guidance on mouse genetics and cancer biology. This thesis would not have been possible without the mentorship of John and Harish.

I extend gratitude to my thesis committee, Jeff Bush and Luke Gilbert. Jeff provided invaluable expertise on all things neural crest, craniofacial biology, and embryology techniques. My manuscript greatly benefited from the collaboration with Dr. Bush and his lab.. Luke provided thoughtful contributions to the genomics aspects of the thesis, as well as fantastic life advice to me as a budding scientist.

The Laboratory Animal Resource Center (LARC) and the dedicated staff at the Helen Diller mouse house have been instrumental in maintaining our mouse colony and thoughtfully caring for the wellbeing and health of my mice. Thank you to the thousands of mice who sacrificed their lives for my research and the betterment of science. We are forever indebted to our model organisms.

Lastly, I extend my heartfelt appreciation to my family. My mother has been my steadfast champion throughout my life, but especially during the past five years, supporting me through numerous challenges. She fielded the countless times I called her and broke down thinking I would not make it through my first year at UCSF, or the third-year slump, or the paper writing, or other challenges. She always told me to keep my head up and keep at it, and she was right! Last but certainly not least, I would be no where without my extraordinary siblings. My twin Lauren and brother Andrew, who embarked on their doctoral studies the same year as I did, have been a constant source of inspiration. Navigating the ups and downs of graduate school with them has been a remarkable journey. I can't wait to go through life with them!

Contributions

Dr. David Raleigh conceived and managed the presented studies with significant input from Dr. John Liu and Dr. Harish Vasudevan. John Liu led the work presented in Chapter 3 (PMID: 38216587). Dr. Charlotte Eaton provided invaluable mentorship during my rotation and technical advice over many years. Kyla Foster was instrumental in her rotation in our successful completion of the snARC-seq project described in Chapter 3. Juan Antonio Camarena was pivotal in performing echocardiograms and microCT of mouse embryos described in Chapter 2. Yoon-Gu Jang provided help with microCT segmentation and acted as my liaison to the Bush lab, which was critical for success in the experiments described in Chapter 2. This thesis could not have been done without the help of Kyounghee Seo, who ensured that a steady stream of lab consumables and reagents was always available. Dr. Jeff Bush and Dr. Luke Gilbert provided thoughtful and insightful help as part of my thesis committee. Finally, I want to acknowledge the administrators of the TETRAD graduate program, Helen Diller Cancer Research Center, and UCSF.

“The only interesting thing about vertebrates is the neural crest”

-overheard by Peter Thorogood

EPIGENETIC CONTROL OF CRANIOFACIAL DEVELOPMENT FROM THE NEURAL CREST AND NEURAL CREST DERIVED TUMORS

Timothy Casey-Clyde

ABSTRACT

The neural crest is a multipotent transient cell population that migrates, proliferates, and differentiates in vertebrate embryogenesis and gives rise to a cornucopia of tissue derivatives such as craniofacial bone and cartilage, peripheral nerves, and glia. Congenital malformations including cleft palate and craniosynostosis arise from aberrant development of cranial neural crest cells and their derivatives. Neural crest derived tumors of Schwann cell lineages can arise from single genomic hits in the form of *NF2* loss. Considering the low genomic burden of many neural crest derived tumors, we hypothesized that epigenetic regulators, which normally specify cell lineages and maintain cell fates in embryonic development, are mis-regulated in adult neural crest derived tissues, contributing to tumorigenesis and differential tumor radiation responses.

Here we use mouse genetics and single cell sequencing to investigate how PRC2, a histone methyltransferase broadly involved in gene repression and maintenance of pluripotency in development, is involved in epigenetic control of post-otic neural crest derivatives. We identified *Eed*, a PRC2 core subunit, as a potent regulator of craniofacial development. *Eed* deletion in post-migratory neural crest cells was perinatal lethal and knockout embryos presented with severe craniofacial abnormalities consistent with impaired differentiation of osteoblast derivatives. Using targeted primary cell culture gene expression analysis and unbiased scRNA-seq, we discovered changes in transcription factors involved in the proliferation and differentiation of neural crest derivatives including

loss of Sox transcription factors and increase in Hox genes. Strikingly, we found an expansion of undifferentiated mesenchymal stem cells and decrease in differentiated osteoblast cells, indicating *Eed* controls proper differentiation of mesenchymal derivatives that comprise craniofacial structures. Taken together, we establish the embryonic, cellular, and molecular consequences of *Eed* loss in neural crest derived craniofacial tissues.

Next, we investigated more broadly how epigenetic regulation contributes to cancer of neural crest derived cells including the tumorigenesis of schwannomas and schwannoma radiation responses. Using bulk and single-cell bioinformatics, functional genomic approaches, and mechanistic validation, we discovered schwannomas comprise 2 molecular subgroups marked by activation of neural crest signaling pathways or enrichment of immune cells in response to radiotherapy. CRISPRi radiation screening in human schwannoma cells identified the lysine demethylases KDM1A and KDM5C as drivers of radioresistance or radiosensitivity, respectively. Lastly, we integrated single-nuclei ATAC, RNA, and CRISPRi perturbation to identify chromatin accessibility motifs that drive schwannoma cell state evolution and radiation responses.

Table of Contents

Chapter 1: Introduction

A brief history of the neural crest.....	1
References.....	4
Transcriptional control of neural crest development.....	6
Epigenetic control of neural crest development.....	8
References.....	13

Chapter 2: Eed controls craniofacial osteoblast differentiation and mesenchymal proliferation from the neural crest

Introduction.....	20
Methods.....	22
Results.....	28
Discussion.....	35
References.....	49

Chapter 3: Epigenetic reprogramming shapes the cellular landscape of schwannoma

Introduction.....	59
Methods.....	60
Results.....	70
Discussion.....	76
References.....	85

List of Figures

Fig. 1. <i>Sox10-Cre Eed^{F1/F1}</i> embryos develop craniofacial malformations <i>in utero</i> ...	38
Fig. 2. <i>Eed</i> is required for craniofacial skeletal development from the neural crest	39
Fig. 3. <i>Eed</i> regulates craniofacial differentiation and proliferation from the neural crest.....	40
Fig. 4. <i>Eed</i> regulates craniofacial mesenchymal stem cell, osteoblast, and proliferating mesenchymal cell fate from the neural crest.....	41
Supplementary Fig. 1. <i>Sox10-Cre Eed^{F1/F1}</i> embryos develop significant craniofacial malformations <i>in utero</i>	42
Supplementary Fig. 2. <i>Sox10-Cre Eed^{F1/F1}</i> embryos develop subtle cardiac malformations <i>in utero</i>	43
Supplementary Fig. 3. <i>Sox10-Cre Eed^{F1/F1}</i> embryos develop significant craniofacial mesenchymal differentiation phenotypes and subtle apoptotic phenotypes <i>in utero</i> .	44
Supplementary Fig 4. <i>Eed</i> regulates craniofacial differentiation and proliferation <i>in vivo</i> and in primary cell cultures.....	45
Supplementary Fig. 5. Cell clusters from single-cell RNA sequencing of E12.5 <i>Sox10-Cre Eed^{F1/WT}</i> or <i>Sox10-Cre Eed^{F1/F1}</i> heads.....	46
Supplementary Fig. 6. Cell cluster marker genes from single-cell RNA sequencing of E12.5 <i>Sox10-Cre Eed^{F1/WT}</i> or <i>Sox10-Cre Eed^{F1/F1}</i> heads.....	47
Supplementary Fig. 7. Single-cell transcriptome differential expression analyses among mesenchymal cell clusters.....	48
Fig. 5. An integrated model of schwannoma tumorigenesis and epigenetic reprogramming in response to treatment.....	78

Fig. 6. Epigenetic regulators reprogram schwannoma cells and drive immune cell infiltration in response to radiotherapy.....	79
Fig. 7. Single-nuclei ATAC, RNA, and CRISPRi perturbation sequencing identify integrated genomic mechanisms driving schwannoma cell state evolution.....	81
Supplementary Fig. 8. Genome-wide CRISPRi screens reveal regulators of schwannoma cell radiotherapy responses.....	83
Supplementary Fig. 9. Proteomic and targeted metabolic mass spectrometry of schwannoma cells.....	84

CHAPTER 1

Introduction: A brief history of the neural crest

The neural crest constitutes an evolutionarily conserved multipotent cell population that is exclusive to vertebrates and contributes to remarkable cell and tissue diversity during embryogenesis. The neural crest was discovered in 1868 by embryologist Wilhelm His who observed a band of cells in chick embryos that lay between the neural tube and epidermal ectoderm in neurula-stage chick embryos¹. His's original name for this group of cells responsible for forming spinal and cranial ganglia, "Zwischenstrang, the intermediate cord", was replaced in 1879 by Arthur Marshall, who originally referred to these cells as the neural ridge due to their proximity to the neural tube, then finally coined the term neural crest, which scientists still use today². By the 1890s, scientists accepted that neural crest cells were the cellular progenitors of spinal and cranial ganglia, but it wasn't until pioneering work led by Julia Platt, who used *Necturus maculosus* to demonstrate that the craniofacial cartilage and teeth were of ectodermal neural crest origin, as opposed to mesodermal origin, which was commonly believed under the prevailing germ-layer theory³⁻⁵. Developmental biologists of the early 20th century finally established the neural crest as a highly migratory transient population capable of developing into ectodermal mesenchyme and subsequent tissue derivatives. Landacre opportunistically used the pigmented neural crest cells in salamander to observe the movement of a continuous sheet of ventrally migrating neural crest cells that erupts out of the neural tube and colonize arches of the face ⁶. Stone used transplantation experiments in *Ambystoma maculatum* and *Rana palustris* to conclusively demonstrate that cranial neural crest cells develop cartilage, loose connective tissues of the head, and

the hyobranchial skeleton⁷⁻⁸. The 1940s revealed in the publication of seminal studies by Hörstadius and Spellman who vital stained portions of *Ambystoma mexicanum* neural folds to track cranial migration and performed extirpation or transplantation experiments to prove that neural crest forms the cranial skeleton, among other structures⁹. Hörstadius advanced techniques in tracking and grafting neural crest tissues and his 1950 monograph is considered one of the most seminal works in the history of neural crest research¹⁰. In 1947 De Beer expanded on the field through experiments showing neural crest cells colonize the pharyngeal arches and differentiate into odontoblasts, and likely dermal bone¹¹. He finally, after the idea was first set forth by Julia Platt 50 years earlier, called for an abandonment of classical germ theory because sufficient evidence supported the invariable correlation between germ layers and their presumptive embryonic structures, which the scientific community accepted.

“Looking at it from the point of view of causal embryology, there can be no doubt that the germ-layer theory was misconceived in its attempt to provide an embryological criterion of homology, and in its assumption that the fates of the germ layers were universally equal and limited.” – De Beer 1947

The 1960s saw several classic experiments which led to the defining of neural crest fates and understanding of migration patterns. Weston and Johnston pioneered *in vivo* tritiated thymidine labeling (today replaced by BrdU) and grafting experiments in chick embryos to radioautographically assess early migration of neural crest cells. He found that the dorsal-ventral orientation of the neural tube is crucial for initial migration into the somatic mesenchyme, and that these cells appear in delimited directional streams as they migrate away from the neural tube¹²⁻¹³. Weston also confirmed that Schwann

cells and melanoblasts are of neural crest origin, with melanoblasts resulting from the ventral migration of cells in the mesenchyme adjacent to the neural tube while Johnston showed that neural crest cells do not develop into nervous system tissues of the brain. In the 1970s, Le Douarin pioneered the use of quail-chick chimeras and Fielgen staining to delineate origin cells to demonstrate the multipotency of neural crest cells and track individual migrating streams of neural crest lineages ¹⁴. Le Douarin published seminal textbooks on the neural crest in 1982 and 1999 and remains one of the world's premier experts in the field ¹⁵⁻¹⁶. In 1983, Gans and Northcutt published a seminal paper on the "new head" hypothesis. The "new head" hypothesis suggests that the development and intricacy of the vertebrate head resulted from the emergence of migratory cranial neural crest cells and cranial placodes. These new cell types facilitated the construction of the craniofacial skeleton and a unique sensory system, which then enabled the anterior neuroepithelium to expand and form the vertebrate brain. The morphological features originating from the neural crest and cranial placodes also supported a shift from the mainly filter-feeding behavior observed in invertebrate chordates to the active predatory lifestyle of vertebrates ¹⁷. The end of the 20th century brought the advent of molecular detection techniques like *in situ* hybridization and immunohistochemistry which led to the discovery of the neural crest gene regulatory network (GRN) which has enabled our knowledge of spatial and temporal transcriptional control of neural crest development. Finally, the advent of genomics, single-cell technology, and pooled screening is charging the field through the 21st century.

References

1. His W. *Untersuchungen über die erste Anlage des Wirbeltierleibes*. Leipzig: Die erste Entwicklung des Hühnchens im Ei. FCW Vogel; 1868.
2. Hall BK. The neural crest and neural crest cells: discovery and significance for theories of embryonic organization. *J Biosci*. 2008 Dec;33(5):781-93. doi: 10.1007/s12038-008-0098-4. PMID: 19179766.
3. Platt, Julia B. "Ectodermic Origin of the Cartilages of the Head." *Anatomischer Anzeiger* [Anatomical Gazette]. (1893) 8: 506–9. <http://biodiversitylibrary.org/page/11789484> (Accessed March 5, 2017).
4. Ramirez, Karina, "Julia Barlow Platt's Embryological Observations on Salamanders' Cartilage (1893)". Embryo Project Encyclopedia (2017-03-06). ISSN: 1940-5030 <https://hdl.handle.net/10776/11437>
5. Platt J B 1897 The development of the cartilaginous skull and of the branchial and hypoglossal musculature in *Necturus*; *Morphol. Jb.* **25** 377–464
6. Landacre, F.L., 1921. The fate of the neural crest in the head of Urodeles. *J. Comp. Neurol.* 33, 1–43.
7. Stone L S 1926 Further experiments on the extirpation and transplantation of mesectoderm in *Amblystoma punctatum*; *J. Exp. Zool.* **44** 95–131
8. Stone LS. Experiments showing the role of migrating neural crest (mesectoderm) in the formation of head skeleton and loose connective tissue in *Rana palustris*. *Wilhelm Roux Arch Entwickl Mech Org.* 1929 Jun;118(1):40-77. doi: 10.1007/BF02108871. PMID: 28354182.

9. Horstadius, Sven Otto, and Sven Sellman. Experimentelle Untersuchungen über die Determination des knorpeligen Kopfskelletes bei Urodelen. Almquist & Wiksell, 1946.
10. Hörstadius S 1950 *The neural crest: Its properties and derivatives in the light of experimental research* (Oxford: Oxford University Press)
11. de Beer G R 1947 The differentiation of neural crest cells into visceral cartilages and odontoblasts in *Amblystoma*, and a re-examination of the germ-layer theory; *Proc. R. Soc. London* **B134** 377–398
12. Weston JA. A radioautographic analysis of the migration and localization of trunk neural crest cells in the chick. *Dev Biol.* 1963 Jun;6:279-310. doi: 10.1016/0012-1606(63)90016-2. PMID: 14000137.
13. Johnston M C 1966 A radioautographic study of the migration and fate of cranial neural crest cells in the chick embryo; *Anat. Rec.* **156** 143–156
14. Le Douarin N & Teillet M. "Experimental analysis of the migration and differentiation of neuroblasts of the autonomic nervous system and of neuroectodermal mesenchymal derivatives using a biological cell marking technique." *Dev. Biol.* v. 41, pp. 162–184 (1974).
15. Le Douarin N M 1982 *The neural crest* (Cambridge: Cambridge University Press)
16. Le Douarin N M and Kalcheim C 1999 *The neural crest* 2nd edition (Cambridge: Cambridge University Press)
17. Gans, C. and R. G. Northcutt (1983). "Neural crest and the origin of vertebrates: A new head." *Science* 220(4594): 268–274.

Transcriptional control of neural crest development

The neural crest is a multipotent transient cell population that gives rise to a variety of derivatives including components of the peripheral nervous system, cartilage and bone of the craniofacial skeleton, melanocytes, and smooth muscle¹⁻². Neural crest cells are induced during gastrulation at the neural plate border between non neural ectoderm and the neural tube. The neural plate border is specified by a module of transcription factors including *Msx1/2*, *Pax 3/7* and *Zic1*¹⁴. Wnt and FGF signaling, as well as BMP molecules like BMP4/7 are thought to contribute to induction of the neural crest and formation of premigratory neural crest precursors⁶⁻¹⁰. Transcription factors including *Snail2* and *Sox2/3* also mark early induction of neural crest fate at the neural plate border¹¹⁻¹². In *Xenopus*, ectopic expression of Wnt ligands and modulation of BMP signaling can induce neural plate border and neural crest marker expression²³⁻²⁴. Wnt, BMP, and Notch signaling pathways are involved in the activation and maintenance of transcription factor expression dubbed “neural crest specifiers” which eventually activate downstream sequences of neural crest development like epithelial to mesenchymal transition and migration²². To that end, mice lacking BMP receptors in neural crest derived lineages have broad craniofacial, pharyngeal, and cardiac defects, supporting the hypothesis that BMP is responsible for maintenance of neural crest marker expression rather than initial induction of expression²⁵. In a fascinating experiment, FGF4 soaked beads were grafted in chick nonneural ectoderm, which activated expression of *Bmp4* and *Wnt8*, indicating FGF signaling is vital for early induction of the neural crest without contribution from surrounding mesoderm²⁶. Additionally, Notch signaling is required for activation and

maintenance of *Bmp4* expression at the epidermis-neural plate boundary resulting in spatially controlled induction of neural crest cells in chick embryos ²⁷.

Specification of neural crest cells is marked by expression of canonical gene markers including *FoxD3* and *Sox10* and following neural tube closure, these cells delaminate, undergo epithelial-to-mesenchymal transition and shift into a migratory cell population ³⁻⁵. Delamination, the process of the neural crest physically separating from the neuroectoderm, occurs through a complex interplay of signaling molecules including BMP and Noggin ¹³. Additionally, *Snail1* is thought to induce the expression of *Slug*, *Foxd3* and *Ets1* as neural crest cells become less adhesive and more motile ¹⁵⁻¹⁶. After delamination, cranial neural crest cells begin moving as a continuous sheet of migrating cells between the space between the epidermal and mesodermal layers ¹⁸. The cells then begin migrating as distinct streams along ventromedial or dorsolateral pathways. Eph/Ephrin signaling, among other signaling modules like Sema3, is linked to the correct segregation of the neural crest into distinct migratory streams ¹⁷. Remarkably, neural crest cells maintain contact with one another throughout the duration of migration and use contact inhibition of locomotion mechanisms to migrate from high to low density areas in a highly coordinated and directional manner ¹⁹. N cadherin and the Wnt/PCP pathway are essential players in neural crest migration and loss of these components results in ectopic protrusions of cell streams. With respect to chemotaxis modes of migration, FGF and VEGF signaling, as well as *Sdf1*, are thought to be specifically involved in neural crest lineages ²⁰⁻²¹. *Sox10* is expressed in cranial neural crest cells colonizing the pharyngeal arches but turns off in the differentiated ectomesenchymal derivatives of cranial bone or cartilage. Conversely, *Sox9* is expressed in an undifferentiated state of the neural

crest and later in the pharyngeal arches marking future chondrogenic progenitors of the cranial skeleton and various cardiac tissues. Anterior hox genes are also involved in neural crest patterning and migration and display striking patterns in the rhombencephalic neural crest and dictate the positional identity of the pharyngeal arches ²⁸⁻²⁹. Once a migratory neural crest cell settles into its final tissue position, a cascade of differentiation expression modules turn on, and early neural crest induction markers turn off, enabling terminal differentiation of neural crest derivatives into respective tissue identities.

Epigenetic control of neural crest development

While the signal transduction and transcriptional control of neural crest development (the gene regulatory network) has been studied for decades, epigenetic regulation of neural crest cell induction, migration, and differentiation is a relatively new field and has only recently been advanced due to the advent of chromatin profiling technologies like ATAC-seq, ChIP-seq, and transgenic animal models. The epigenome is responsible for changes in gene expression without modifying the underlying DNA sequence. This regulation comes from changes in higher order chromatin structure due to DNA and histone modifications such as methylation, acetylation, and phosphorylation. Chromatin modifications such as H3K4me3 (methylation) and H3K27ac (acetylation) are thought to be involved in the open conformation of chromatin, and enhancement of gene expression, while H3K9me3 and H3K27me3 are thought to be responsible for closed chromatin and silencing of gene expression ³⁰.

Cell type specification, lineage commitment, and maintenance of pluripotency relies on epigenetic regulatory mechanisms including gene silencing via DNA methylation occurring at CpG islands in the genome which tend to lie at the promoter region of genes

³¹. The neural crest relies heavily on these mechanisms to specify neural crest lineages and maintain cell state identity in its cornucopia of tissue derivatives. For example, the maintenance DNA methyltransferase *Dnmt3a* is highly expressed in development and works to repress expression of neural-like *Sox2* and *Sox3* in the dorsal neural fold and subsequently enable activation of neural crest transcription factor expression including *FoxD3*, *Snail2*, and *Sox10* ³². Additionally, the *de novo* DNA methyltransferase *Dnmt3B* is required for development of craniofacial structures in zebrafish, but intriguingly not required for mouse development when *Dnmt3b* was deleted using a *Wnt1-Cre* or *Sox10-Cre* driver ³³⁻³⁴. In humans, *Dnmt3b* is thought to promote activation of transcription factors including *FoxD3*, *Snail2*, *Pax3*, *Pax7*, and *Sox10* ³⁵.

Histone modifications, often in the form of methylation or acetylation of histone tails, is an additional mechanism of epigenetic regulation of gene expression in neural crest development. Histone methyltransferases and demethylases are important regulators of chromatin confirmation, with marks such as H3K4me3 at promoters and H3K36me3 at gene bodies being associated with transcriptionally open chromatin ³⁶. Conversely, H3K27me3, a mark of closed chromatin and gene repression, is catalyzed by the histone methyltransferase complexes PRC1 and PRC2 ³⁷. In the developing neural tube, chromatin is decorated with H3K9me3 marks in dorsally situated cells relative to ventral neural cells, and this activity is thought to be regulated by *JmjD2A*. Neural crest specification is regulated by *JmjD2A* by maintaining expression of neural crest transcription factors including *FoxD3*, *Snail2*, and *Sox10* through direct interaction of *JmjD2A* with promoter regions of transcription factors. Additionally, the transcription factor *MxB*, which is required for proper craniofacial development in zebrafish and other

vertebrates, is regulated by the histone demethylase *Phf8* through demethylation of H3K9me1 at transcription start sites ^{24,39}.

Enhancer activity is associated with histone acetylation, including H3K27ac marks on active enhancers ⁴⁰. Neural crest development appears to be uniquely susceptible to histone acetylation changes, as dysregulation of acetylation results in broad defects in specification, migration, and differentiation. In chick embryos, histone deacetylase inhibitors promote neural crest specification via induction of markers like *Sox10*, *Sox9*, and *Bmp4* ⁴¹. In premigratory neural crest cells, *Cad6B* is repressed by the neural crest transcription factors *Snail2* via *PHD12-Snail2* recruitment of the Sin3A histone deacetylase complex, resulting in a loss of adhesion and promotion of epithelial-to-mesenchymal transition ⁴². HDAC1 appears to be heavily involved of differentiation of neural crest derivatives. In zebrafish, HDAC1 represses expression of *FoxD3*, which in turn increases MITFa to drive proper differentiation, migration, and differentiation of melanocytes ⁴³. In HDAC1-deficient zebrafish, branchial arch specification is incomplete and chondrocyte precursors fail differentiate correctly, leading to cartilage defects of the craniofacial skeleton ⁴⁴. HDAC4 is additionally required for craniofacial morphogenesis, and zebrafish treated with HDAC4 inhibitors fail to develop palatal skeletal precursor cells resulting in cleft palate and craniofacial shortening ⁴⁵. Finally, HDAC8 regulates expression of the homeobox transcription factors *Otx2* and *Lhx1* to direct skull morphogenesis in mice⁴⁶.

ATP dependent chromatin remodelers use the power of ATP hydrolysis to physically change the structure of chromatin and create pockets of open chromatin for transcription factors to access. One such remodeler, *CDH7* interacts with the SWI/SNF

complex PBAF and directs enhancer activity of *Sox9* and *Twist1* to drive neural crest specification. Mutations in *CDH7* result in CHARGE (coloboma, heart, atresia, restricted growth, genital defects, and ear abnormalities) syndrome in humans, a rare genetic condition marked by broad craniofacial abnormalities, heart defects, and peripheral nerve dysfunction which is recapitulated in mouse and zebrafish models of *CDH7* deficiency⁴⁷⁻⁴⁸. SWI/SNF is further involved in neural crest induction through *Brg1*, and ATP dependent regulation of *Snail2* and other transcription factors⁴⁹. The transcription factor WSFT, a core component in ATP dependent chromatin remodelers including WINAC and WICH, is highly expressed in branchial arches and controls expression of *Snail2* in migratory neural crest cells⁵⁰. In addition to the SWI/SNF complex, the Polycomb repressive complexes act as major regulator of gene repression in neural crest development. PRC catalyzes H3K27me3 to broadly control development including specification of cell identity, maintenance of pluripotency, and commitment to differentiated cell states⁵¹. EZH2, the catalytic subunit of PRC2 is responsible for repression of Hox gene clusters, and deletion of *Ezh2* in pre-migratory neural crest cells results in broad craniofacial and skeletal defects⁵². *Aebp*, another component of PRC2, is thought to directly regulate *Sox10* expression and mice with heterozygous mutations of *Aebp2* exhibit phenotypes consistent with Hirschsprung's disease and Waardenburg syndrome, two congenital syndromes resulting from neural crest defects⁵³. Craniofacial development is also impacted by loss of the PRC1 component *Ring1b/Rnf2*, and *Ring1b* deficient zebrafish fail to differentiate chondrocytes into cranial cartilage and bone⁵⁴. Taken together, a cornucopia of epigenetic regulators is broadly responsible for all aspects of neural crest development, including induction, specification, migration, and

differentiation. In Chapter 2 of this thesis, *Eed*, a core subunit of the H3K27me3 histone methyltransferase PRC2, is investigated using a Sox10-Cre driver targeting migratory neural crest cells and the impact of *Eed* deletion is evaluated at the tissue and single cell level. In Chapter 3 of this thesis, bulk and single-cell bioinformatics, functional genomic, and mechanistic approaches are deployed to investigate how epigenetic regulators control cell states and immune microenvironment responses in neural crest derived peripheral nervous system tumors.

1.5 References

1. Bronner ME, LaBonne C. Preface: the neural crest--from stem cell formation to migration and differentiation. *Dev Biol.* 2012 Jun 1;366(1):1. doi: 10.1016/j.ydbio.2012.03.011. Epub 2012 Mar 15. PMID: 22459578.
2. Sauka-Spengler T, Bronner M. Snapshot: neural crest. *Cell.* 2010 Oct 29;143(3):486-486.e1. doi: 10.1016/j.cell.2010.10.025. PMID: 21029868.
3. Simões-Costa M, Bronner ME. Establishing neural crest identity: a gene regulatory recipe. *Development.* 2015 Jan 15;142(2):242-57. doi: 10.1242/dev.105445. PMID: 25564621; PMCID: PMC4302844.
4. Labosky PA, Kaestner KH. The winged helix transcription factor Hfh2 is expressed in neural crest and spinal cord during mouse development. *Mech Dev.* 1998 Aug;76(1-2):185-90. doi: 10.1016/s0925-4773(98)00105-1. PMID: 9767163.
5. Southard-Smith EM, Kos L, Pavan WJ. Sox10 mutation disrupts neural crest development in Dom Hirschsprung mouse model. *Nat Genet.* 1998 Jan;18(1):60-4. doi: 10.1038/ng0198-60. PMID: 9425902.
6. A. Streit, C.D. Stern Establishment and maintenance of the border of the neural plate and in the chick: involvement of FGF and BMP activity *Mech. Dev.*, 82 (1999), pp. 51-66
7. K.F. Liem Jr., G. Tremml, H. Roelink, T. Jessell Dorsal differentiation of neural plate cells induced by BMP-mediated signals from epidermal ectoderm *Cell*, 82 (1995), pp. 969-979
8. M. Ikeya, S.M.K. Lee, J.E. Johnson, A.P. McMahon, S. Takada

9. Wnt signalling required for expansion of neural crest and CNS progenitors
Nature, 389 (1997), pp. 966-970
10. R.I. Dorsky, R.T. Moon, D.W. Raible Control of neural crest fate by the Wnt signalling pathway Nature, 396 (1998), pp. 370-373
11. M.A. Nieto, M.G. Sargent, D.G. Wilkinson, J. Cooke Control of cell behaviour during vertebrate development by Slug, a zinc finger gene Science, 264 (1994), pp. 835-839
12. C. LaBonne, M. Bronner-Fraser Snail-related transcriptional repressors are required in *Xenopus* both for induction of the neural crest and its subsequent migration Dev. Biol., 221 (2000), pp. 195-20
13. D. Sela-Donenfeld, C. Kalcheim Regulation of the onset of neural crest migration by coordinated activity of BMP4 and Noggin in the dorsal neural tube Development, 126 (1999), pp. 4749-4762
14. C.S. Hong, J.P. Saint-Jeannet The activity of Pax3 and Zic1 regulates three distinct cell fates at the neural plate border Mol. Biol. Cell, 18 (2007), pp. 2192-2202
15. Aybar MA, Nieto MA, Mayor R. 2003. Snail precedes Slug in the genetic cascade required for the specification and migration of the *Xenopus* neural crest. Development 130:483–94
16. Cheung M, Chaboissier MC, Mynett A, Hirst E, Schedl A, Briscoe J. 2005. The transcriptional control of trunk neural crest induction, survival, and delamination. Dev. Cell 8(2):179–92
17. Kindberg AA, JO. Cellular organization and boundary formation in craniofacial development. Genesis. 2019 Jan;57(1):e23271. doi: 10.1002/dvg.23271. Epub 2019 Jan 12. PMID: 30548771; PMCID: PMC6503678.

18. Szabó A, Mayor R. Mechanisms of Neural Crest Migration. *Annu Rev Genet.* 2018 Nov 23;52:43-63. doi: 10.1146/annurev-genet-120417-031559. PMID: 30476447.
19. Stramer BM, Mayor R. 2016. Mechanisms and in vivo functions of contact inhibition of locomotion. *Nat. Rev. Mol. Cell Biol.* 18:43–55
20. Theveneau E, Marchant L, Kuriyama S, Gull M, Moepps B, et al. 2010. Collective chemotaxis requires contact-dependent cell polarity. *Dev. Cell* 19(1):39–53
21. McLennan R, Teddy JM, Kasemeier-Kulesa JC, Romine MH, Kulesa PM. 2010. Vascular endothelial growth factor (VEGF) regulates cranial neural crest migration in vivo. *Dev. Biol.* 339(1):114–25
22. Prasad MS, Charney RM, García-Castro MI. Specification and formation of the neural crest: Perspectives on lineage segregation. *Genesis.* 2019 Jan;57(1):e23276. doi: 10.1002/dvg.23276. Epub 2019 Jan 15. PMID: 30576078; PMCID: PMC6570420.
23. Hong C-S, Park BY, & Saint-Jeannet J-P (2008). Fgf8a induces neural crest indirectly through the activation of Wnt8 in the paraxial mesoderm. *Development*, 135, 3903–3910.
24. Hong C-S, Park BY, & Saint-JeannMonsoro-Burq A-H, Wang E, & Harland R (2005). Msx1 and Pax3 cooperate to mediate FGF8 and WNT signals during *Xenopus* neural crest induction. *Developmental Cell*, 8, 167–178. 10.1016/j.devcel.2004.12.017t J-P (2008). Fgf8a induces neural crest indirectly through the activation of Wnt8 in the paraxial mesoderm. *Development*, 135, 3903–3910.
25. Dudas M, Sridurongrit S, Nagy A, Okazaki K, & Kaartinen V (2004). Craniofacial defects in mice lacking BMP type I receptor Alk2 in neural crest cells. *Mechanisms of Development*, 121, 173–182. 10.1016/j.mod.2003.12.003

26. Yardley N, & García-Castro MI (2012). FGF signaling transforms nonneural ectoderm into neural crest. *Developmental Biology*, 372, 166–177. 10.1016/j.ydbio.2012.09.006
27. Endo Y, Osumi N, & Wakamatsu Y (2002). Bimodal functions of notch-mediated signaling are involved in neural crest formation during avian ectoderm development. *Development*, 129, 863–873.
28. Prasad MS, Charney RM, García-Castro MI. Specification and formation of the neural crest: Perspectives on lineage segregation. *Genesis*. 2019 Jan;57(1):e23276. doi: 10.1002/dvg.23276. Epub 2019 Jan 15. PMID: 30576078; PMCID: PMC6570420
29. Trainor PA, & Krumlauf R (2000). Patterning the cranial neural crest: Hindbrain segmentation and Hox gene plasticity. *Nature Reviews. Neuroscience*, 1,116–124. 10.1038/35039056
30. Hu N, Strobl-Mazzulla PH, Bronner ME. Epigenetic regulation in neural crest development. *Dev Biol*. 2014 Dec 15;396(2):159-68. doi: 10.1016/j.ydbio.2014.09.034. Epub 2014 Oct 24. PMID: 25446277; PMCID: PMC4261016.
31. T. Chen, E. Li Establishment and maintenance of DNA methylation patterns in mammals *Curr. Top. Microbiol. Immunol.*, 301 (2006), pp. 179-201
32. N. Hu, P. Strobl-Mazzulla, T. Sauka-Spengler, M.E. Bronner DNA methyltransferase3A as a molecular switch mediating the neural tube-to-neural crest fate transition *Genes Dev.*, 26 (2012), pp. 2380-2385
33. K. Rai, I.F. Jafri, S. Chidester, S.R. James, A.R. Karpf, B.R. Cairns, D.A. Jones Dnmt3 and G9a cooperate for tissue-specific development in zebrafish *J. Biol. Chem.*, 285 (2010), pp. 4110-4121

34. B.T. Jacques-Fricke, J. Roffers-Agarwal, L.S. Gammill
DNA methyltransferase 3b is dispensable for mouse neural crest development.
PLoS One, 7 (2012), p. e47794
35. K. Martins-Taylor, D.I. Schroeder, J.M. Lasalle, M. Lalande, R.H. Xu
Role of DNMT3B in the regulation of early neural and neural crest specifiers.
Epigenetics, 7 (2012), pp. 71-81
36. R.C. Akkers, S.J. van Heeringen, U.G. Jacobi, E.M. Janssen-Megens, K.J. Francoijs, H.G. Stunnenberg, G.J. Veenstra A hierarchy of H3K4me3 and H3K27me3 acquisition in spatial gene regulation in *Xenopus* embryos *Dev. Cell*, 17 (2009), pp. 425-434
37. B. Tolhuis, E. de Wit, I. Muijers, H. Teunissen, W. Talhout, B. van Steensel, M. van Lohuizen Genome-wide profiling of PRC1 and PRC2 Polycomb chromatin binding in *Drosophila melanogaster* *Nat. Genet.*, 38 (2006), pp. 694-699
38. P.H. Strobl-Mazzulla, T. Sauka-Spengler, M. Bronner-Fraser Histone demethylase JmjD2A regulates neural crest specification *Dev. Cell*, 19 (2010), pp. 460-468
39. H.H. Qi, M. Sarkissian, G.Q. Hu, Z. Wang, A. Bhattacharjee, D.B. Gordon, M. Gonzales, F. Lan, P.P. Ongusaha, M. Huarte, N.K. Yaghi, H. Lim, B.A. Garcia, L. Brizuela, K. Zhao, T.M. Roberts, Y. Shi Histone H4K20/H3K9 demethylase PHF8 regulates zebrafish brain and craniofacial development *Nature*, 466 (2010), pp. 503-507
40. S. Bonn, R.P. Zinzen, C. Girardot, E.H. Gustafson, A. Perez-Gonzalez, N. Delhomme, Y. Ghavi-Helm, B. Wilczynski, A. Riddell, E.E. Furlong Tissue-specific analysis of chromatin state identifies temporal signatures of enhancer activity during embryonic development *Nat. Genet.*, 44 (2012), pp. 148-156

41. C. Murko, S. Lager, M. Steiner, C. Seiser, C. Schoefer, O. Pusch Histone deacetylase inhibitor Trichostatin A induces neural tube defects and promotes neural crest specification in the chicken neural tube
42. P.H. Strobl-Mazzulla, M.E. Bronner A PHD12-Snail2 repressive complex epigenetically mediates neural crest epithelial-to-mesenchymal transition *J. Cell Biol.*, 198 (2012), pp. 999-1010
43. M.S. Ignatius, H.E. Moose, H.M. El-Hodiri, P.D. Henion colgate/hdac1 repression of foxd3 expression is required to permit mitfa-dependent melanogenesis *Dev. Biol.*, 313 (2008), pp. 568-583
44. M.S. Ignatius, A. Unal Eroglu, S. Malireddy, G. Gallagher, R.M. Nambiar, P.D. Henion Distinct functional and temporal requirements for zebrafish Hdac1 during neural crest-derived craniofacial and peripheral neuron development *PLoS One*, 8 (2013), p. e63218
45. A. DeLaurier, Y. Nakamura, I. Braasch, V. Khanna, H. Kato, S. Wakitani, J.H. Postlethwait, C.B. Kimmel Histone deacetylase-4 is required during early cranial neural crest development for generation of the zebrafish palatal skeleton *BMC Dev. Biol.*, 12 (2012), p. 16
46. M. Haberland, M.H. Mokalled, R.L. Montgomery, E.N. Olson Epigenetic control of skull morphogenesis by histone deacetylase 8 *Genes Dev.*, 23 (2009), pp. 1625-1630
47. R. Bajpai, D.A. Chen, A. Rada-Iglesias, J. Zhang, Y. Xiong, J. Helms, C.P. Chang, Y. Zhao, T. Swigut, J. Wysocka CHD7 cooperates with PBAF to control multipotent neural crest formation *Nature*, 463 (2010), pp. 958-962

48. G.E. Zentner, W.S. Layman, D.M. Martin, P.C. Scacheri Molecular and phenotypic aspects of CHD7 mutation in CHARGE syndrome *Am. J. Med. Genet. Part A*, 152A (2010), pp. 674-686
49. B. Eroglu, G. Wang, N. Tu, X. Sun, N.F. Mivechi Critical role of Brg1 member of the SWI/SNF chromatin remodeling complex during neurogenesis and neural crest induction in zebrafish *Dev. Dyn.*, 235 (2006), pp. 2722-2735
50. K. Yoshimura, H. Kitagawa, R. Fujiki, M. Tanabe, S. Takezawa, I. Takada, I. Yamaoka, M. Yonezawa, T. Kondo, Y. Furutani, H. Yagi, S. Yoshinaga, T. Masuda, T. Fukuda, Y. Yamamoto, K. Ebihara, D.Y. Li, R. Matsuoka, J.K. Takeuchi, T. Matsumoto, S. Kato Distinct function of 2 chromatin remodeling complexes that share a common subunit, Williams syndrome transcription factor (WSTF) *Proc. Natl. Acad. Sci. U.S.A.*, 106 (2009), pp. 9280-9285
51. B. Schuettengruber, D. Chourrout, M. Vervoort, B. Leblanc, G. Cavalli Genome regulation by polycomb and trithorax proteins *Cell*, 128 (2007), pp. 735-745
52. D. Schwarz, S. Varum, M. Zemke, A. Scholer, A. Baggiolini, K. Draganova, H. Koseki, D. Schubeler, L. Sommer Ezh2 is required for neural crest-derived cartilage and bone formation *Development*, 141 (2014), pp. 867-877
53. H. Kim, K. Kang, M.B. Ekram, T.Y. Roh, J. Kim Aebp2 as an epigenetic regulator for neural crest cells *PLoS One*, 6 (2011), p. e25174
54. Y.U. van der Velden, L. Wang, L. Querol Cano, A.P. Haramis The polycomb group protein ring1b/rnf2 is specifically required for craniofacial development *PLoS One*, 8 (2013), p. e73997

CHAPTER 2

Eed controls craniofacial osteoblast differentiation and mesenchymal proliferation from the neural crest

Introduction

The embryonic neural crest is a multipotent progenitor cell population that gives rise to peripheral neurons, glia, Schwann cells, melanocytes, and diverse mesenchymal cells such as osteoblasts, chondrocytes, fibroblasts, cardiac mesenchyme, and cardiomyocytes^{5,64}. Following induction in the neural tube, cranial neural crest cells undergo dorsolateral migration to the pharyngeal arches and differentiate to form craniofacial bones and cartilage⁴⁸. To do so, cranial neural crest cells express transcription factors such as *Sox9*, *Sox10*, and *Twist1* that specify cell fate decisions in derivatives of the neural crest^{1,8}. Pre-migratory neural crest cell specification is partially controlled by the epigenetic regulator Polycomb repressive complex 2 (PRC2), an H3K27 histone methyltransferase that is broadly responsible for chromatin compaction and transcriptional silencing⁴⁴. The catalytic activity of PRC2 is comprised of four core subunits: (1) enhancer of zeste homologue 1 (*Ezh1*) or *Ezh2*, (2) suppressor of zeste 12 (*Suz12*), (3) *RBBP4* or *RBBP7*, and (4) embryonic ectoderm development (*Eed*)⁵⁶. *Eed* binds to H3K27 trimethylation peptides (H3K27me3) and stabilizes *Ezh2* for allosteric activation of methyltransferase activity and on-chromatin spreading of H3K27 methylation. *Eed* is required for stem cell plasticity, pluripotency, and maintaining cell fate decisions, but all PRC2 core subunits are required for embryonic development and loss of any individual subunit is embryonic lethal around gastrulation^{17,54,55}. *Eed* null embryos can initiate endoderm and mesoderm induction but have global anterior-posterior

patterning defects in the primitive streak and genome-wide defects in H3K27 methylation^{17,60,50}.

Ezh2 has been studied in the context of pre-migratory neural crest development. In mice, *Wnt1-Cre Ezh2^{F/FI}* embryos fail to develop skull and mandibular structures due to de-repression of Hox transcription factors in cranial neural crest cells and loss of *Ezh2* in mesenchymal precursor cells causes skeletal defects and craniosynostosis in *Prrx1-Cre Ezh2^{F/FI}* embryos^{16,34,62}. *Ezh2* also regulates neural crest specification in xenopus⁷¹, and *Col2-Cre Eed^{F/FI}* mice have kyphosis and accelerated hypertrophic differentiation due to de-repression of Wnt and TGF- β signaling in chondrocytes⁵⁰. Genetic and molecular interactions allow *Eed* to repress Hox genes to maintain vertebral body identity during mouse development³⁴ but the embryonic, cellular, and molecular consequences of *Eed* activity in craniofacial development are incompletely understood. To address this gap in our understanding of epigenetic mechanisms that may contribute to craniofacial development, we conditionally deleted *Eed* from the migratory neural crest and its derivatives. Our results suggest that *Eed* is required for craniofacial osteoblast differentiation from post-migratory neural crest mesenchymal stem cells, and that *Eed* regulates diverse transcription factor programs that are required for mesenchymal cell proliferation, differentiation, and osteogenesis. More broadly, these data show that *Eed* is required at early post-migratory stages in neural crest progenitors of craniofacial structures.

Methods

Mice

Mice were maintained in the University of California San Francisco (UCSF) pathogen-free animal facility in accordance with the guidelines established by the Institutional Animal Care and Use Committee (IACUC) and Laboratory Animal Resource Center (LARC) protocol AN191840. Mice were maintained in a 70°F, 50% humidity temperature-controlled barrier facilities under a 12-12h light cycle with access to food and water *ad libitum*. *Sox10-Cre* and *Eed^{Fl}* mice were obtained from the Jackson Laboratory (B6;CBA-Tg(Sox10-cre)1Wdr/J, 025807 and B6;129S1-Eed^{tm1Sho}/J, 022727, respectively). The presence of the floxed *Eed* allele was determined through standard PCR genotyping using the following primers: 5' GGGACGTGCTGACATTTTCT 3' (forward) and 5' CTTGGGTGGTTTGGCTAAGA 3' (reverse). To generate embryos at specific time points, *Sox10-Cre^{tg+} Eed^{Fl/WT}* mice were bred overnight with *Eed^{Fl/Fl}* mice. Females were checked for copulation plugs in the morning and the presence of a vaginal plug was designated as E0.5.

Mouse fetal echocardiography

Ultrasound studies were acquired with a Fujifilm Vevo 2100 Imaging system, and instrument specifically designed for lab animal imaging studies. Pregnant females were anesthetized using an isoflurane/oxygen mixture with an isoflurane concentration of 3% during imaging. The pregnancy date (at least 17) was checked to observe the correct development of fetal hearts. Isoflurane was increased until 5% and the abdomen of pregnant females was open surgically to expose the gravid uterus. The number of fetuses was counted, and craniofacial architecture was evaluated for phenotypic confirmation.

Once each fetus was defined as mutant or wild type, echocardiography was performed to evaluate left ventricle anatomy and physiology, including left ventricle size and contractility. Three different measurements were obtained in B and M modes, and functional parameters, including heart rate, fraction shortening, ejection fraction, and left ventricle mass were obtained.

Whole-mount embryo staining

Embryos were stained as previously described (Sandell et al., 2018). In brief, embryos were harvested, and heads were fixed overnight in 4% PFA. Embryos were dehydrated through a methanol series up to 100% before being treated with Dent's bleach (4:1:1, MeOH, DMSO, 30% H₂O₂) for 2hr at 25°C. Embryos were serially rehydrated in methanol up to 25%, washed with PBST, and stained with DAPI solution (1:40,000, Thermo Scientific, cat# 62248) overnight at 4°C. Samples were mounted in low melt agarose for imaging.

Whole-mount skeletal staining

Embryos were stained as previously described (Rigueur and Lyons, 2013). In brief, embryos were dissected in cold PBS and scalded in hot water to facilitate the removal of eyes, skin, and internal organs. Embryos were fixed in 95% ethanol overnight then subsequently incubated in acetone overnight. Embryos were stained with Alcian Blue solution (Newcomer Supply, cat# 1300B) for 8hr, washed in 70% ethanol, and destained in 95% ethanol. Embryos were cleared in 95% ethanol and 1% KOH, and stained in Alizarin red S solution (SCBT, cat#130-22-3) for 4hr. Embryos were stored in glycerol for imaging.

Micro-computed tomography (microCT)

microCT studies were acquired with a Perkin Elmer's Quantum GX2 microCT Imaging system, an instrument specifically designed for lab animal imaging studies. The samples were imaged in Eppendorf tubes containing preservative media, which were placed on the scanning bed and fixed with tape to minimize movement. Acquisition parameters were set as follows: FOV 10mm, acquisition time 14 minutes, current voltage 70KV, amperage 114uA. Each study was composed by a 512x512x512 voxels matrix with a spatial resolution of 0.018mm³. Study reconstruction was based on Feldkamp's method using instrument dedicated software. For image analysis, tridimensional renders were obtained using 3D SLICER software. The threshold range applied for bone segmentation was 300-1400 Hounsfield Units. For the segmentation and visualization of individual frontal bones, cranial base, and mandible, Avizo Lite software (v9.1.1) was used. The threshold range applied was 570-1570 Hounsfield Units.

Cryosectioning and H&E staining

Embryos were fixed in 4% PFA overnight at 4°C and subjected to a sucrose gradient from 15% to 30% before embedding in OCT (Tissue-Tek, cat#4583) and storage at -80°C. Embryos were sectioned at 25µm on a Leica CM1850 cryostat. Slides were immediately subjected to H&E staining as previously described (Cardiff et al., 2014), or stored at -80°C for immunofluorescence.

Immunofluorescence

Immunofluorescence of cryosections was performed on glass slides. Immunofluorescence for primary cells was performed on glass cover slips. Primary cells were fixed in 4% PFA for 10 minutes at room temperature. Antibody incubations were

performed in blocking solution (0.1% Triton X-100, 1% BSA, 10% donkey serum) for 2hr at room temperature or overnight at 4°C. Slides or cover slips were mounted in ProLong Diamond Antifade Mountant (Thermo Scientific, cat# P36965). Primary antibodies used in this study were anti-Sox9 (1:500, Proteintech, cat# 67439-1-Ig), anti-Sox9 (1:500, Abcam, cat# ab185230), anti-Runx2 (1:500, Cell Signaling, cat# D1L7F), anti-Ki67 (1:2000, Abcam, cat# ab15580), anti-Vimentin (1:1000, Abcam, cat# ab8069), anti-BrdU (1:1000, Abcam, cat# ab6326), anti-Sox10 (1:500, Cell Signaling, cat# D5V9L), anti-ALPL (1:1000, Invitrogen, cat# PA5-47419), anti-Eed (1:1000, Cell Signaling, cat# E4L6E), and anti-Cleaved Caspase-3 (Asp175) (1:500, Cell Signaling, cat#9661). Secondary antibodies used in this study were Donkey anti-Rabbit IgG (H+L) Alexa Fluor Plus 555 (1:1000, Thermo Scientific, cat# A32794), Donkey anti-Rabbit IgG (H+L) Alexa Fluor 488 (1:1000, Thermo Scientific, cat# A21206), and Donkey anti-Rabbit IgG (H+L) Alexa Fluor Plus 568 (1:1000, Thermo Scientific, cat# A10042). DAPI solution (1:5000, Thermo Scientific, cat# 62248) was added to secondary antibody solutions. Slides or cover slips were mounted in ProLong Diamond Antifade Mountant (Thermo Scientific, cat# P36965) and cured overnight before imaging.

BrdU staining

Timed mating dams were subjected to intraperitoneal injection of 100mg/kg sterile BrdU in PBS (Abcam, cat# ab142567). After 2hr, mice were euthanized and embryos were harvested in cold PBS. Embryos were fixed in 4% PFA overnight at 4°C and cryosectioned. Sections were incubated with 1M HCl for 2hr then 0.1M sodium borate buffer for 15min before being subjected to standard immunofluorescence.

Microscopy and image analysis

Whole-mount skeletal and H&E stains were imaged using a Zeiss Stemi 305 Stereo Zoom microscope running Zeiss Blue v2.0. Whole-mount embryo DAPI stains were imaged using an upright Zeiss Axio Imager Z2 running AxioVision v4.0. Immunofluorescence images were obtained using a Zeiss LSM800 confocal laser scanning microscope running Zen Blue v2.0. Quantification of embryo measurements and immunofluorescence staining intensities was performed in ImageJ using standard thresholding and measurement of signal integrated density. Signal to nuclei normalization was performed by dividing signal intensity by DAPI signal per image. Quantification was performed using $n > 6$ images per embryo. Proliferation index was calculated by dividing number of Ki67+ or BrdU+ nuclei by the total number of DAPI stained nuclei per image.

Primary craniofacial cell culture

Timed mating embryos were dissected on ice cold PBS and heads were removed. Brains and eyes were removed from each head, and the remaining craniofacial structures were minced with a sterile blade on a glass surface. Tissue was enzymatically dissociated in 3mg/ml Collagenase Type 7 (Worthington, cat# CLS-6) in HBSS for 2-3hr at 37°C with frequent trituration using an Eppendorf ThermoMixer. Dissociated cells were filtered through a 70uM MACS smart strainer (Miltenyi Biotec, cat#130-110-916) and either plated on cover slips or cell culture dishes. Primary craniofacial cells were grown in DMEM with 10% FBS. For RNA extraction and immunofluorescence, cells were harvested one day following initial dissociation.

Single cell RNA-seq

Matched littermate timed embryos were dissected on ice cold PBS. Embryo heads were removed and minced using sterile razor blades on a glass surface. Tissue was enzymatically dissociated in 3mg/ml Collagenase Type 7 (Worthington, cat# CLS-6) in HBSS for 2-3hr at 37°C with frequent trituration using an Eppendorf ThermoMixer. The quality of the dissociation was frequently monitored by looking at the cell suspension on an automated cell counter. Cells were spun down at 350rcf, resuspended in MACS BSA stock solution (Miltenyi Biotec, cat# 130-091-376), and serially filtered through 70µm and 40µm MACS smart strainers (Miltenyi Biotec, cat# 130-110-916). Dissociation quality checks, cell viability, and counting was performed using an Invitrogen Countess 3 automated cell counter. 10,000 cells were loaded per single-cell RNA sequencing sample. Single-cell RNA sequencing libraries were generated using the Chromium Single Cell 3' Library & Gel Bead Kit v3.1 on a 10x Genomics Chromium controller using the manufacturer recommended default protocol and settings.

Single-cell RNA sequencing analysis

Library demultiplexing, read alignment to the mouse reference genome mm10, and unique molecular identifier (UMI) quantification was performed in Cell Ranger v7.2.0. Cells with greater than 200 unique genes were retained for analysis. Data were normalized and variance stabilized by SCTransform in Seurat v5.0 (Hao et al., 2024). UMAP and cluster analysis were performed using the Seurat function RunUMAP with parameters of mindist=0.7, res=0.4, dims=1:30. Cluster markers were identified using Seurat function FindAllMarkers with parameters min.pct = 0.25, thresh.use = 0.25. Differential gene expression analysis was performed using DElegate v1.1.0 (Hafemeister

and Halbritter, 2023) using the DEseq2 method, with biological replicate animals (n=3 per genotype) as the replicate_column parameter. Featureplots were generated using SCPubr v1.1.2 (Blanco-Carmona, 2022) and scale bars represent log2 UMI's corrected by SCTransform.

Statistics

All experiments were performed with independent biological replicates and repeated, and statistics were derived from biological replicates. Biological replicates are indicated in each figure panel or figure legend. No statistical methods were used to predetermine sample sizes, but sample sizes in this study are similar or larger to those reported in previous publications. Data distribution was assumed to be normal, but this was not formally tested. Investigators were blinded to conditions during data collection and analysis. Bioinformatic analyses were performed blind to clinical features, outcomes, and molecular characteristics. The samples used in this study were nonrandomized with no intervention, and all samples were interrogated equally. Thus, controlling for covariates among samples was not relevant. No data points were excluded from the analyses.

Results

Loss of Eed after neural crest induction causes severe craniofacial malformations.

To determine if *Eed* is required for the development of neural crest derivatives, homozygous floxed *Eed* alleles (*Eed*^{F1/F1}) were used to conditionally delete *Eed* following neural crest cell induction using Cre under control of the *Sox10* promoter, which is expressed in the migratory neural crest at embryonic day E8.75 and results in complete recombination in post-migratory neural crest cells by E10.5^{46,54}. *Sox10-Cre Eed*^{F1/F1} mice

were not recovered past postnatal day 0, suggesting that loss of *Eed* following induction of the neural crest is embryonic lethal (Fig. 1a). *Sox10-Cre Eed^{F/F}* embryos were recovered at expected genotypic frequencies from embryonic day E9.5 to E17.5 (Fig. 1a), and there were no differences in the penetrance or severity of *Sox10-Cre Eed^{F/F}* phenotypes whether Cre was maternally or paternally inherited, as has been reported for other phenotypes arising in cells expressing *Sox10-Cre*^{13,41}. No overt phenotypes were identified at early post-migratory neural crest cell stages E10.5 or E11.5, but craniofacial malformations were seen in *Sox10-Cre Eed^{F/F}* embryos starting at E12.5 that increased in severity throughout the remainder of embryonic development (Fig. 1a). *Sox10-Cre Eed^{F/F}* phenotypes were broadly consistent with impaired development of craniofacial structures⁶², including frontonasal and mandibular hypoplasia, a prominent telencephalon and exencephaly resulting from underdevelopment of the viscerocranium and frontal calvarium, collapsed nasal cavity bones, and microtia compared to controls (Fig. 1c). *Sox10-Cre Eed^{F/F}* embryos had increased pupillary distance and craniofacial width (Supplementary Fig. 1a-d), and whole mount DAPI imaging of *Sox10-Cre Eed^{F/F}* embryos revealed severe frontonasal dysplasia with underdeveloped midface and mandible, and an irregular and corrugated facial structure compared to controls (Fig. 1d). Although PRC2 is ubiquitously expressed in the developing embryo⁵⁵, *Sox10-Cre Eed^{F/F}* embryos did not have cardiac outflow tract defects or other structural heart malformations that can arise from impaired neural crest differentiation (40, 53) (Supplementary Fig. 2a-d and Movie 1, 2). Instead, fetal echocardiography showed subtle structural and functional changes but preserved ejection fraction and fraction shortening in *Sox10-Cre Eed^{F/F}* embryos compared to controls (Supplementary Fig. 2d).

Eed regulates craniofacial mesenchymal cell differentiation and proliferation from the early post-migratory neural crest.

Skeletal stains, computed tomography (microCT), histology, and immunofluorescence were used to shed light on how loss of *Eed* impacts craniofacial development. Whole mount alcian blue/alizarin red staining of *Sox10-Cre Eed^{F1/F1}* embryos revealed hypoplasia of the viscerocranium, including reduced frontal, temporal, maxillary, and mandibular bones, and complete loss of the tympanic ring and premaxillary and nasal bones compared to controls (Fig. 2a, b and Supplementary Fig. 3a). MicroCT validated these findings, showing fragmentation and hypoplasia of the frontal, temporal, maxillary, and mandibular bones, loss of frontal calvarial fusion, and absence of tympanic ring and nasal bones (Fig. 2c-e and Movie 3, 4). H&E histology showed that frontal calvarium reduction resulted in anteriorly displaced brain structures in *Sox10-Cre Eed^{F1/F1}* embryos compared to controls, with the midbrain and cortex in the same coronal plane as the nasal cavity and developing mandible (Fig. 3a and Supplementary Fig. 3b). Most of the midfacial and mandible were absent in *Sox10-Cre Eed^{F1/F1}* embryos, and the tongue and masseter muscles were underdeveloped (Fig. 3a).

Immunofluorescence demonstrated disorganized ALPL and Osteocalcin, markers of osteoblasts and mineralizing bone ⁴² in craniofacial tissues from *Sox10-Cre Eed^{F1/F1}* embryos compared to controls (Fig. 3b and Supplementary Fig. 3c). Immunofluorescence for Sox9, a marker of chondrocytes that are derived from the neural crest ^{52,73} was also disorganized in *Sox10-Cre Eed^{F1/F1}* embryos compared to controls (Fig. 3b). There was a small increase in immunofluorescence labeling index for cleaved Caspase 3 (Supplementary Fig. 3d, e), suggesting that apoptosis may play a subtle role in

craniofacial phenotypes from *Sox10-Cre Eed^{F1/F1}* embryos compared to controls. In contrast to *Wnt1-Cre Ezh2^{F1/F1}* embryos⁶² the craniofacial region of *Sox10-Cre Eed^{F1/F1}* embryos had marked decreased immunofluorescence labeling index for Ki67 (Fig. 3c, 3d), a marker of cell proliferation²¹ and decreased immunofluorescence staining for Vimentin (Vim), a marker of mesenchymal cells (Fig. 3c)⁴⁷. Immunofluorescence for Runx2, a transcription factor that is required for osteoblast differentiation and proliferation^{32,36} was also decreased in craniofacial tissues from *Sox10-Cre Eed^{F1/F1}* embryos compared to controls (Fig. 3e and Supplementary Fig. 3f). In support of these findings, BrdU labeling index was decreased in the craniofacial region of *Sox10-Cre Eed^{F1/F1}* embryos compared to controls (Supplementary Fig. 4a, b), *Eed*, Runx2, Ki67, and ALPL were decreased in primary *Sox10-Cre Eed^{F1/F1}* craniofacial cell cultures compared to controls (Fig. 3f and Supplementary Fig. 4c), and there was no change in immunofluorescence for Sox10 in either primary *Sox10-Cre Eed^{F1/F1}* craniofacial cell cultures or *Sox10-Cre Eed^{F1/F1}* embryos compared to controls (Supplementary Fig. 4c, e). These results suggest craniofacial mesenchymal differentiation, proliferation, and osteogenesis are impaired in *Sox10-Cre Eed^{F1/F1}* embryos^{26,33}.

Eed regulates craniofacial mesenchymal stem cell, osteoblast, and proliferating mesenchymal cell fate from the early post-migratory neural crest.

To define cell types and gene expression programs underlying craniofacial phenotypes in *Sox10-Cre Eed^{F1/F1}* embryos, single-cell RNA sequencing was performed on litter-matched E12.5 *Sox10-Cre Eed^{F1/WT}* and *Sox10-Cre Eed^{F1/F1}* heads (n=3 biological replicates per genotype). Uniform manifold approximation and projection (UMAP)

analysis of 63,730 single-cell transcriptomes revealed 23 cell clusters (C0-C22) that were defined using automated cell type classification ²⁷, cell signature genes, cell cycle analysis, and differentially expressed cluster marker genes (Fig. 4a, Supplementary Fig. 5, 6, and Supplementary Table 1, 2). Differentiating osteoblasts marked by *Runx2* (C0) and proliferating mesenchymal cells marked by Ki67 (C7) were enriched in *Sox10-Cre Eed^{F/WT}* samples (Fig. 4b-d). Mesenchymal stem cells marked by *Col6a3* (C4) or *Dcn* (C5) were enriched in *Sox10-Cre Eed^{F/FI}* samples ^{29,37} (Fig. 4b-d), suggesting that loss of *Eed* prevents craniofacial mesenchymal stem cell differentiation. There were subtle differences in the number of interneurons (C17, 1.4% versus 1.9% of cells, p=0.01), Schwann cells (C19, 1.0 versus 1.3% of cells, p=0.03), pericytes (C20, 0.7% vs 0.9%, p=0.05), and spinal neurons (C21, 0.5% vs 0.9% of cells, p=0.003) in *Sox10-Cre Eed^{F/WT}* versus *Sox10-Cre Eed^{F/FI}* samples, but each of these comprised a small minority of the recovered cell types (Student's t tests) (Supplementary Table 1). There were no differences between genotypes in the number of chondrocytes (C10, 3.1% versus 2.7%, p=0.09), fibroblasts (C11, 2.6% versus 2.7%, p=0.24), endothelia (C16, 1.9% vs 1.6%, p=0.22), hematopoietic cells, or other cell types recovered at E12.5 (Student's t tests) (Supplementary Table 1).

Differential expression analysis of single cell transcriptomes from differentiating osteoblasts (C0), which were enriched in *Sox10-Cre Eed^{F/WT}* samples (Fig. 4c), compared to mesenchymal stem cells marked by *Col6a3* (C4), which were enriched in *Sox10-Cre Eed^{F/FI}* samples (Fig. 4c), showed *Sox5* and *Sox6* were reduced in mesenchymal stem cells (Fig. 4e, Supplementary Fig. 7a, and Supplementary Table 3). These data are consistent with the known role of Sox transcription factors in craniofacial

specification and development⁶⁶. Iroquois homeobox (*Irx*) transcription factors 3 and 5, which contribute to craniofacial osteogenesis and mineralization^{3,7,69}, were also suppressed in mesenchymal stem cells compared to differentiating osteoblasts (Fig. 4e, Supplementary Fig. 7a, and Supplementary Table 3).

Differential expression analysis of single cell transcriptomes from differentiating osteoblasts compared to mesenchymal stem cells marked by *Dcn* (C5), which were also enriched in *Sox10-Cre Eed^{F1/F1}* samples (Fig. 4c), showed *Mecom*, *Trps1*, and *Ptch1* were suppressed and *Sparc* and *Tnmd* were enriched in mesenchymal stem cells (Fig. 4f, Supplementary Fig. 7b, and Supplementary Table 4). Loss of *Mecom* causes craniofacial malformations in mice and zebrafish⁶⁴ *Ptch1* is a key component of the Hedgehog pathway that is crucial for craniofacial osteogenesis^{30,48}, and *Trps1* regulates secondary palate and vibrissa development^{10,17}. Consistently, *Sox10-Cre Eed^{F1/F1}* samples had decreased vibrissa compared to controls (Fig. 1d and Supplementary Fig. 3b). *Sparc* drives morphogenesis of the pharyngeal arches and inner ear⁵⁹, and *Tnmd* regulates mesenchymal differentiation⁶³. *Pax3* and *Pax7*, key regulators of neural crest migration and development of skeletal structures⁴⁴ were also suppressed in mesenchymal stem cells compared to differentiating osteoblasts (Fig. 4f, Supplementary Fig. 7b, and Supplementary Table 4).

Differential expression analysis of single cell transcriptomes from the two clusters of mesenchymal stem cells that were marked by *Col6a3* (C4) versus *Dcn* (C5), both of which were enriched in *Sox10-Cre Eed^{F1/F1}* samples (Fig. 4c), showed *Twist2*, *Irx3*, and *Irx5*, which regulate mesenchymal differentiation to osteoblasts^{38,68,39} distinguished

mesenchymal stem cell populations (Fig. 4g, Supplementary Fig. 7c, and Supplementary Table 5).

To determine if there were differences in the gene expression programs from differentiating osteoblasts (C0), mesenchymal stem cells (C4, C5), or proliferating mesenchymal cells in *Sox10-Cre Eed^{F1/WT}* versus *Sox10-Cre Eed^{F1/F1}* samples, differential expression analysis was performed on single-cell transcriptomes from these clusters between genotypes (Supplementary Table 6). Consistent with craniofacial findings after loss of *Ezh2*^{35,62} and vertebral body findings after loss of *Eed*³⁴. Hox transcription factors were broadly de-repressed in mesenchymal cell populations from *Sox10-Cre Eed^{F1/F1}* samples compared to controls (Fig. 4h). PRC2 targets *Sp7* in bone marrow stroma cells⁴¹ and regulates Wnt signaling in dental stem cells³¹. Differential expression analysis showed that *Sp7* was enriched in mesenchymal single-cell transcriptomes from *Sox10-Cre Eed^{F1/WT}* samples and the Wnt and stem cell regulator gene *Gata4* was enriched in mesenchymal single-cell transcriptomes from *Sox10-Cre Eed^{F1/F1}* samples (Fig. 4h). *Mki67*, *Pax3*, and *Pax7* were enriched in mesenchymal single-cell transcriptomes from *Sox10-Cre Eed^{F1/WT}* samples, and the cell cycle inhibitors *Cdkn2a* and *Cdkn2b* were enriched in mesenchymal single-cell transcriptomes from *Sox10-Cre Eed^{F1/F1}* samples (Fig. 4h). In sum, these data show that *Eed* specifies craniofacial osteoblast differentiation and mesenchymal cell proliferation by regulating diverse transcription factor programs that are required for specification of post-migratory neural crest cells, and that loss of *Eed* inhibits mesenchymal stem cell differentiation and mesenchymal cell proliferation by de-repressing transcription factors and inhibitors of the cell cycle. These data contrast with the function of *Eed* in chondrocytes, where genetic inactivation of *Eed* at a later stage in

mesenchymal development accelerates hypertrophic differentiation, leading to hypoxia and cell death ⁵⁰.

Discussion

Epigenetic regulation of the neural crest, which differentiates into diverse mesenchymal derivatives, is incompletely understood. Here we identify the PRC2 core subunit *Eed* as a potent regulator of craniofacial development after induction of the neural crest. Conditional deletion of *Eed* using *Sox10-Cre* causes severe craniofacial malformations that are consistent with impaired differentiation and proliferation of cells arising from the pharyngeal arches ¹⁹. In support of this hypothesis, we observed severe defects in the development of craniofacial mesenchyme-derived tissues (Fig. 1, 2) that were consistent with molecular and cellular findings from *Sox10-Cre Eed^{F1/F1}* embryos (Fig. 3, 4). Expression of key regulators of craniofacial osteogenesis such as *Runx2*, *Irx3*, *Irx5*, *Mecom*, *Trps1*, *Ptch1*, *Pax3*, and *Pax7* were reduced in *Sox10-Cre Eed^{F1/F1}* heads and primary craniofacial cell cultures compared to controls, and single-cell RNA sequencing showed reduced craniofacial osteoblast differentiation and reduced proliferation of mesenchymal cells in *Sox10-Cre Eed^{F1/F1}* heads compared to controls. We also identified subtle cardiac phenotypes and a small increase in apoptosis in *Sox10-Cre Eed^{F1/F1}* embryos. These data suggest that PRC2 may contribute to the development of diverse neural crest-derived tissues but is particularly important for craniofacial mesenchymal cell differentiation and proliferation.

By using *Sox10-Cre*, which marks the migratory neural crest ⁴⁶, we bypass potential roles of *Eed* in neural crest cell induction to examine its function in neural crest

cell development. The requirement of PRC2 for craniofacial development has been studied in the context of *Ezh2* loss using *Wnt1-Cre*⁶² but to our knowledge, our study is the first report directly linking *Eed* to differentiation of neural crest-derived mesenchymal cells. To date, fifteen human missense mutations in *EED* have been reported as pathogenic for Cohen-Gibson syndrome^{11,12,23}. Like Weaver syndrome, which arises from missense mutations in *EZH2*^{22,70}, and Imagawa-Matsumoto syndrome, which arises from missense mutations in *SUZ12*²⁸, Cohen-Gibson syndrome is a rare congenital syndrome associated with craniofacial malformations, advanced bone age, intellectual disability, and developmental delay⁶⁷. *EED* mutations in individuals with Cohen-Gibson syndrome cluster in WD40 domains 3 through 5 and are predicted to (1) abolish interaction with EZH2, (2) prevent histone methyltransferase activity, and (3) inhibit H3K27 trimethylation peptide binding. In support of these hypotheses, functional investigations have shown that single nucleotide variants in the WD40 domain of *EED* abolish binding to *EZH2 in vitro*¹⁵. Mouse models encoding pathogenic *EZH2* missense variants, which are predicted to result in loss of function of the PRC2 complex, phenocopy Weaver syndrome and cause excess osteogenesis and skeletal overgrowth²⁰. In this study, we show that loss of *Eed* after neural crest induction causes the opposite phenotype, resulting in craniofacial hypoplasia due to impairments in osteogenesis, mesenchymal cell proliferation, and mesenchymal stem cell differentiation. The discrepancy of missense variants in *EED* causing gain of craniofacial osteogenic function in humans versus loss of *Eed* causing loss of craniofacial osteogenic function in mice warrants further study, including investigation using alternative Cre drivers to target different developmental stages of the neural crest. Despite these discrepancies, it is

notable that many of the phenotypes we observed after loss of *Eed* in the neural crest of mice were similar to previously reported phenotypes after loss of *Ezh2* in the neural crest cell in mice, with the exception of proliferation deficits after loss of *Eed* but not after loss of *Ezh2*⁶².

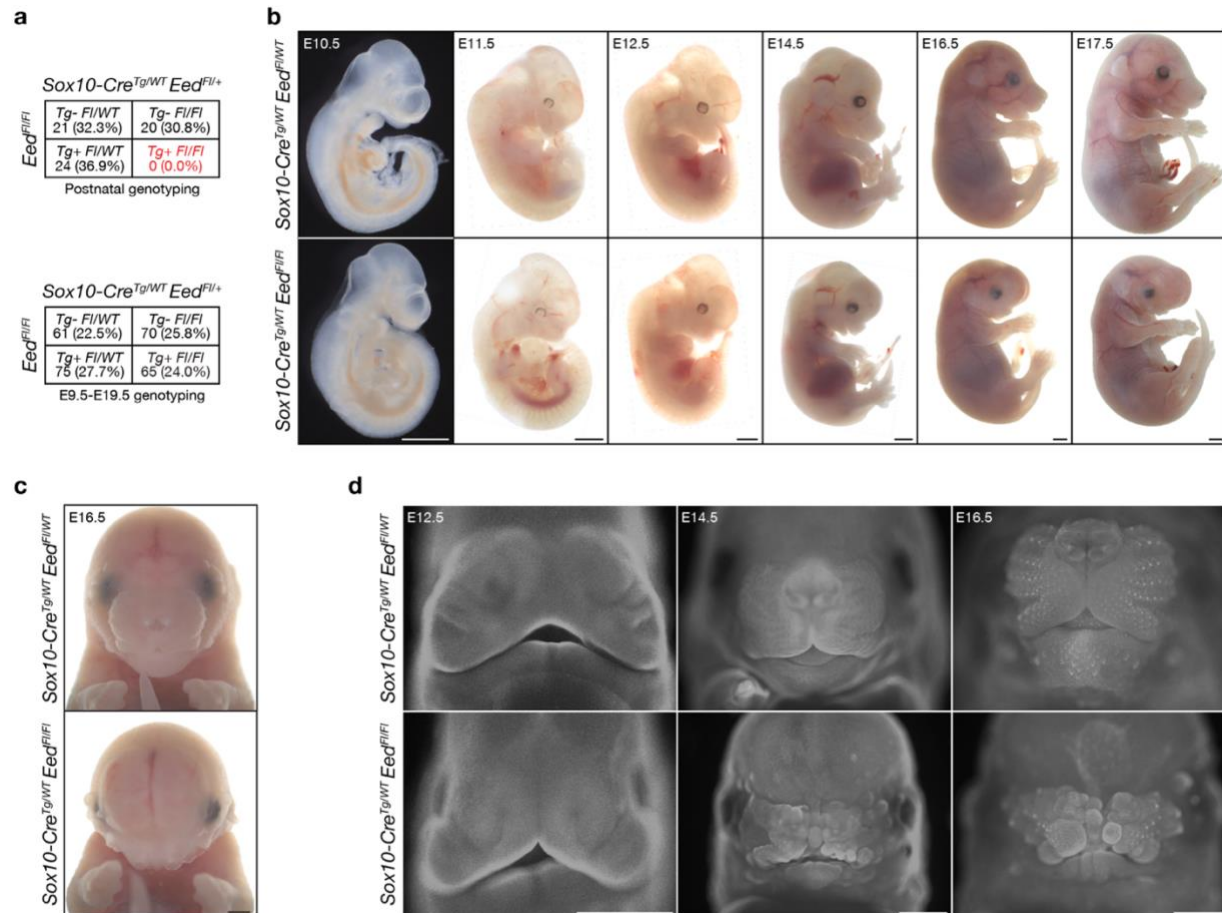


Fig. 1. Sox10-Cre Eed^{F/FI} embryos develop craniofacial malformations in utero.

(a) Genotyping frequencies of postnatal postnatal (top) and embryonic (bottom) Sox10-Cre Eed^{F/FI} mice. (b) Sagittal brightfield images of Sox10-Cre Eed^{F/WT} or Sox10-Cre Eed^{F/FI} embryos from E10.5 to E17.5 showing craniofacial malformations appearing at E12.5 that were observed with 100% penetrance. Scale bar, 1mm. (c) Coronal brightfield images of E16.5 Sox10-Cre Eed^{F/WT} or Sox10-Cre Eed^{F/FI} embryos showing craniofacial malformations. Scale bar, 1mm. (d) Whole-mount fluorescence microscopy of DAPI-stained Sox10-Cre Eed^{F/WT} or Sox10-Cre Eed^{F/FI} heads at E12.5, E14.5, or E16.5. Scale bar, 1mm. All images are representative of ≥ 3 biological replicates.

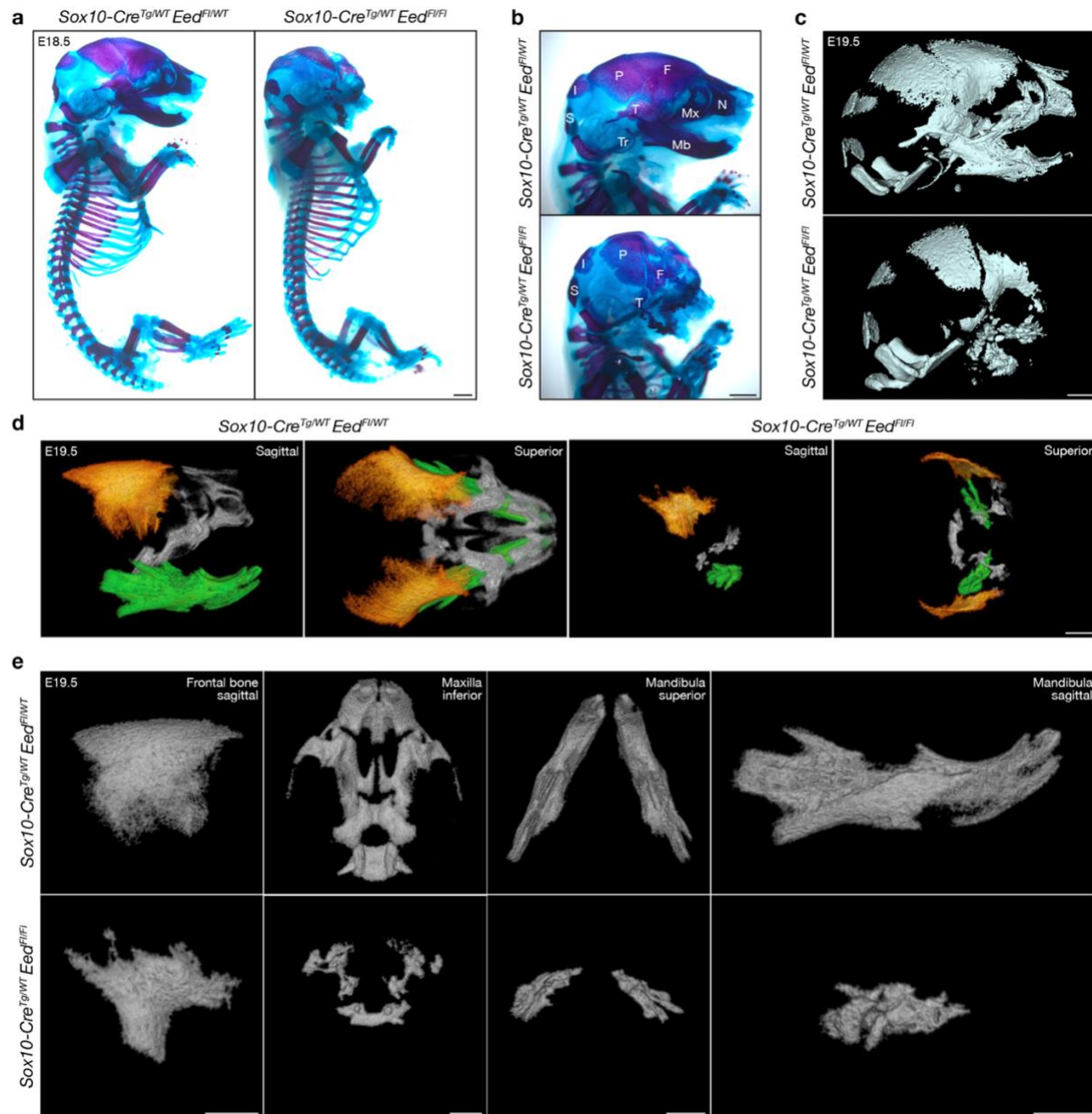


Fig. 2. *Eed* is required for craniofacial skeletal development from the neural crest.

(a) Sagittal brightfield images of whole-mount skeletal stains of E18.5 *Sox10-Cre Eed^{F1/WT}* or *Sox10-Cre Eed^{F1/F1}* embryos. Alcian blue and alizarin red identify cartilage and bone, respectively. Scale bar, 1mm. (b) Magnified sagittal brightfield images of whole-mount skeletal stains of E18.5 *Sox10-Cre Eed^{F1/WT}* or *Sox10-Cre Eed^{F1/F1}* embryos. Bones structures are annotated (I, interparietal; P, parietal; Mx, maxilla; Mb, mandible; Tr, tympanic ring; F, frontal; N, nasal; T, temporal; S, supraoccipital). Scale bar, 1mm. (c) Micro-CT images of E19.5 *Sox10-Cre Eed^{F1/WT}* or *Sox10-Cre Eed^{F1/F1}* heads. Scale bar, 1 μ m. (d) Micro-CT images of E19.5 *Sox10-Cre Eed^{F1/WT}* or *Sox10-Cre Eed^{F1/F1}* neural crest-derived craniofacial bones shaded in orange (frontal), grey (maxilla), or green (mandible). Scale bar, 1 μ m. (e) Micro-CT images of E19.5 *Sox10-Cre Eed^{F1/WT}* or *Sox10-Cre Eed^{F1/F1}* neural crest-derived craniofacial bones shaded. Scale bars, 1 μ m.

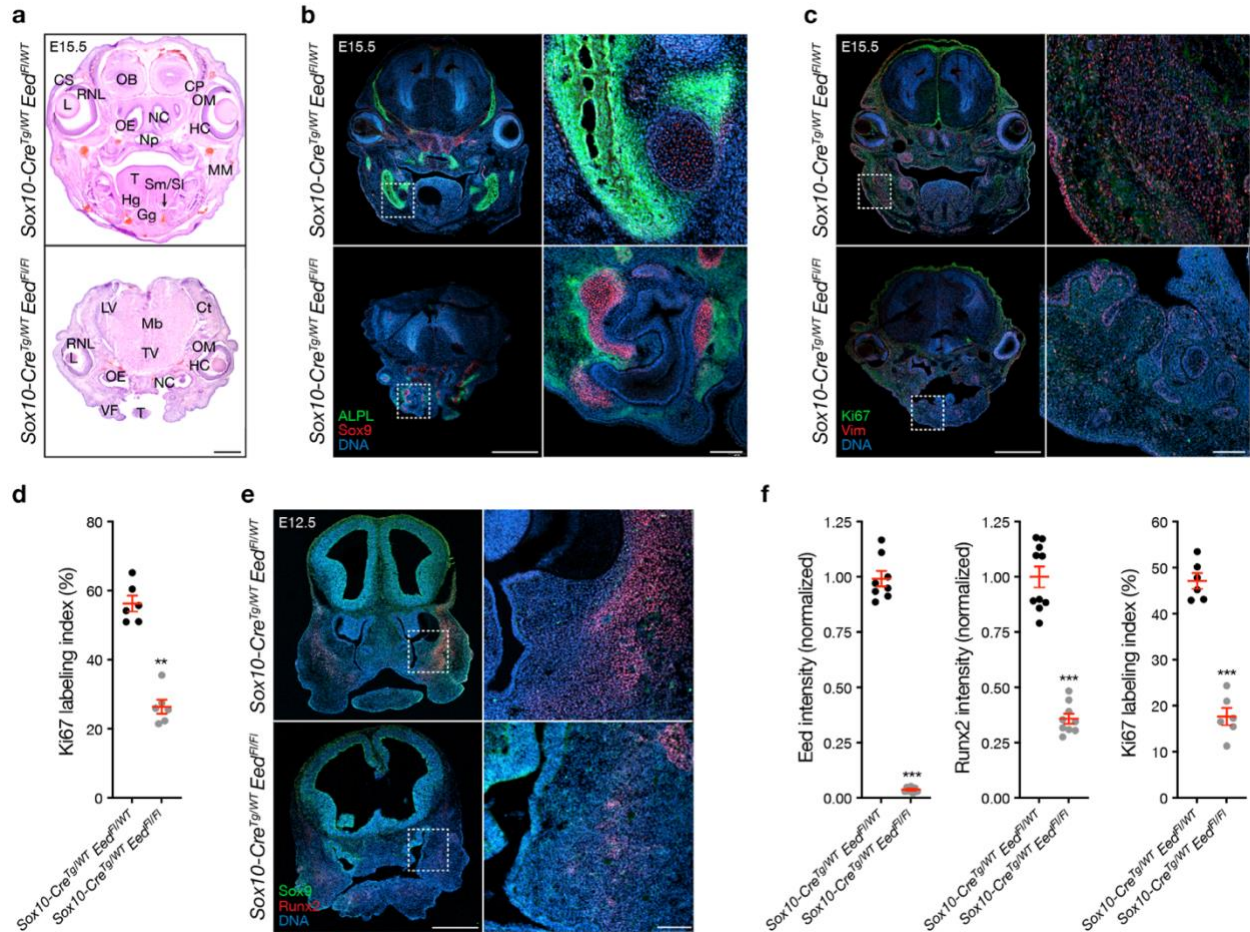


Fig. 3. Eed regulates craniofacial differentiation and proliferation from the neural crest. (a) Brightfield coronal H&E images of E15.5 *Sox10-Cre Eed^{F1/WT}* or *Sox10-Cre Eed^{F1/F1}* heads. Anatomic structures are annotated (Ct, cortex; CP, cartilage primordium; CS, conjunctival sac; Gg, genioglossus muscle; HC, hyaloid cavity; Hg, hyoglossus muscle; L, lens; LV, lateral ventricle; Mb, midbrain; MM, masseter muscle; Np, nasopharynx; NC, nasal cavity; OB, olfactory bulb; OE, olfactory epithelium; OM, ocular muscle; RNL, retina neural layer; Sm/St, sublingual and submandibular ducts; T, tongue; TV, third ventricle; VF, vibrissa follicles). Scale bar, 1mm. (b) Coronal immunofluorescence images of E15.5 *Sox10-Cre Eed^{F1/WT}* or *Sox10-Cre Eed^{F1/F1}* heads stained for ALPL (green) and Sox9 (red). Scale bars, 1mm and 100µm. (c) Coronal immunofluorescence images of E15.5 *Sox10-Cre Eed^{F1/WT}* or *Sox10-Cre Eed^{F1/F1}* heads stained for Ki67 (green) and Vimentin (red). Scale bars, 1mm and 100µm. (d) Quantification of Ki67 immunofluorescence labeling index from E15.5 heads. (e) Coronal immunofluorescence images of E12.5 *Sox10-Cre Eed^{F1/WT}* or *Sox10-Cre Eed^{F1/F1}* heads stained for Runx2 (red) and Sox9 (green). Intracranial tissues demonstrate *ex vacuo* dilation and anterior herniation in *Sox10-Cre Eed^{F1/F1}* heads. DNA is marked by DAPI. Scale bars, 500µm and 100µm. (f) Quantification of immunofluorescence imaging intensity from primary craniofacial cell cultures from E12.5 *Sox10-Cre Eed^{F1/WT}* or *Sox10-Cre Eed^{F1/F1}* embryos. All images are representative of ≥ 3 biological replicates. DNA is marked by DAPI. Lines represent means and error bars represent standard error of the means. Student's t-tests, ** $p \leq 0.01$, *** $p \leq 0.0001$.

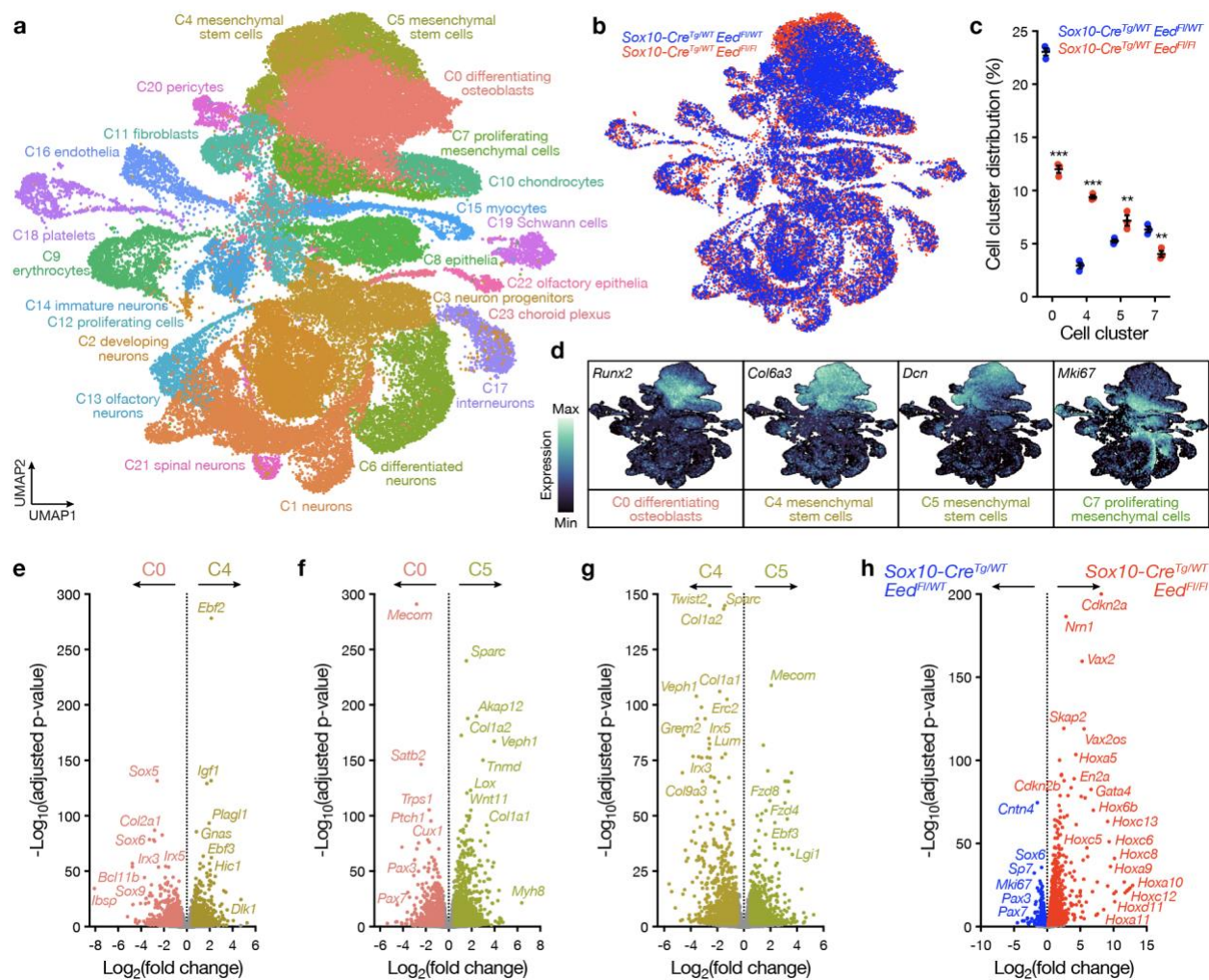
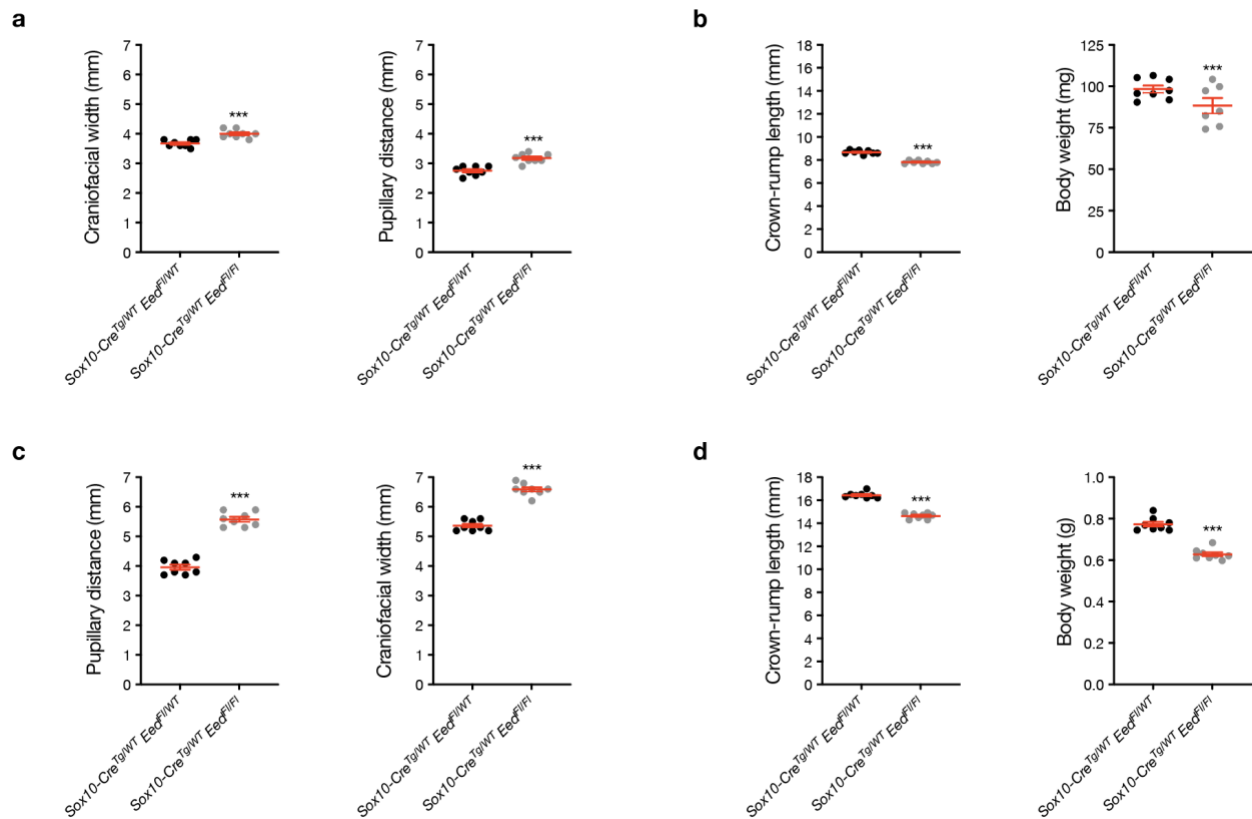
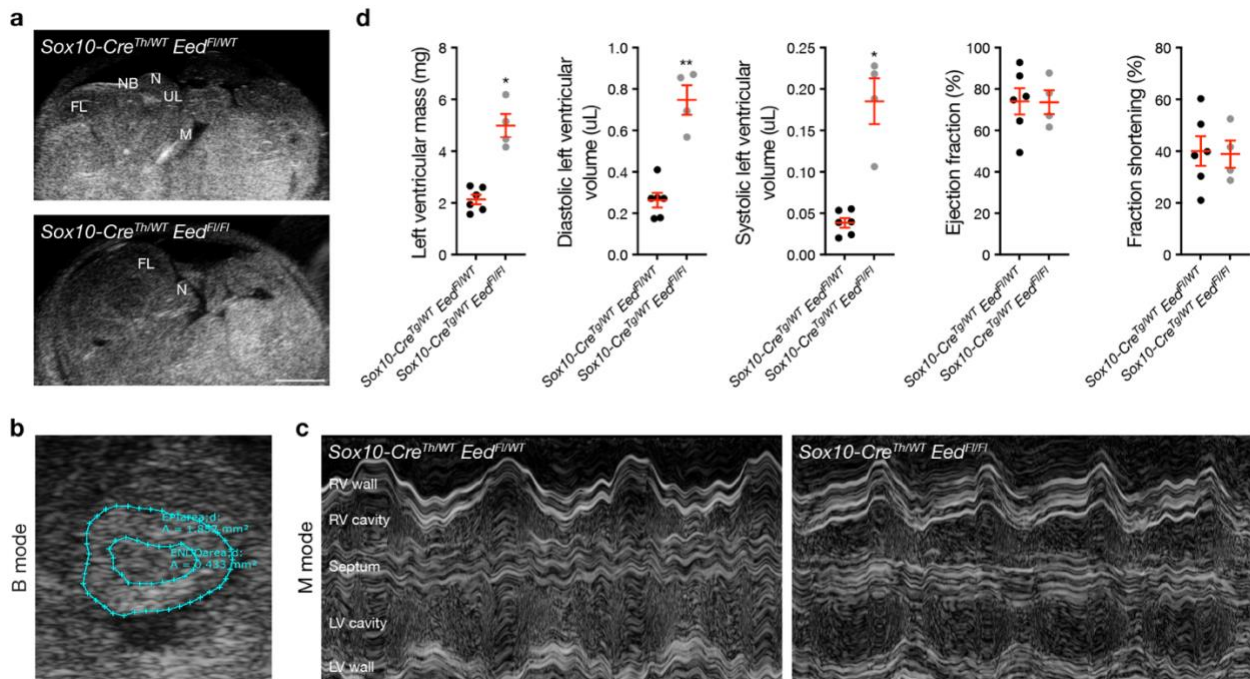


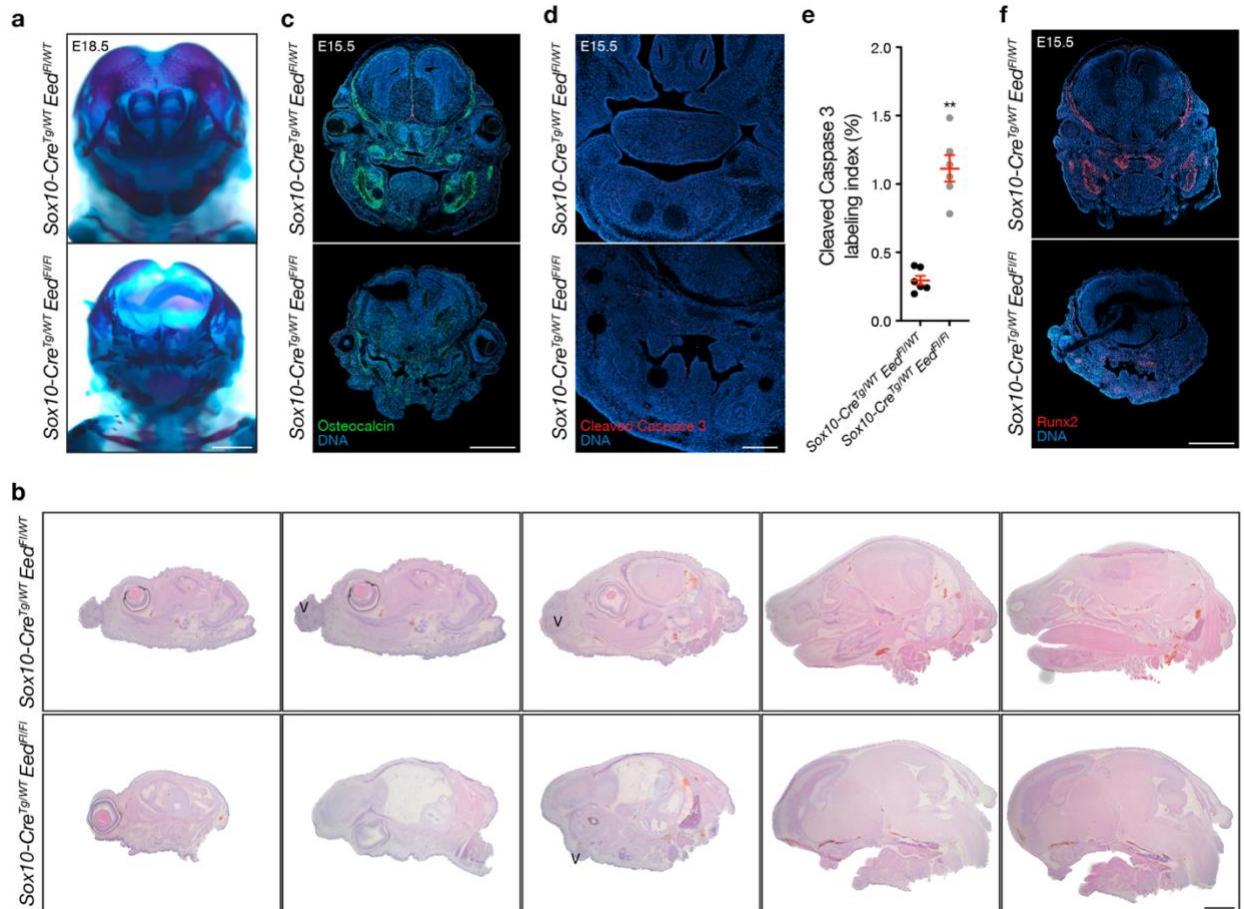
Fig. 4. *Eed* regulates craniofacial mesenchymal stem cell, osteoblast, and proliferating mesenchymal cell fate from the neural crest. (a) Integrated UMAP of 63,730 transcriptomes from single-cell RNA sequencing of litter-matched E12.5 *Sox10-Cre Eed^{F1/WT}* (n=3) or *Sox10-Cre Eed^{F1/F1}* (n=3) heads. (b) Integrated UMAP overlaying cell cluster distribution from single-cell RNA sequencing. (c) Quantification of mesenchymal cell cluster distribution from single-cell RNA sequencing. Lines represent means and error bars represent standard error of the means. Student's t-tests, **p<0.01, ***p<0.0001. (d) Gene expression feature plots of mesenchymal lineages from single-cell RNA sequencing. (e) Volcano plot showing differentially expressed genes between C0 (osteoblasts) and C4 (mesenchymal stem cells). (g) Volcano plot showing differentially expressed genes between C0 and C5 (mesenchymal stem cells). (a) Volcano plot showing differentially expressed genes between 2 clusters of mesenchymal stem cells from single-cell RNA sequencing of litter-matched E12.5 *Sox10-Cre Eed^{F1/WT}* (n=3) or *Sox10-Cre Eed^{F1/F1}* (n=3) heads. (c) Volcano plot showing differentially expressed genes in differentiating osteoblasts (C0), mesenchymal stem cells (C4, C5), and proliferating mesenchymal cells (C7) from single-cell RNA sequencing of litter-matched E12.5 *Sox10-Cre Eed^{F1/WT}* (n=3) versus *Sox10-Cre Eed^{F1/F1}* (n=3) heads.



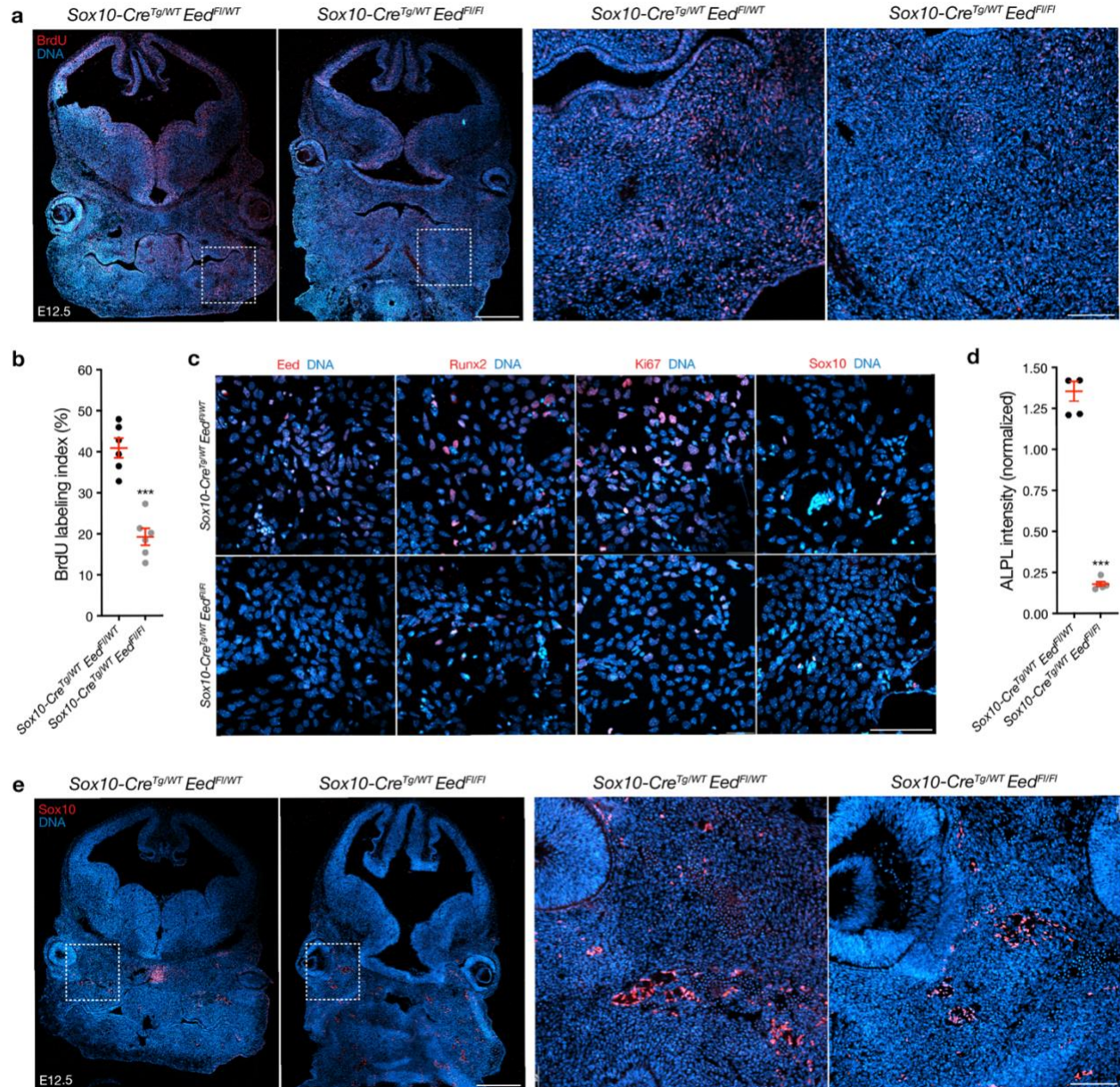
Supplementary Fig. 1. Sox10-Cre Eed^{F1/F1} embryos develop significant craniofacial malformations in utero. (a) Craniofacial measurement quantification of pupillary distance (left) or craniofacial width (right) from E12.5 Sox10-Cre Eed^{F1/WT} or Sox10-Cre Eed^{F1/F1} embryos. (b) Body measurement quantification of crown-rump length from E12.5 Sox10-Cre Eed^{F1/WT} or Sox10-Cre Eed^{F1/F1} embryos. Lines represent means and error bars represent standard error of the means. (c) Craniofacial measurement quantification of pupillary distance (left) or craniofacial width (right) from E16.5 Sox10-Cre Eed^{F1/WT} or Sox10-Cre Eed^{F1/F1} embryos. (d) Body measurement quantification of crown-rump length (left) or body weight (right) from E16.5 Sox10-Cre Eed^{F1/WT} or Sox10-Cre Eed^{F1/F1} embryos. Lines represent means and error bars represent standard error of the means. Student's t-tests, ***p<0.0001.



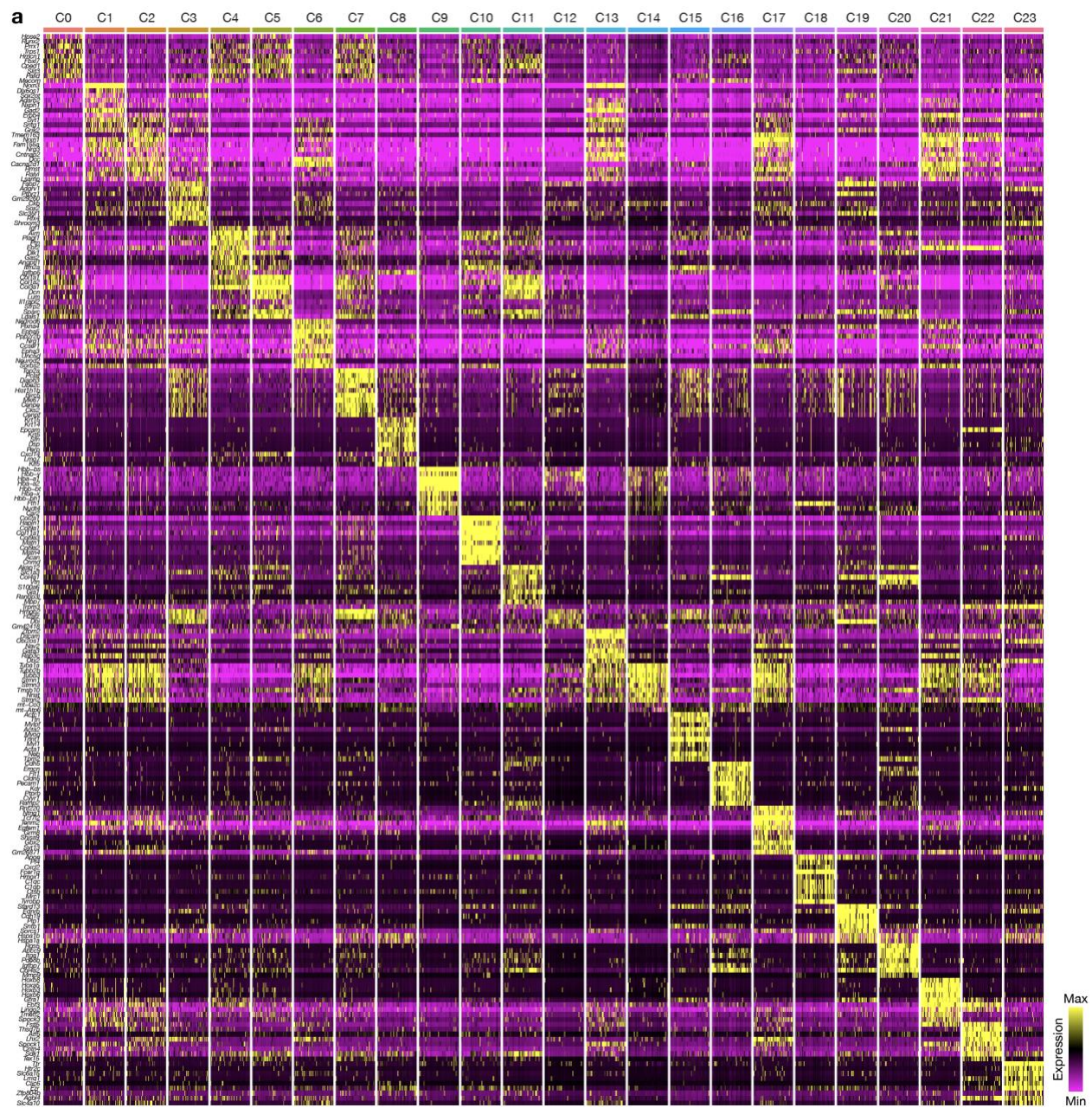
Supplementary Fig. 2. Sox10-Cre Eed^{F1/F1} embryos develop subtle cardiac malformations in utero. (a) Sagittal view of E16.5 Sox10-Cre Eed^{F1/WT} (top) or Sox10-Cre Eed^{F1/F1} (bottom) embryos in B-mode echocardiography (FL, frontal lobe; NB, nasal bridge; N, nose; UL, upper lip; M, mandible). Scale bar, 1mm. (b) Transversal view of B-mode echocardiography with measurements of left ventricle internal and external areas of an E16.5 embryo. (c) M-mode echocardiography of E16.5 Sox10-Cre Eed^{F1/WT} (left) or Sox10-Cre Eed^{F1/F1} (right) embryos. Four cardiac cycles are included per trace and all cardiac segments are visible in each embryo, as labeled. (d) Quantitative echocardiography measurements from Sox10-Cre Eed^{F1/WT} or Sox10-Cre Eed^{F1/F1} embryos. Lines represent means and error bars represent standard error of the means. Student's t-tests, *p≤0.05, **p≤0.01.



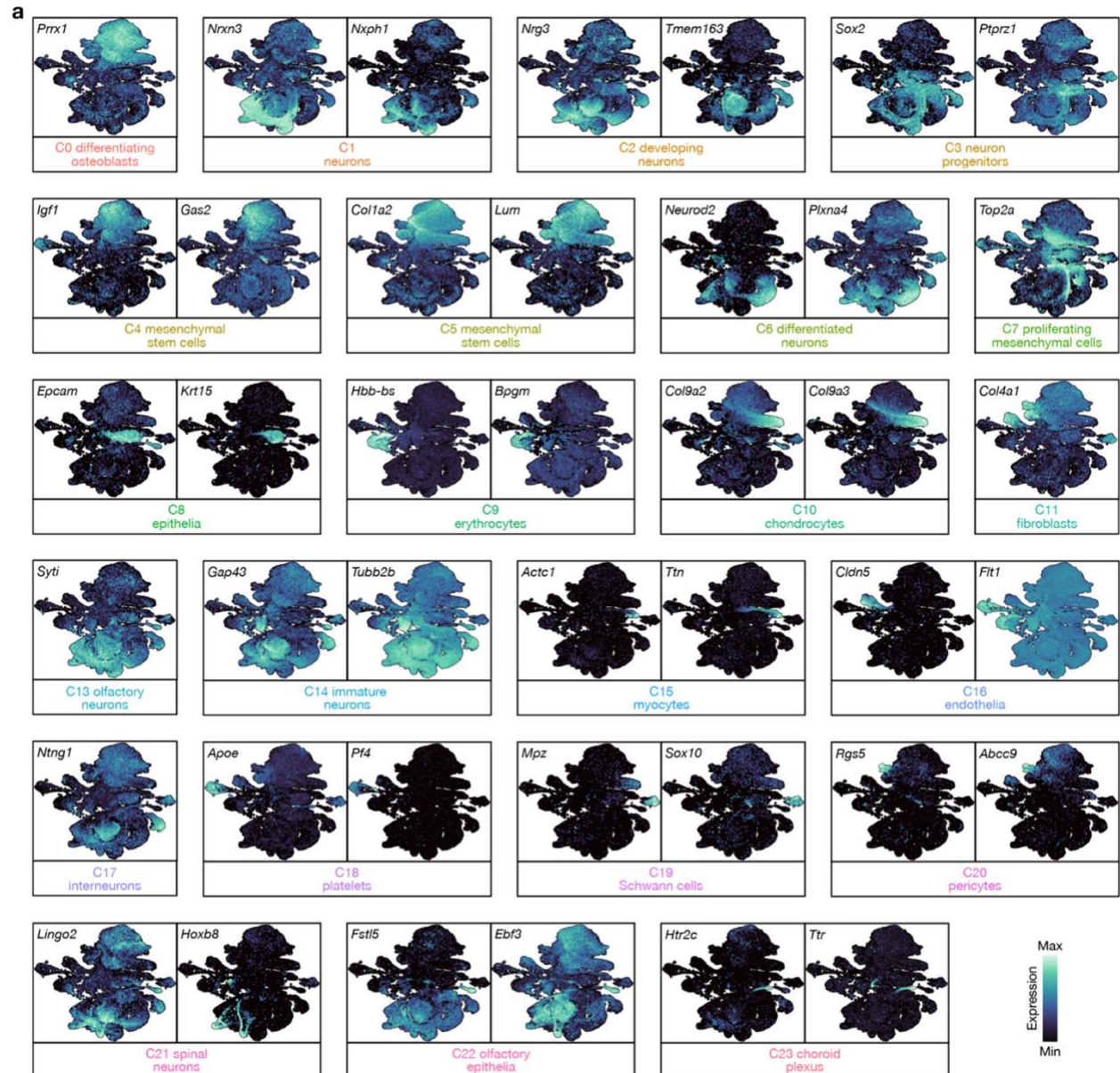
Supplementary Fig. 3. Sox10-Cre Eed^{F1/F1} embryos develop significant craniofacial mesenchymal differentiation phenotypes and subtle apoptotic phenotypes in utero. (a) Coronal brightfield images of whole-mount skeletal stains of E18.5 Sox10-Cre Eed^{F1/WT} or Sox10-Cre Eed^{F1/F1} embryos. Scale bar, 1mm. (b) Brightfield sagittal H&E images of E16.5 Sox10-Cre Eed^{F1/WT} or Sox10-Cre Eed^{F1/F1} heads in series from lateral (left) to medial (right). Vibrissa (V) were reduced in Sox10-Cre Eed^{F1/F1} heads compared to controls. Scale bar, 1mm. (c) Coronal immunofluorescence images of E15.5 Sox10-Cre Eed^{F1/WT} or Sox10-Cre Eed^{F1/F1} heads stained for osteocalcin (green). Scale bar, 1mm. (d) Coronal immunofluorescence images of E15.5 Sox10-Cre Eed^{F1/WT} or Sox10-Cre Eed^{F1/F1} mandibles stained for Cleaved Caspase 3 (red). Scale bar, 100µm. (e) Quantification of Cleaved Caspase 3 immunofluorescence labeling index from E15.5 Sox10-Cre Eed^{F1/WT} or Sox10-Cre Eed^{F1/F1} mandibles. Lines represent means and error bars represent standard error of the means. Student's t-test, **p≤0.01. (f) Coronal immunofluorescence images of E15.5 Sox10-Cre Eed^{F1/WT} or Sox10-Cre Eed^{F1/F1} heads stained for Runx2 (red). Scale bar, 1mm. All images are representative of ≥3 biological replicates. DNA is marked by DAPI.



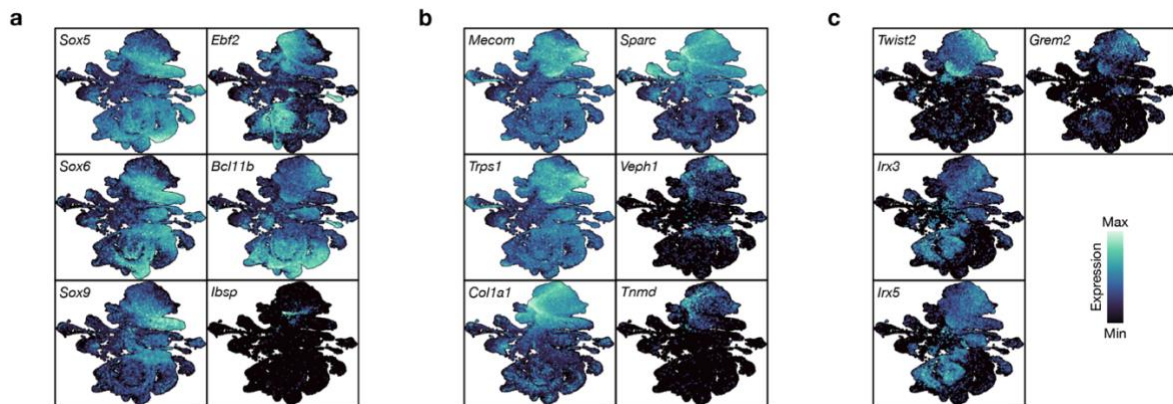
Supplementary Fig. 4. Eed regulates craniofacial differentiation and proliferation in vivo and in primary cell cultures. (a) Coronal immunofluorescence images of E12.5 *Sox10-Cre Eed^{F1/WT}* or *Sox10-Cre Eed^{F1/F1}* heads stained for BrdU (red). Scale bars, 500 μ m and 50 μ m. (b) Quantification of BrdU immunofluorescence labeling index from E12.5 heads. (c) Immunofluorescence images of primary craniofacial cell cultures from E12.5 *Sox10-Cre Eed^{F1/WT}* or *Sox10-Cre Eed^{F1/F1}* embryos stained for Eed, Runx2, Ki67, or Sox10. Scale bar, 100 μ m. (d) Quantification of ALPL immunofluorescence imaging intensity from primary E15.5 craniofacial cell cultures. (e) Coronal immunofluorescence images of E12.5 *Sox10-Cre Eed^{F1/WT}* or *Sox10-Cre Eed^{F1/F1}* heads stained for Sox10 (red). Scale bars, 500 μ m and 50 μ m. All images are representative of ≥ 3 biological replicates. DNA is marked by DAPI. Lines represent means and error bars represent standard error of the means. Student's t-tests, *** $p \leq 0.0001$.



Supplementary Fig 5. Cell clusters from single-cell RNA sequencing of E12.5 Sox10-Cre *Eed*^{FI/WT} or Sox10-Cre *Eed*^{FI/FI} heads. (a) Heat map of differentially expressed genes across 23 cell clusters.



Supplementary Fig. 6. Cell cluster marker genes from single-cell RNA sequencing of E12.5 Sox10-Cre Eed^{F1/WT} or Sox10-Cre Eed^{F1/F1} heads. (a) Gene expression feature plots for differentially expressed genes across 23 cell clusters.



Supplementary Fig. 7. Single-cell transcriptome differential expression analyses among mesenchymal cell clusters. (a) Gene expression feature plots for differentially expressed genes between C0 and C4. (b) Gene expression feature plots for differentially expressed genes between C0 and C5. (c) Gene expression feature plots for differentially expressed genes between mesenchymal stem cell clusters.

References

1. Bertol, J. W., Johnston, S., Ahmed, R., Xie, V. K., Hubka, K. M., Cruz, L., Nitschke, L., Stetsiv, M., Goering, J. P., Nistor, P., et al. (2022). Twist1 interacts with beta/delta-Catenins during neural tube development and regulates fate transition in cranial neural crest cells. *Development* 149,.
2. Blanco-Carmona, E. (2022). Generating publication ready visualizations for Single Cell transcriptomics using SCpubr. *bioRxiv* 2022.02.28.482303.
3. Bonnard, C., Strobl, A. C., Shboul, M., Lee, H., Merriman, B., Nelson, S. F., Ababneh, O. H., Uz, E., Güran, T., Kayserili, H., et al. (2012). Mutations in IRX5 impair craniofacial development and germ cell migration via SDF1. *Nat. Genet.* 44, 709–713.
4. Bowers, S. L. K., Meng, Q., Kuwabara, Y., Huo, J., Minerath, R., York, A. J., Sargent, M. A., Prasad, V., Saviola, A. J., Galindo, D. C., et al. (2023). Col1a2-Deleted Mice Have Defective Type I Collagen and Secondary Reactive Cardiac Fibrosis with Altered Hypertrophic Dynamics. *Cells* 12, 2174.
5. Bronner, M. E. and LeDouarin, N. M. (2012). Development and evolution of the neural crest: An overview. *Dev. Biol.* 366, 2–9.
6. Cain, C. J., Gaborit, N., Lwin, W., Barruet, E., Ho, S., Bonnard, C., Hamamy, H., Shboul, M., Reversade, B., Kayserili, H., et al. (2016). Loss of Iroquois homeobox transcription factors 3 and 5 in osteoblasts disrupts cranial mineralization. *Bone Rep.* 5, 86–95.
7. Cardiff, R. D., Miller, C. H. and Munn, R. J. (2014). Manual Hematoxylin and Eosin Staining of Mouse Tissue Sections. *Cold Spring Harb. Protoc.* 2014, pdb.prot073411.

8. Cheung, M., Chaboissier, M.-C., Mynett, A., Hirst, E., Schedl, A. and Briscoe, J. (2005). The Transcriptional Control of Trunk Neural Crest Induction, Survival, and Delamination. *Dev. Cell* 8, 179–192.
9. Cho, K. Y., Kelley, B. P., Monier, D., Lee, B., Szabo-Rogers, H. and Napierala, D. (2019). Trps1 Regulates Development of Craniofacial Skeleton and Is Required for the Initiation of Palatal Shelves Fusion. *Front. Physiol.* 10, 513.
10. Cohen, A. S. and Gibson, W. T. (2016). EED-associated overgrowth in a second male patient. *J. Hum. Genet.* 61, 831–834.
11. Cohen, A. S. A., Tuysuz, B., Shen, Y., Bhalla, S. K., Jones, S. J. M. and Gibson, W. T. (2015). A novel mutation in EED associated with overgrowth. *J. Hum. Genet.* 60, 339–342.
12. Crispino, G., Pasquale, G. D., Scimemi, P., Rodriguez, L., Ramirez, F. G., Siaty, R. D. D., Santarelli, R. M., Arslan, E., Bortolozzi, M., Chiorini, J. A., et al. (2011). BAAV Mediated GJB2 Gene Transfer Restores Gap Junction Coupling in Cochlear Organotypic Cultures from Deaf Cx26Sox10Cre Mice. *PLoS ONE* 6, e23279.
13. Deckelbaum, R. A., Holmes, G., Zhao, Z., Tong, C., Basilico, C. and Loomis, C. A. (2012). Regulation of cranial morphogenesis and cell fate at the neural crest-mesoderm boundary by engrailed 1. *Development* 139, 1346–1358.
14. Denisenko, O., Shnyreva, M., Suzuki, H. and Bomsztyk, K. (1998). Point Mutations in the WD40 Domain of Eed Block Its Interaction with Ezh2. *Mol. Cell. Biol.* 18, 5634–5642.
15. Dudakovic, A., Camilleri, E. T., Xu, F., Riester, S. M., McGee-Lawrence, M. E., Bradley, E. W., Paradise, C. R., Lewallen, E. A., Thaler, R., Deyle, D. R., et al. (2015).

Epigenetic Control of Skeletal Development by the Histone Methyltransferase Ezh2*. *J. Biol. Chem.* 290, 27604–27617.

16. Fantauzzo, K. A. and Christiano, A. M. (2011). Trps1 activates a network of secreted Wnt inhibitors and transcription factors crucial to vibrissa follicle morphogenesis. *Development* 139, 203–214.
17. Faust, C., Schumacher, A., Holdener, B. and Magnuson, T. (1995). The eed mutation disrupts anterior mesoderm production in mice. *Development* 121, 273–285.
18. Frisdal, A. and Trainor, P. A. (2014). Development and evolution of the pharyngeal apparatus. *Wiley Interdiscip. Rev.: Dev. Biol.* 3, 403–418.
19. Gao, C. W., Lin, W., Riddle, R. C., Kushwaha, P., Boukas, L., Björnsson, H. T., Hansen, K. D. and Fahrner, J. A. (2023). Novel mouse model of Weaver syndrome displays overgrowth and excess osteogenesis reversible with KDM6A/6B inhibition. *bioRxiv* 2023.06.23.546270.
20. Gerdes, J., Lemke, H., Baisch, H., Wacker, H. H., Schwab, U. and Stein, H. (1984). Cell cycle analysis of a cell proliferation-associated human nuclear antigen defined by the monoclonal antibody Ki-67. *J. Immunol. (Baltim., Md : 1950)* 133, 1710–5.
21. Gibson, W. T., Hood, R. L., Zhan, S. H., Bulman, D. E., Fejes, A. P., Moore, R., Mungall, A. J., Eydoux, P., Babul-Hirji, R., An, J., et al. (2012). Mutations in EZH2 Cause Weaver Syndrome. *Am. J. Hum. Genet.* 90, 110–118.
22. Goel, H., O'Donnell, S. and Edwards, M. (2024). EED related overgrowth: First report of multiple members in a single family. *Am. J. Méd. Genet. Part A* 194, 374–382.

23. Hafemeister, C. and Halbritter, F. (2023). Single-cell RNA-seq differential expression tests within a sample should use pseudo-bulk data of pseudo-replicates. *bioRxiv* 2023.03.28.534443.
24. Hao, Y., Stuart, T., Kowalski, M. H., Choudhary, S., Hoffman, P., Hartman, A., Srivastava, A., Molla, G., Madad, S., Fernandez-Granda, C., et al. (2024). Dictionary learning for integrative, multimodal and scalable single-cell analysis. *Nat. Biotechnol.* 42, 293–304.
25. Honoré, S. M., Aybar, M. J. and Mayor, R. (2003). Sox10 is required for the early development of the prospective neural crest in *Xenopus* embryos. *Dev. Biol.* 260, 79–96.
26. Ianevski, A., Giri, A. K. and Aittokallio, T. (2022). Fully-automated and ultra-fast cell-type identification using specific marker combinations from single-cell transcriptomic data. *Nat Commun* 13, 1246.
27. Imagawa, E., Albuquerque, E. V. A., Isidor, B., Mitsuhashi, S., Mizuguchi, T., Miyatake, S., Takata, A., Miyake, N., Boguszewski, M. C. S., Boguszewski, C. L., et al. (2018). Novel SUZ12 mutations in Weaver-like syndrome. *Clin. Genet.* 94, 461–466.
28. Jang, Y. O., Cho, M.-Y., Yun, C.-O., Baik, S. K., Park, K.-S., Cha, S.-K., Chang, S. J., Kim, M. Y., Lim, Y. L. and Kwon, S. O. (2016). Effect of Function-Enhanced Mesenchymal Stem Cells Infected With Decorin-Expressing Adenovirus on Hepatic Fibrosis. *Stem Cells Transl. Med.* 5, 1247–1256.

29. Jeong, J., Mao, J., Tenzen, T., Kottmann, A. H. and McMahon, A. P. (2004). Hedgehog signaling in the neural crest cells regulates the patterning and growth of facial primordia. *Genes Dev.* 18, 937–951.
30. Jing, H., Liao, L., An, Y., Su, X., Liu, S., Shuai, Y., Zhang, X. and Jin, Y. (2016). Suppression of EZH2 Prevents the Shift of Osteoporotic MSC Fate to Adipocyte and Enhances Bone Formation During Osteoporosis. *Mol. Ther.* 24, 217–229.
31. Kawane, T., Qin, X., Jiang, Q., Miyazaki, T., Komori, H., Yoshida, C. A., Matsuura-Kawata, V. K. dos S., Sakane, C., Matsuo, Y., Nagai, K., et al. (2018). Runx2 is required for the proliferation of osteoblast progenitors and induces proliferation by regulating Fgfr2 and Fgfr3. *Sci. Rep.* 8, 13551.
32. Kim, J., Lo, L., Dormand, E. and Anderson, D. J. (2003). SOX10 Maintains Multipotency and Inhibits Neuronal Differentiation of Neural Crest Stem Cells. *Neuron* 38, 17–31.
33. Kim, S. Y., Paylor, S. W., Magnuson, T. and Schumacher, A. (2006). Juxtaposed Polycomb complexes co-regulate vertebral identity. *Development* 133, 4957–4968.
34. Kim, H., Langohr, I. M., Faisal, M., McNulty, M., Thorn, C. and Kim, J. (2018). Ablation of Ezh2 in neural crest cells leads to aberrant enteric nervous system development in mice. *PLoS ONE* 13, e0203391.
35. Komori, T. (2009). Osteoimmunology, Interactions of the Immune and skeletal systems II. *Adv. Exp. Med. Biol.* 658, 43–49.
36. Lamandé, S. R., Mörgelin, M., Adams, N. E., Selan, C. and Allen, J. M. (2006). The C5 domain of the collagen VI alpha3(VI) chain is critical for extracellular microfibril

- formation and is present in the extracellular matrix of cultured cells. *J. Biol. Chem.* 281, 16607–14.
37. Lee, M. S., Lowe, G., Flanagan, S., Kuchler, K. and Glackin, C. A. (2000). Human dermo-1 has attributes similar to twist in early bone development. *Bone* 27, 591–602.
38. Lindsay, E. A., Botta, A., Jurecic, V., Carattini-Rivera, S., Cheah, Y.-C., Rosenblatt, H. M., Bradley, A. and Baldini, A. (1999). Congenital heart disease in mice deficient for the DiGeorge syndrome region. *Nature* 401, 379–383.
39. Lindsay, E. A., Vitelli, F., Su, H., Morishima, M., Huynh, T., Pramparo, T., Jurecic, V., Ogunrinu, G., Sutherland, H. F., Scambler, P. J., et al. (2001). Tbx1 haploinsufficiency in the DiGeorge syndrome region causes aortic arch defects in mice. *Nature* 410, 97–101.
40. Liu, Y., Strecker, S., Wang, L., Kronenberg, M. S., Wang, W., Rowe, D. W. and Maye, P. (2013). Osterix-Cre Labeled Progenitor Cells Contribute to the Formation and Maintenance of the Bone Marrow Stroma. *PLoS ONE* 8, e71318.
41. Liu, W., Zhang, L., Xuan, K., Hu, C., Liu, S., Liao, L., Li, B., Jin, F., Shi, S. and Jin, Y. (2018). Alpl prevents bone ageing sensitivity by specifically regulating senescence and differentiation in mesenchymal stem cells. *Bone Res.* 6, 27.
42. Luo, L., Ambrozkiwicz, M. C., Benseler, F., Chen, C., Dumontier, E., Falkner, S., Furlanis, E., Gomez, A. M., Hoshina, N., Huang, W.-H., et al. (2020). Optimizing Nervous System-Specific Gene Targeting with Cre Driver Lines: Prevalence of Germline Recombination and Influencing Factors. *Neuron* 106, 37-65.e5.
43. Maczkowiak, F., Matéos, S., Wang, E., Roche, D., Harland, R. and Monsoro-Burq, A. H. (2010). The Pax3 and Pax7 paralogs cooperate in neural and neural crest

- patterning using distinct molecular mechanisms, in *Xenopus laevis* embryos. *Dev. Biol.* 340, 381–396.
44. Margueron, R. and Reinberg, D. (2011). The Polycomb complex PRC2 and its mark in life. *Nature* 469, 343–349.
45. Matsuoka, T., Ahlberg, P. E., Kessar, N., Iannarelli, P., Dennehy, U., Richardson, W. D., McMahon, A. P. and Koentges, G. (2004). Neural crest origins of the neck and shoulder. *Nature* 436, 347–55.
46. Mendez, M. G., Kojima, S. and Goldman, R. D. (2010). Vimentin induces changes in cell shape, motility, and adhesion during the epithelial to mesenchymal transition. *FASEB J.* 24, 1838–1851.
47. Metzis, V., Courtney, A. D., Kerr, M. C., Ferguson, C., Galeano, M. C. R., Parton, R. G., Wainwright, B. J. and Wicking, C. (2013). Patched1 is required in neural crest cells for the prevention of orofacial clefts. *Hum. Mol. Genet.* 22, 5026–5035.
48. Minoux, M. and Rijli, F. M. (2010). Molecular mechanisms of cranial neural crest cell migration and patterning in craniofacial development. *Development* 137, 2605–2621.
49. Mirzamohammadi, F., Papaioannou, G., Inloes, J. B., Rankin, E. B., Xie, H., Schipani, E., Orkin, S. H. and Kobayashi, T. (2016). Polycomb repressive complex 2 regulates skeletal growth by suppressing Wnt and TGF- β signalling. *Nat. Commun.* 7, 12047.
50. Montgomery, N. D., Yee, D., Montgomery, S. A. and Magnuson, T. (2007). Molecular and Functional Mapping of EED Motifs Required for PRC2-Dependent Histone Methylation. *J. Mol. Biol.* 374, 1145–1157.

51. Mori-Akiyama, Y., Akiyama, H., Rowitch, D. H. and Crombrugge, B. de (2003). Sox9 is required for determination of the chondrogenic cell lineage in the cranial neural crest. *Proc. Natl. Acad. Sci.* 100, 9360–9365.
52. Nakamura, T., Gulick, J., Colbert, M. C. and Robbins, J. (2009). Protein tyrosine phosphatase activity in the neural crest is essential for normal heart and skull development. *Proc. Natl. Acad. Sci.* 106, 11270–11275.
53. Niethamer, T. K., Teng, T., Franco, M., Du, Y. X., Percival, C. J. and Bush, J. O. (2020). Aberrant cell segregation in the craniofacial primordium and the emergence of facial dysmorphology in craniofrontonasal syndrome. *PLoS Genet.* 16, e1008300.
54. O'Carroll, D., Erhardt, S., Pagani, M., Barton, S. C., Surani, M. A. and Jenuwein, T. (2001). The polycomb-group gene Ezh2 is required for early mouse development. *Mol. Cell. Biol.* 21, 4330–6.
55. Pasini, D., Bracken, A. P., Jensen, M. R., Denchi, E. L. and Helin, K. (2004). Suz12 is essential for mouse development and for EZH2 histone methyltransferase activity. *EMBO J.* 23, 4061–4071.
56. Piunti, A. and Shilatifard, A. (2021). The roles of Polycomb repressive complexes in mammalian development and cancer. *Nat. Rev. Mol. Cell Biol.* 22, 326–345.
57. Rigueur, D. and Lyons, K. M. (2013). Skeletal Development and Repair, Methods and Protocols. *Methods Mol. Biol.* 1130, 113–121.
58. Rotllant, J., Liu, D., Yan, Y.-L., Postlethwait, J. H., Westerfield, M. and Du, S.-J. (2008). Sparc (Osteonectin) functions in morphogenesis of the pharyngeal skeleton and inner ear. *Matrix Biol.* 27, 561–572.

59. Sandell, L., Inman, K. and Trainor, P. (2018). DAPI Staining of Whole-Mount Mouse Embryos or Fetal Organs. *Cold Spring Harb. Protoc.* 2018, pdb.prot094029.
60. Schumacher, A., Faust, C. and Magnuson, T. (1996). Positional cloning of a global regulator of anterior–posterior patterning in mice. *Nature* 383, 250–253.
61. Schwarz, D., Varum, S., Zemke, M., Schöler, A., Baggiolini, A., Draganova, K., Koseki, H., Schübeler, D. and Sommer, L. (2014). Ezh2 is required for neural crest-derived cartilage and bone formation. *Development* 141, 867–877.
62. Shukunami, C., Takimoto, A., Oro, M. and Hiraki, Y. (2006). Scleraxis positively regulates the expression of tenomodulin, a differentiation marker of tenocytes. *Dev. Biol.* 298, 234–247.
63. Shull, L. C., Sen, R., Menzel, J., Goyama, S., Kurokawa, M. and Artinger, K. B. (2020). The conserved and divergent roles of Prdm3 and Prdm16 in zebrafish and mouse craniofacial development. *Dev. Biol.* 461, 132–144.
64. Simões-Costa, M. and Bronner, M. E. (2015). Establishing neural crest identity: a gene regulatory recipe. *Development* 142, 242–257.
65. Smits, P., Li, P., Mandel, J., Zhang, Z., Deng, J. M., Behringer, R. R., Crombrughe, B. de and Lefebvre, V. (2001). The Transcription Factors L-Sox5 and Sox6 Are Essential for Cartilage Formation. *Dev. Cell* 1, 277–290.
66. Spellicy, C. J., Peng, Y., Olewiler, L., Cathey, S. S., Rogers, R. C., Bartholomew, D., Johnson, J., Alexov, E., Lee, J. A., Friez, M. J., et al. (2019). Three additional patients with EED-associated overgrowth: potential mutation hotspots identified? *J. Hum. Genet.* 64, 561–572.

67. Tamamura, Y., Katsube, K., Mera, H., Itokazu, M. and Wakitani, S. (2017). *Irx3* and *Bmp2* regulate mouse mesenchymal cell chondrogenic differentiation in both a *Sox9*-dependent and -independent manner. *J. Cell. Physiol.* 232, 3317–3336.
68. Tan, Z., Kong, M., Wen, S., Tsang, K. Y., Niu, B., Hartmann, C., Chan, D., Hui, C. and Cheah, K. S. E. (2020). *IRX3* and *IRX5* Inhibit Adipogenic Differentiation of Hypertrophic Chondrocytes and Promote Osteogenesis. *J. Bone Miner. Res.* 35, 2444–2457.
69. Tatton-Brown, K., Murray, A., Hanks, S., Douglas, J., Armstrong, R., Banka, S., Bird, L. M., Clericuzio, C. L., Cormier-Daire, V., Cushing, T., et al. (2013). Weaver syndrome and *EZH2* mutations: Clarifying the clinical phenotype. *Am. J. Méd. Genet. Part A* 161, 2972–2980.
70. Tien, C.-L., Jones, A., Wang, H., Gerigk, M., Nozell, S. and Chang, C. (2015). *Snail2/Slug* cooperates with Polycomb repressive complex 2 (PRC2) to regulate neural crest development. *Development* 142, 722–731.
71. Ting, M.-C., Wu, N. L., Roybal, P. G., Sun, J., Liu, L., Yen, Y. and Maxson, R. E. (2009). *EphA4* as an effector of *Twist1* in the guidance of osteogenic precursor cells during calvarial bone growth and in craniosynostosis. *Development* 136, 855–864.
72. Yan, Y.-L., Miller, C. T., Nissen, R. M., Singer, A., Liu, D., Kirn, A., Draper, B., Willoughby, J., Morcos, P. A., Amsterdam, A., et al. (2002). A zebrafish *sox9* gene required for cartilage morphogenesis. *Dev. (Camb., Engl.)* 129, 5065–79.
73. Yu, M., Riva, L., Xie, H., Schindler, Y., Moran, T. B., Cheng, Y., Yu, D., Hardison, R., Weiss, M. J., Orkin, S. H., et al. (2009).

CHAPTER 3

Epigenetic reprogramming shapes the cellular landscape of schwannoma

Introduction

Cancer is a heterogeneous disease, and the evolution of cell states and cell types in the tumor microenvironment can influence response to treatment¹⁻⁵. Peripheral nervous system Schwann cells develop from the neural crest⁶, a multipotent embryonic cell population characterized by remarkable molecular and functional diversity⁷. Schwannoma tumors have a low burden of somatic mutations that do not change after treatment with ionizing radiation^{8,9}, but schwannomas that are treated with radiotherapy periodically swell and shrink for many years^{10,11}. In clinical practice, symptomatic schwannoma oscillations are treated with empiric immunosuppressive corticosteroids or surgical decompression, and preoperative schwannoma growth is associated with immune cell infiltration^{12,13}. Here we test the hypothesis that epigenetic mechanisms shape schwannoma cell states and the immune microenvironment during schwannoma responses to radiotherapy. To do so, I collaborated with Dr. John Liu, MD, PhD (J.L.) and Dr. David Raleigh, MD, PhD who conceived of this study and wrote this manuscript. J.L. interrogated human schwannomas, primary patient-derived schwannoma cells, and Schwann and schwannoma cell lines using bulk and single-cell bioinformatics, functional genomic, proteomic, metabolomic, and mechanistic approaches. J.L. found schwannomas are comprised of 2 molecular groups that are distinguished by tumor and immune cell types and can arise de novo (Fig. 1) but undergo epigenetic interconversion in response to radiotherapy (Fig. 2). I conducted a genome-wide CRISPR interference

(CRISPRi) screen¹⁵ and identified epigenetic regulators driving schwannoma cell reprogramming and immune cell infiltration in response to ionizing radiation (Fig. 3). We co-developed a technique integrating single-nuclei ATAC, RNA, and CRISPRi perturbation sequencing and elucidates concordant chromatin accessibility, transcription factor activity, and gene expression programs underlying schwannoma cell state evolution that are conserved in human tumors (Fig. 4). In sum, these data shed light on the molecular landscape of schwannomas and reveal epigenetic mechanisms underlying tumor heterogeneity and response to radiotherapy (Fig. 5).

Methods

Cell culture and treatments

Human Schwann cells (HSC, ScienCell Research Laboratories #1700) and Mouse Schwann Cells (MSC, ScienCell Research Laboratories #M1700-57) were cultured in complete Schwann Cell Medium on Poly- L-Lysine coated substrates (ScienCell Research Laboratories, #1701). HEI-193 schwannoma cells were a gift from Marco Giovannini and cultured in Dulbecco's Modified Eagle Medium (Gibco, #11960069) supplemented with 10% fetal bovine serum (FBS) (Life Technologies, #16141), glutamine (Thermo Fisher Scientific, #10378016)³⁸. HEK-293T cells were a gift from Luke Gilbert and cultured in Dulbecco's Modified Eagle Medium (Gibco, #11960069) supplemented with 10% fetal bovine serum (FBS) (Life Technologies, #16141). Cell cultures were authenticated by STR analysis at the UC Berkeley DNA Sequencing Facility, as well as routinely tested for mycoplasma using the MycoAlert Detection Kit (Lonza, #75866-212). Subconfluent HSC and HEI-193 schwannoma cells were irradiated with an X-Rad 320

(Precision X-Ray) irradiator using a 320 KV output at a rate of 3 Gy/min, with rotating a platform supporting cell culture plates. Cells were quantified by manual hemocytometer during routine cell culture passaging. Crystal violet staining of HEI-193 cells was quantified with background subtraction using ImageJ⁷⁴. For ciliation and Hedgehog signaling assays, cultures were transitioned to OptiMEM (Thermo Fisher Scientific, #31985062) and treated with recombinant Sonic Hedgehog 1 µg/ml (1845, R&D Systems, Minneapolis, MN) or vehicle control for 24 h. Subconfluent HSC cultures in 96 well plates were treated with vismodegib (Genentech) for 72 h, and cell proliferation was assayed on a GloMax Discovery plate reader (Promega, #PAGM3000) using the CellTiter 96 Non-Radioactive Cell Proliferation kit (Promega, #G4100). For proteomic mass spectrometry, cells were grown in serum-free N5 media consisting of Neurobasal A (Life Technologies, #10888022) supplemented with N2 (Gemini Bio-Products, #400-163) and B27 supplements without vitamin A (Gibco, #12587010), L-glutamine 2 mM, antibiotic-antimycotic (Thermo Fisher Scientific, #15240112), bFGF 20 ng/mL (VWR, #119-126), and human EGF 20 ng/mL (Pepro- Tech, #AF-100-15). Cells were irradiated, and cell-free conditioned media was isolated by centrifugation for 10 min at 4000g and filtering through a 0.45 µm syringe for mass spectrometry. TUNEL assays for apoptosis were performed using the APO-BrdU TUNEL Assay Kit with Alexa Fluor 488 Anti-BrdU (Thermo Fisher Scientific, #A23210).

CRISPR interference

HEI-193 schwannoma cells stably expressing the CRISPRi components dCas9-KRAB were generated as previously described^{14,40}. HEI-193 schwannoma cells were transduced with lentivirus harboring SFFV-dCas9-BFP-KRAB, and the top ~25% of cells

expressing BFP were FACS sorted and expanded. For single gene targeted knockdowns, sgRNA protospacer sequences (Supplementary Data 11) were cloned into a lentiviral expression vector (U6-sgRNA EF1Alpha-puro-T2A- BFP) by annealing and ligation. HEI-193 schwannoma CRISPRi cells were then transduced with sgRNA lentivirus and selected with puromycin 1 µg/mL for at least 4 days before experimentation.

Lymphocyte isolation and migration

Peripheral blood lymphocytes were isolated from the human blood of healthy volunteers⁷⁶. A Polymorph density gradient (Accurate Chemical & Scientific Corporation, #AN221725) was used to isolate peripheral blood mononuclear cells that were subsequently selected and differentiated into T cell lymphocytes in Roswell Park Memorial Institute 1640 media (Life Technologies, #11875093) supplemented with 10% FBS, 1% penicillin/streptomycin, phytohemagglutinin 1 µg/ml (10576015, Thermo Fisher Scientific) and recombinant human IL-2 20ng/ml (202-IL, R&D Systems). The QCM Leukocyte Migration Assay (MilliporeSigma, # ECM557) and a GloMax Discovery plate reader (Promega, #PAGM3000) were used to quantify transwell T cell lymphocyte migration from the apical chamber over 4 h at 37 °C. Unconditioned HEI-193 media served as a negative control, unconditioned HEI-193 media supplemented with recombinant human CCL21 600 ng/ml (366-6C, R&D Systems) served as a positive control, HEI-193 media 5 days after 12.5 Gy in 1 fraction, or HEI-193 media without radiation were placed in the basolateral chamber. All conditions were free from serum or other supplements unless specifically indicated.

Quantitative polymerase chain reaction

RNA was isolated using the RNEasy Mini Kit (Qiagen, #74106) and a QiaCube (Qiagen, #9001292), and cDNA was synthesized using the iScript cDNA Synthesis Kit (Bio-Rad, #1708891) and a ProFlex thermocycler (Thermo Fisher Scientific, #4484073). Target genes were amplified using PowerUp SYBR Green Master Mix (Thermo Fisher Scientific, #A25741) and a QuantStudio 6 thermocycler (Thermo Fisher Scientific, #4485691). Gene expression was calculated using the $\Delta\Delta C_t$ method for candidate genes, with normalization to GAPDH (Supplementary Data 11).

Single-nuclei RNA sequencing and analysis

Flash-frozen archived schwannoma specimens were minced with sterile Bard-Parker #10 surgical scalpels (Aspen Surgical, #4–410) and mechanically dissociated with a Pestle Tissue Grinder (size A, Thomas Scientific, #3431E45) in ice-cold lysis buffer consisting of 0.32 M sucrose, 5 mM CaCl₂, 3 mM MgAc₂, 0.1 mM EDTA, 10 mM Tris-HCl, 1 mM DTT and 0.1% Triton X-100 in DEPC-treated water⁹⁰. A sucrose solution consisting of 1.8 M sucrose, 3 mM MgAc₂, 1 mM DTT, and 10 mM Tris-HCl in DEPC-treated water was added to the bottom of the lysis solution in ultracentrifuge tubes (Beckman Coulter) to form a gradient, which was ultracentrifuged at 107,000g for 2.5 h at 4 °C. Nuclei pellets were resuspended in phosphate-buffered saline and sequentially filtered twice in 30 µm strainers (Miltenyi Biotec, #130-098-458). Isolated nuclei were assessed with DAPI staining and loaded onto a 10× Chromium controller using the Chromium Single Cell 3' Library & Gel Bead Kit v2 (10× Genomics). Library sequencing and preprocessing for single nuclei were performed as described above for single-cell libraries, except that a pre-mRNA reference library (GRCh38), including intronic segments, was used for read alignment and quantification. Nuclei libraries with greater

than 400 unique genes were detected, and fewer than 5% of reads attributed to mitochondrial transcripts were retained. To integrate single-nuclei and single-cell RNA sequencing data, all libraries passing respective QC filters described above were combined in silico and normalized with variance stabilization using SCTransform in Seurat version 3.0, with UMI count, percent of reads aligned to mitochondrial transcripts, and technique (single-cell versus single-nuclei) as covariates⁸⁸. Principal component analysis was performed, and single nuclei and single-cell data were harmonized using Harmony in Seurat version 3.0 using technique and day-of tumor isolation as covariates. Clustering and marker identification was performed as described above for single cell-only analysis, with parameters $\text{min.dist} = 0.3$ and $\text{resolution} = 0.3$.

CRISPR interference genome-wide screening

CRISPRi screens were performed as described previously^{14,15}. HEI-193 cells stably expressing CRISPRi components (dCas9-KRAB) were transduced with lentivirus supernatant containing the third-generation dual sgRNA CRISPRi library, which targets 20,528 genes and 1025 sgNTC¹⁵. Screens were performed in triplicate cultures with coverage of at least 500× cells per construct. sgRNA-expressing cells were selected using puromycin (1 $\mu\text{m}/\text{mL}$) for 48 h and transferred to puromycin-free normal growth media for 48 h to allow recovery. Initial (T0) cell populations were then frozen in 10% DMSO and processed for genomic DNA alongside endpoint (T12) cell populations, which corresponded to 7.82 population doublings. Triplicate screens were also performed with radiotherapy (1.8 Gy \times 5 fractions) delivered daily starting on T0, with the endpoints (T12) corresponding to 3.46 population doublings. Genomic DNA was harvested using the NucleoSpin Blood L Kit (Machery-Nagel, #740954.20) for each cell population, and

sgRNA cassettes were amplified using 22 cycles of PCR using NEBNext Ultra II Q5 PCR MasterMix (New England Biolabs, #M0544L). Sequencing was performed on a NovaSeq 6000 (Illumina) using custom sequencing primers¹⁵. sgRNA read counts were aligned using custom Python scripts derived from the ScreenProcessing package¹⁵, without allowing mismatches. sgRNA counts with discordant target genes from the same vector, representative of vector recombination, or fewer than 100 reads detected in the T0 populations, were discarded from downstream analysis. Growth phenotype (γ) was defined as $\log_2(\text{sgRNA count T12}/\text{sgRNA count T0})$ minus median sgNTC $\log_2(\text{sgRNA count T12}/\text{sgRNA count T0})$ as previously described¹⁴. Radiation phenotype (ρ) was defined as $\log_2(\text{sgRNA count T12 (1.8 Gy} \times 5)/\text{sgRNA count T12 (0 Gy)})$. Statistical significance was quantified using a two-sided Student's t-test comparing replicate distributions of library-normalized counts for each sgRNA between conditions (ρ) or time points (γ). A discriminant threshold of 5, derived from the product of normalized gene-phenotype and $-\log_{10}(\text{p-value})$, corresponding to an empiric false discovery rate of $\sim 1\%$, was selected for hit definitions¹⁴. To ascertain the fidelity of our screens, we overlapped all negative growth hits from our screen (without radiotherapy treatment) with common essential genes from DepMap⁹¹ and found that 591 out of 918 total negative growth hits (64.4%) were also DepMap essential genes. The reproducibility of our screens was assessed by calculating the Pearson correlation coefficients of the screen hit phenotypes, which demonstrated a median R of 0.829 for no radiotherapy and 0.760 for radiotherapy conditions.

Single-nuclei ATAC, RNA, and CRISPRi perturbation sequencing (snARC-seq)

Genetic perturbations in snARC-seq rely on the CROP-seq vector (Addgene, pBA950)⁹⁴, which allows for the capture of sgRNA identity from nuclear RNA transcripts. This design permits single sgRNA perturbations, and therefore we designed 2 independent sgRNA vectors per target gene, corresponding to each of the dual sgRNAs that targeted hit genes from the genome-wide CRISPRi V3 library¹⁵. Oligonucleotides containing protospacer sequences (Supplementary Data 11) were ordered as a pool from Twist Bioscience and PCR amplified as described above. The oligonucleotide pool was ligated into the CROP-seq backbone using BstXI and BlnI digestion and T4 ligation. Library representation, including sgNTC overrepresentation, was performed on a MiSeq run to ensure sgRNA uniformity. The cloned library was packaged into lentivirus using HEK-293T cells. HEI-193 cultures were transduced to an MOI of 0.1, and FACS sorted for sgRNA+ cells after 48 h. Radiotherapy was then delivered to either 0 Gy or 1.8 Gy × 5 daily fractions using the X-Rad 320 irradiator (Precision X-Ray). Following completion of radiotherapy, cells were harvested with Trypsin and prepared following the Nuclei Isolation for Single Cell Multiome ATAC + Gene Expression Sequencing 10× Protocol (10× Genomics, CG000365 Rev C). Briefly, 1–2 × 10⁵ cells were incubated in chilled Lysis Buffer (Tris-HCl (pH 7.4) 10 mM, NaCl 10 mM, MgCl₂ 3 mM, Tween-20 0.1%, Nonidet P40 Substitute 0.1%, Digitonin 0.01%, BSA 1%, DTT 1mM, RNase inhibitor 1 U/μL) on ice for 4 min, washed with Wash Buffer (Tris-HCl (pH 7.4) 10 mM, NaCl 10 mM, MgCl₂ 3 mM, Tween-20 0.1%, BSA 1%, DTT 1 mM, RNase inhibitor 1 U/uL) 3 times, and resuspended in diluted nuclei buffer. Nuclei were counted, and membrane integrity was evaluated by Trypan staining on the Countess II FL Automated Cell Counter (Thermo,

#TF-CACC2FL). Nuclei suspensions were diluted to approximately 3000 nuclei/ μ L and processed according to the 10 \times Chromium Next GEM Single Cell Multiome ATAC + Gene Expression protocol (CG000338 Rev A). To recover sgRNA identities from single-nuclei RNA fractions, CROP-seq guides were amplified into dual-indexed Illumina libraries from the cDNA product of the 10 \times multiome protocol as described above with a three-round heminested PCR as previously described⁹⁵. Totally, 15 ng of full-length cDNA product was amplified with primers binding to the sgRNA constant region and 10 \times Genomics Read 1 Adapter. Two subsequent PCR steps were performed to introduce i5 and i7 indices and Illumina P5 and P7 adapters. After the first round of PCR, each product was size-selected using SPRI beads at 1.0 \times . Subsequent PCRs were conducted with 1 ng product. The final PCR product was size selected with 0.5 \times , and then 1.0 \times SPRI beads, and library quality was assessed by TapeStation high-sensitivity D1000 analysis (Thermo, #5067-5584). CROP-seq libraries were pooled with gene expression libraries and sequenced on an Illumina NovaSeq 6000 using the paired-end 100 bp protocol. Library demultiplexing, read alignment to human genome GRCh38, and UMI quantification for the RNA and ATAC fractions were performed using Cell Ranger ARC version 2.0.1 (10 \times Genomics). CROP-seq sgRNAs were detected using kallisto bustools (v0.24.1)⁹⁶. First, a sgRNA reference was built using kb ref with a k-mer size of 15 which was used as a reference for kb count. The sgRNA enrichment PCR sequences were then pseudo-aligned to this index using kallisto bustools, including the ARC multiome Gene Expression Whitelist version 1 (10 \times Genomics). For each cell barcode group, sgRNAs with less than 6 UMIs were filtered, and sgRNAs were assigned to cells using Geomux (v0.2.1)⁵⁴ ([https:// github.com/noamteyssier/geomux](https://github.com/noamteyssier/geomux)), which performs a hypergeometric test for

each cell on its observed guide counts, then calculates a log₂- odds ratio between the two highest counts. Cells were assigned to their majority guide if their Benjamini–Hochberg corrected P value was below 0.05, the log-odds ratio was above 1, and the total number of UMIs was greater than 6. The resulting sgRNA assignments were used to determine cell barcode groups with a single detected sgRNA. Preprocessing of single-nuclei RNA and ATAC data was performed using Signac v1.8.0⁹⁷. Cells containing the following quality measures were retained: ATAC UMI between 1000 and 100,000, RNA UMI between 50 and 25,000, nucleosome signal <4, and TSS enrichment >1. TAC peak calling was performed using the MACS2 wrapper in Signac. Peaks were processed using term frequency-inverse document frequency (TF-IDF) normalization and singular value decomposition. RNA counts were normalized, and variance was stabilized by SCTransform using default parameters. ATAC UMAP projection was calculated using the latent semantic indexing reduction dimensions 2–30. RNA UMAP projection was calculated using principal component analysis dimensions 1:20, which was empirically determined using ElbowPlot. Louvain clustering for either ATAC or RNA data was performed using a resolution parameter of 0.5. Gene activity scores from the ATAC signal were generated by quantifying ATAC UMIs mapped to the promoter of each gene, defined as between the TSS and 2000 bp upstream of the TSS for each gene. To score gene activity changes of gene modules between radiotherapy and control conditions, gene activity scores were calculated for marker genes derived from Louvain clustering of human schwannoma cell types (Fig. 1b) and HEI-193 schwannoma cell states (Fig. 2c), as described above. Expression and gene activity were then pseudobulked according to the target gene and therefore included cells with either of the two targeting sgRNAs. The

top ten most specific cluster markers were used for each cell type or cell state, and the mean pseudobulk gene activity of these markers was obtained for each on-target sgRNA as well as for sgNTC cells, in each radiotherapy condition. sgRNA phenotypes were then log₂ transformed, and the gene activity vector in radiotherapy (1.8 Gy × 5) conditions were subtracted by those in control conditions (0 Gy). These fold changes were clustered using hierarchical clustering with Pearson correlation and complete linkage. Transcription factor motif deviations in the setting of genetic or therapeutic perturbations were quantified using the ChromVAR⁵⁹ wrapper in Signac with default parameters against the peaks assay. Mean motif deviations for each sgRNA identity in each condition were quantified and subsetted to only motifs whose cognate transcription factors were expressed in HEI-193 cells using RNA sequencing data, as described above. To estimate the differential motif deviations for a given sgRNA perturbation in radiotherapy conditions versus control conditions, deviations were log₂ transformed, and deviations in radiotherapy conditions were subtracted by those in control conditions. To further quantify chromatin accessibility at motif regions as a consequence of epigenetic regulator snARC-seq perturbations, differentially accessible regions were determined using the FindMarkers function in Signac using logistic regression. Differentially accessible regions were further subsetted by those whose nearest neighbor gene was associated with ChIP-seq peaks derived from the ENCODE project (KLF13 accession ENCF453MMH, SETDB1 accession ENCF773RNU). Average ATAC profiles were obtained for each sgRNA condition at these restricted sets of differentially accessible regions with a window ±1000 bp and then normalized to the average read depth at 100 bps at each end flank of the distributions.

Results

Schwannomas are comprised of neural crest and immune enriched epigenetic groups and radiation is sufficient for epigenetic reprogramming between groups.

Dr. John Liu (J.L.) conducted DNA methylation profiling on vestibular schwannomas from patients at UCSF and discovered differentially methylated probes comprising two molecular groups: genes involved in nervous system development or immunologic signaling (Fig. 5). RNA sequencing and differential expression analysis on 11 neural crest and 13 immune-enriched schwannomas integrated with DNA methylation profiling revealed enrichment and hypomethylation of either neural crest genes and Hedgehog target genes or immune genes and apolipoprotein genes across the 2 molecular groups of schwannomas. To define cell types comprising schwannoma molecular groups, J.L. performed single-nuclei or single-cell RNA sequencing on neural crest or immune enriched schwannomas and found schwannoma cluster cell states reflective of nerve injury and regeneration, or immune signatures indicative of processes like macrophage migration and axon repair. J.L. defined immune cell types using CyTOF analysis and found an enrichment of myeloid derived macrophages and lymphoid cells in immune enriched schwannomas compared to neural crest schwannomas. J.L. found that schwannomas with prior radiotherapy favored immune characteristics and underwent an epigenetic reprogramming from immune-enriched to neural crest upon treatment with radiotherapy. Hierarchical clustering of differentially methylated DNA probes distinguishing schwannomas with prior radiotherapy showed hypomethylation of immune genes and hypermethylation of neuronal progenitor maintenance genes. The *NF2*

deficient schwannoma cell line HEI193 was employed and treated with ionizing radiation to assess epigenetic transformation of these cells. Indeed, schwannoma cell expression of inflammatory factors like apolipoprotein was enriched in the radiated cells. To better define how schwannoma cell states respond to radiotherapy, J.L. used Perturb-seq in radiated HEI193 cells and found that genetic perturbations caused heterogeneous changes in gene module expression with or without ionizing radiation. Therefore, I hypothesized other genomic and epigenomic mechanisms responded to radiation to define schwannoma cell states. The following data presented is a product of my close collaboration with John Liu and was exclusively conducted in the Raleigh lab.

Epigenetic regulators reprogram schwannoma cells and drive immune cell infiltration in response to radiotherapy

To more broadly define genomic drivers specifying schwannoma cell states in response to ionizing radiation, triplicate genome-wide CRISPRi screens were performed using dual sgRNA libraries comprised of 20,528 targeted sgRNAs and 1025 sgNTCs¹⁵ (Fig. 6a). The effect of genetic perturbations on HEI-193 schwannoma cell growth \pm radiotherapy was defined by quantifying the relative DNA abundance of all sgRNAs in each sample using sequencing of integrated barcodes. Gene set enrichment analysis of radiotherapy sensitivity screen hits showed expected enrichment of cell cycle and DNA repair, but also revealed significant enrichment of epigenetic genes (Supplementary Fig. 16a). Examination of screen hits identified 29 epigenetic regulators associated with radiotherapy resistance or sensitivity phenotypes in schwannoma cells (Fig. 6b, c). In support of these findings, CRISPRi suppression of the histone demethylases KDM1A or

KDM5C validated radiotherapy resistance or sensitivity phenotypes, respectively (Fig. 6d,e). Cancer cell death from ionizing radiation leads to acute, transient recruitment of immune cells to the tumor microenvironment⁵¹, but we identified surviving schwannoma cells alongside infiltrating immune cells for many years after treatment of human tumors with radiotherapy (Fig. 6b and Supplementary Fig. 2f, 5c, 12). To determine if schwannoma cell reprogramming contributes to immune cell infiltration of the tumor microenvironment, proteomic mass spectrometry was performed on conditioned media from surviving HEI-193 schwannoma cells after radiotherapy (Supplementary Fig. 17a–c). Ontology analyses of 425 differentially expressed proteins from conditioned media revealed enrichment of apolipoproteins after ionizing radiation (Fig. 6f), and a parallel reaction monitoring targeted assay validated secretion of APOA1 and other chemokines from surviving schwannoma cells (Fig. 6g). Transwell migration assays showed conditioned media from schwannoma cells recruited primary human peripheral blood lymphocytes after radiotherapy (Supplementary Fig. 16c), and conditioned media from schwannoma cells with CRISPRi suppression of the radio-therapy resistance hit KDM1A enhanced lymphocyte migration (Fig. 6h). In contrast, conditioned media from schwannoma cells with CRISPRi suppression of APOA1 or the radiotherapy sensitivity hit KDM5C inhibited lymphocyte migration (Fig. 6h and Supplementary Fig. 16b). Thus, epigenetic mechanisms in schwannoma cells contribute to immune cell infiltration in response to radiotherapy. To determine if altered expression of epigenetic regulators mediates schwannoma responses to radiotherapy, we analyzed the 29 epigenetic hits from our genome-wide CRISPRi screen (Fig. 6b, c) across schwannoma cell types and schwannoma cell states. Surprisingly, no epigenetic regulators were differentially

expressed across either context, either with or without radiotherapy (Supplementary Data 4,7). Epigenetic regulator activity is dependent on metabolite cofactors that covalently modify histone subunits⁵². Thus, we hypothesized schwannoma cell metabolites may be altered in response to radiotherapy. To test this, we performed targeted metabolite profiling of HEI-193 cells after control, fractionated radiotherapy, or hypo- fractionated radiotherapy treatments using liquid chromatography mass spectrometry. Radiotherapy suppressed the KDM5C cofactor α - ketoglutarate and succinic acid, a biproduct of α -ketoglutarate metabolism (Fig. 6i). α -ketoglutarate was also suppressed by radiotherapy in primary schwannoma cells from 7 patients (Supplementary Fig. 17d). Moreover, radiotherapy suppressed the KDM1A cofactor flavin adenine dinucleotide (FAD) and increased the KDM5C cofactor ascorbic acid (Fig. 6i). RNA sequencing showed IDH1/2 and MDH1/2, which produce α - ketoglutarate or succinic acid, respectively, were suppressed following schwannoma cell radiotherapy (Fig. 6j). DHCR7, which metabolizes ascorbic acid precursors⁵³, was also suppressed after radiotherapy, but the nudix hydrolases NUTD1/4/14, which degrade FAD, were increased (Fig. 6j). These data suggest altered expression of metabolic enzymes and metabolite cofactors may influence epigenetic regulator activity during schwannoma radiotherapy responses.

Single-nuclei ATAC, RNA, and CRISPRi perturbation sequencing identifies integrated genomic mechanisms driving schwannoma cell state evolution

To define how epigenetic regulators shape chromatin accessibility and gene expression in schwannoma cells during tumor evolution, we developed a technique for simultaneous interrogation of chromatin accessibility and gene expression coupled with genetic and therapeutic perturbations in single-nuclei (Fig. 7a). Single-nuclei ATAC, RNA,

and CRISPRi perturbation sequencing (snARC-seq) of the 29 epigenetic regulator hits from our genome-wide CRISPRi screen (Fig. 6b, c) was performed in HEI-193 cells with control or radiotherapy treatments (Supplementary Fig. 18a). sgRNA identities were assigned to individual cells using a hypergeometric test⁵⁴ (Supplementary Fig. 18b, c). Genome-wide ATAC signals were enriched at transcription start sites and 5' nucleosome free regions⁵⁵ (Supplementary Fig. 18d). ATAC and RNA sequencing data exhibited heterogenous distributions in UMAP space⁵⁶ (Fig. 4b). Together, these data support successful simultaneous profiling of 3 genomic modalities in single-nuclei with or without radiotherapy (Fig. 7a). To determine if snARC-seq suppression of chromatin regulators reprograms the epigenetic landscape of schwannoma cells, we quantified gene activity scores for open chromatin regions nearby marker genes distinguishing schwannoma cell states or cell types. Differential gene activity scores clustered according to gene ontologies of perturbed epigenetic regulators (e.g., histone demethylases, histone acetyltransferases) and CRISPRi screen phenotypes (radiotherapy sensitivity, negative rho; radiotherapy resistance, positive rho) (Fig. 7c). For instance, snARC-seq suppression of the elongator acetyltransferase complex component ELP6 attenuated interferon signaling and ER stress schwannoma cell states that were normally activated by radiotherapy consistent with the role of the elongator acetyltransferase complex in gene activation and sensitivity to genotoxic stress^{57,58}. To elucidate transcription factors underlying changes in gene expression programs with snARC-seq suppression of chromatin regulators, we scored transcription factor motif deviation with or without radiotherapy⁵⁹ (Fig. 7d). Restricting analysis to transcription factors in HEI-193 cells revealed heterogenous disruptions in chromatin accessibility that clustered based on

CRISPRi screen phenotypes (Fig. 7d). snARC-seq suppression of the radiotherapy sensitivity hit KDM5C caused enrichment of open chromatin regions at KLF13 motifs with radiotherapy (Fig. 7e), and KLF13 target genes such as DDI2 and PTPA were simultaneously accessible at their genomic loci and had enriched RNA expression in single-nuclei following snARC-seq suppression of KDM5C with radiotherapy (Supplementary Fig. 18e). ITIH4, a secreted protein that was enriched in conditioned media from schwannoma cells surviving radiotherapy (Fig. 6g), displayed closed chromatin and RNA suppression following snARC-seq suppression of KDM5C with radiotherapy (Supplementary Fig. 18e). Concordant changes in KLF13 gene activity were not observed following snARC-seq suppression of the radiotherapy resistance hit KDM1A with radiotherapy (Fig. 7e), consistent with opposing phenotypes of KDM1A and KDM5C in mediating schwannoma radiotherapy responses (Fig. 6c). snARC-seq suppression of the histone methyltransferase SETDB1 increased accessibility at TCF3 motifs and expression of TCF3 target genes (Fig. 7e) such as RNF217, FOXO1, and RAD23B with radiotherapy (Supplementary Fig. 18e). Integrated single-nuclei and single-cell RNA sequencing showed TCF3 target genes were expressed in schwannoma cells from human tumors (Fig. 4f), and schwannoma clustering restricted to RNA sequencing of TCF3 target genes recapitulated neural crest and immune-enriched molecular groups of schwannomas (Fig. 7g). Thus, our snARC-seq technique for simultaneous interrogation of chromatin accessibility and gene expression coupled with genetic and therapeutic perturbations in single-nuclei reveals epigenetic dependences underlying radiotherapy responses in schwannomas cells that are conserved across molecular groups of human tumors.

Discussion

Mutational and non-mutational mechanisms are critical for cancer evolution^{5,60}. Schwannomas are the most common tumors of the peripheral nervous system and have a remarkably low burden of somatic mutations that is not increased by radiotherapy^{8,9,61}. Thus, schwannomas represent prototypical tumors for understanding epigenetic mechanisms specifying tumor cell states, tumor heterogeneity, and response to therapy. Our results reveal schwannomas are comprised of neural crest and immune-enriched molecular groups that are distinguished by schwannoma and immune cell types, and that radiotherapy is sufficient for epigenetic reprogramming of neural crest schwannomas to immune-enriched schwannomas (Fig. 5). By integrating multiplatform profiling of human tumors with multiomic functional genomic approaches, we show interconversion of schwannoma molecular groups, cell types, and cell states in response to radiotherapy, a treatment that is used for half of cancer patients worldwide⁶². Future studies will be needed to determine if the epigenetic mechanisms we report are relevant to other treatment modalities or tumorigenesis. Intriguingly, patients in our study with autoimmune diseases and severe allergies were more likely to have immune-enriched schwannomas than neural crest schwannomas (25.7% vs 0%, $p = 0.0025$, Fischer's exact test) (Fig. 1a and Supplementary Data 1), suggesting systemic factors may also influence the epigenetic architecture of cancer. To that end, we establish a framework for investigating how tumor evolution and responses to treatment are modulated by epigenetic reprogramming. This paradigm is bolstered by an innovative method for simultaneous profiling of epigenetic and transcriptional cell states coupled with genetic and therapeutic

perturbations in single-nuclei (snARC-seq), a technique that may enable new discoveries in health and disease.

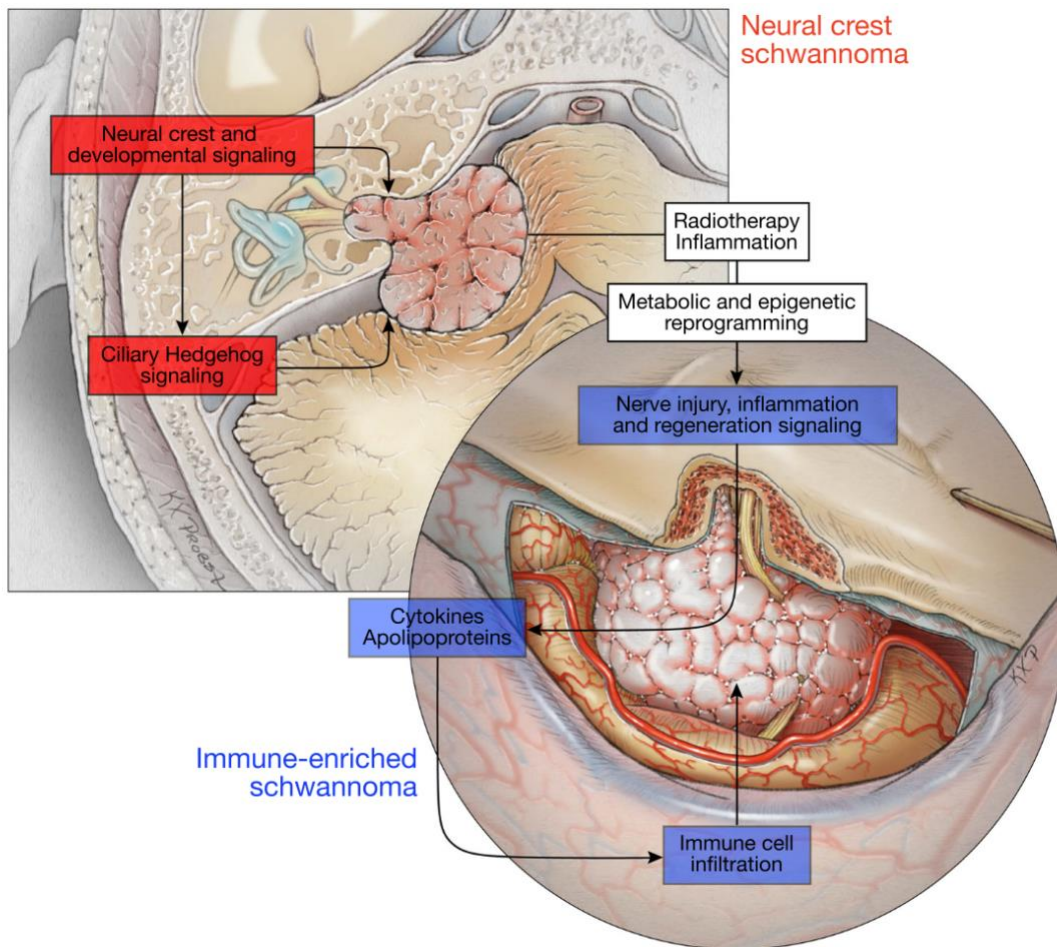


Fig. 5 | An integrated model of schwannoma tumorigenesis and epigenetic reprogramming in response to treatment. Two molecular groups of schwannoma, neural crest schwannoma and immune-enriched schwannoma, are driven by distinct mechanisms. Radiotherapy can induce immune-enriched schwannoma through metabolic and epigenetic reprogramming.

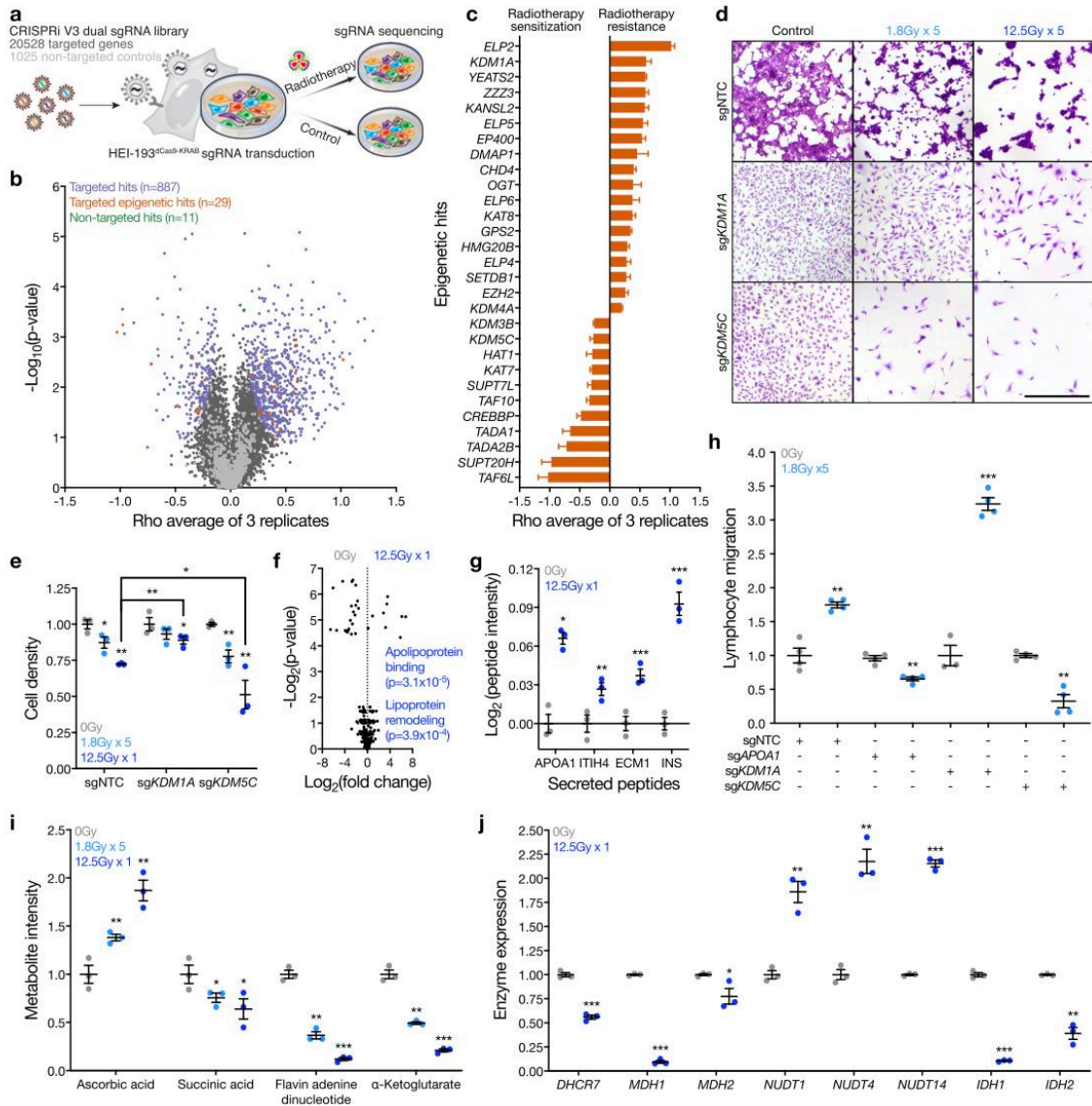


Fig. 6 Epigenetic regulators reprogram schwannoma cells and drive immune cell infiltration in response to radiotherapy. a Experimental workflow for genome-wide CRISPRi screens using dual sgRNA libraries comprised of 20,528 targeted sgRNAs and 1025 non-targeted control sgRNAs (sgNTC). Libraries were transduced into HEI-193 cells that were subsequently treated with 0 Gy or 1.8 Gy × 5 radiotherapy (n = 3 per condition). sgRNA barcodes were sequenced and quantified as proxies for cell enrichment or depletion. b CRISPRi screen results showing the average rho log₂(sgRNA in radiotherapy conditions/sgRNA in control conditions) and two-sided Student's t-test p values across three replicates.

Figure caption continued on the next page.

Figure caption continued from the previous page.

On-target hit genes (purple), epigenetic regulator hit genes (orange), and sgNTCs called hits (green) at a false discovery rate of 1% are shown. c Rho phenotypes of epigenetic regulator CRISPRi screen hits genes from (b). n = 3 replicate screens. d Crystal violet staining of HEI-193 following CRISPRi of KDM1A or KDM5C compared to sgNTC after treatment with 0 Gy, 1.8 Gy × 5, or 12.5 Gy × 1 of radiotherapy. Scale bar, 100 μm. e Quantification of cell density from (d) (n = 3 independent cultures, two-sided Student's t-test). f Volcano plot of 425 peptides identified using proteomic mass spectrometry of conditioned media from triplicate HEI-193 cultures after radiotherapy or control treatment. Significant gene ontology terms of enriched peptides after radiotherapy conditions annotated (two-sided Fisher's exact test). g Proteomic mass spectrometry parallel reaction monitoring targeted assay validating secreted peptide enrichment in conditioned media from HEI-193 after radiotherapy (n = 3 independent cultures, two-sided Student's t-test) as in (f). h Transwell primary human peripheral blood lymphocyte migration assays using conditioned media from HEI-193 (n = 3 independent cultures, two-sided Student's t-test) following CRISPRi suppression of APOA1, KDM1A, or KDM5C ± radiotherapy as a chemoattractant. i Targeted metabolite mass spectrometry of HEI-193 after treatment with 0 Gy, 1.8 Gy × 5, or 12.5 Gy × 1 of radiotherapy (n = 3 independent cultures per condition, two-sided Student's t-test). Fold changes normalized to 0 Gy treatment for each metabolite. j Metabolic enzymes gene expression changes from bulk RNA sequencing of HEI-193 cells ± radiotherapy (n = 3 independent cultures) (Supplementary Data 6). Fold changes normalized to 0 Gy treatment for each gene. Lines represent means, and error bars represent standard error of means (two-sided Student's t-tests, *p ≤ 0.05, **p ≤ 0.01, ***p ≤ 0.0001). Source data are provided as a Source Data file.

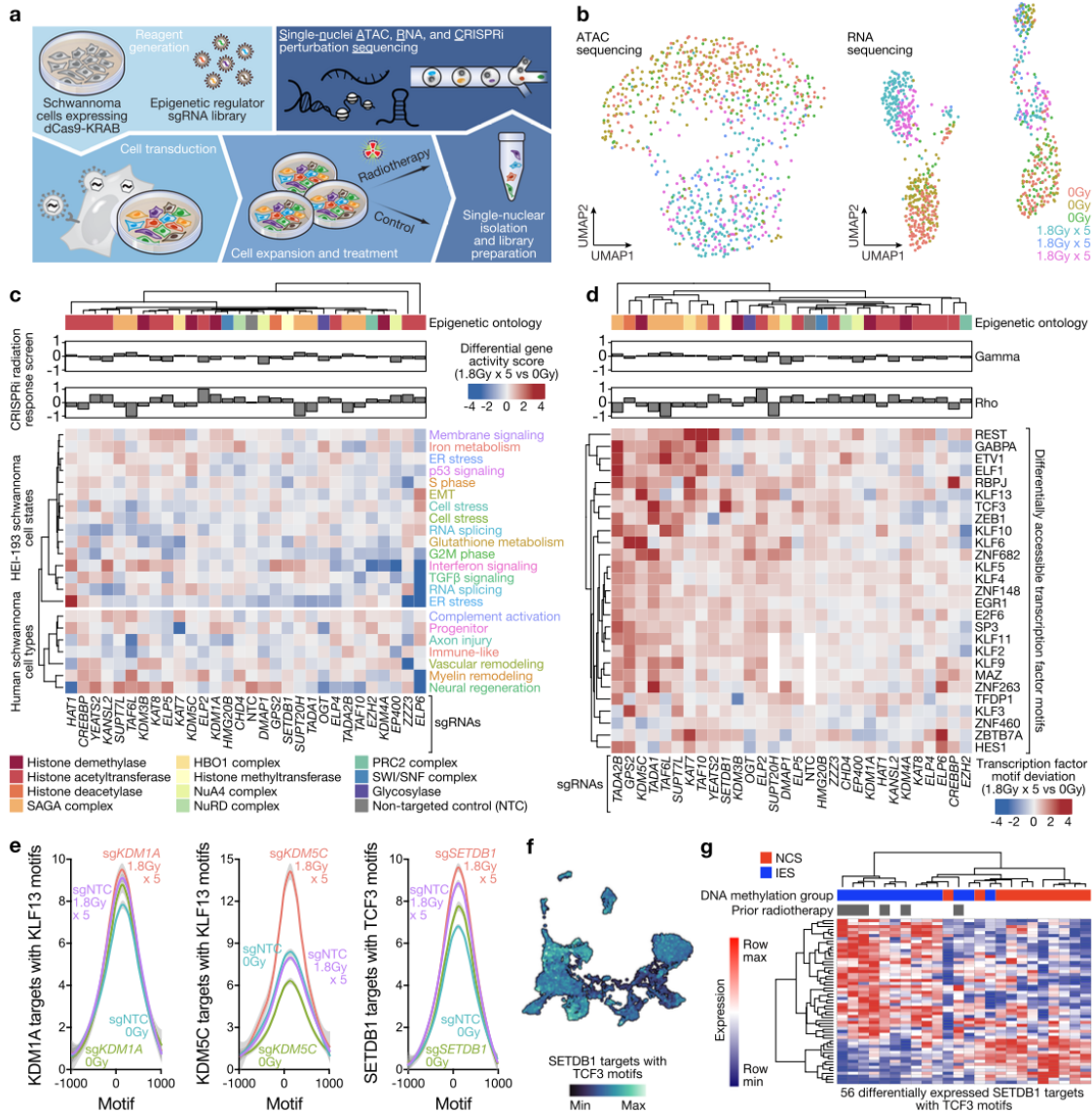


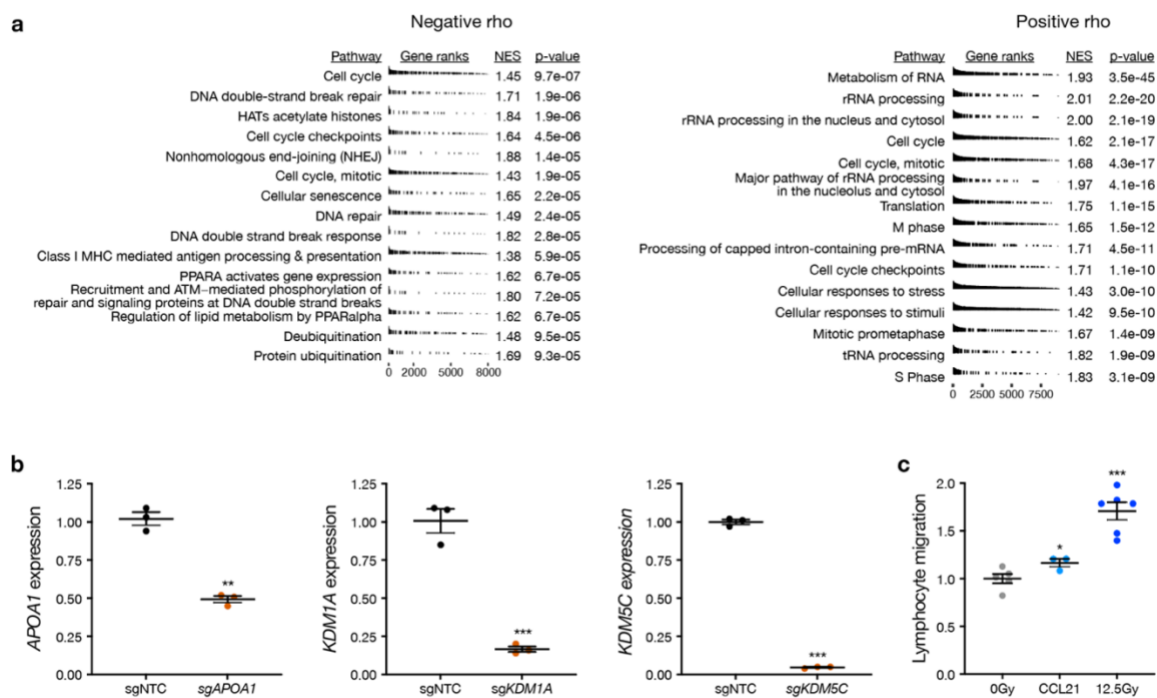
Fig. 7 Single-nuclei ATAC, RNA, and CRISPRi perturbation sequencing identify integrated genomic mechanisms driving schwannoma cell state evolution.

a Experimental workflow for single-nuclei ATAC, RNA, and CRISPRi perturbation sequencing (snARC-seq). Triplicate HEI-193 cultures were transduced with sgRNA libraries targeting 29 epigenetic regulators driving radiotherapy responses from genome-wide CRISPRi screens (Fig. 3c) and treated with 0 Gy or 1.8 Gy \times 5 of radiotherapy prior to isolation of single-nuclei for sequencing. sgRNA identities were recovered from CROP-seq tags in single-nuclei RNA sequencing data. b UMAPs of ATAC (left) or RNA (right) sequencing of 855 single nuclei passing snARC-seq quality control from triplicate control or radiotherapy conditions (Supplementary Fig. 18). c Hierarchical clustering of differential gene activity scores between radiotherapy and control conditions for each snARC-seq perturbation (columns). Gene activity modules (rows) were derived from HEI-193 schwannoma cell states \pm radiotherapy (Fig. 2c) or from human schwannoma cell types (Fig. 1b).

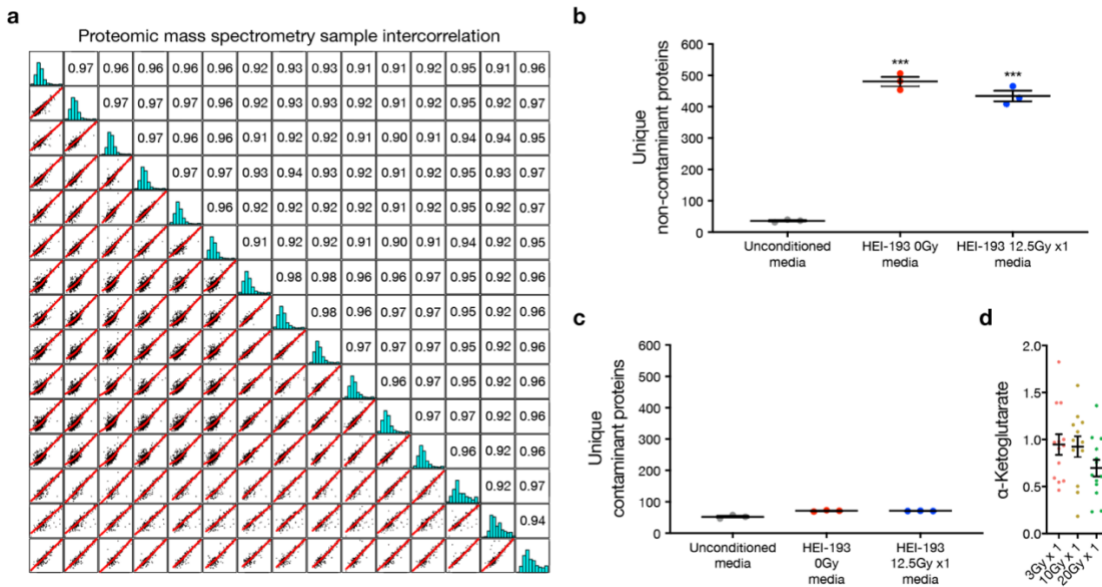
Figure caption continued on the next page.

Figure caption continued from the previous page.

Gene ontology of perturbed epigenetic regulators and CRISPRi screen growth (γ) or radiation response (ρ) phenotypes from genome-wide CRISPRi screens (Fig. 3c) are shown. d Hierarchical clustering of differential ChromVAR transcription factor motif deviations between radiotherapy and control conditions for each snARC-seq perturbation (columns). e Average profile plots of normalized ATAC signal at KLF13 or TCF3 motifs with ENCODE ChIP-seq peak annotations and differential accessibility following snARC-seq perturbation of KDM1A, KDM5C, or SETDB1. f Feature plot of integrated UMAP from harmonized schwannoma single- nuclei and single-cell RNA sequencing (Fig. 1b) showing genes near TCF3 motifs that are differentially accessible following SETDB1 snARC-seq perturbation. g Hierarchical clustering of human schwannoma RNA sequencing profiles using 56 differentially expressed SETDB1 targets with TCF3 motifs showing separation of NCS and IES molecular groups of schwannomas. Source data are provided as a Source Data file.



Supplementary Fig. 8 Genome-wide CRISPRi screens reveal regulators of schwannoma cell radiotherapy responses. a, Gene set enrichment analysis of ranked gene targets exhibiting negative rho (left, radiotherapy sensitivity) or positive rho (right, radiotherapy resistance) following CRISPRi gene suppression. Gene ontology terms derived from Reactome. NES, normalized enrichment score. b, CRISPRi suppression of APOA1, KDM1A, or KDM5C in HEI-193 cells (n=3 independent cultures, **p=0.00042 sgAPOA1, ***p=0.00047 sgKDM1A, p=4.33x10⁻⁷ sgKDM5C). c, Transwell primary human peripheral blood lymphocyte migration assays using conditioned media from HEI-193 cells ± radiotherapy or with recombinant CCL21 as a chemoattractant (*p=0.033, ***p=0.000125). Lines represent means and error bars represent standard error of means. (Two-sided Student's t tests used). Source data are provided as a Source Data file.



Supplementary Fig. 9. Proteomic and targeted metabolic mass spectrometry of schwannoma cells. a, Proteomic mass spectrometry Pearson correlation matrix from HSC and HEI-193 media demonstrating high correlation across samples. b and c, Unique non-contaminant or contaminant protein counts from HEI-193 media mass spectrometry (n=3 independent cultures, Two-sided Student's t tests, ***p=8.17x10⁻⁶ 0Gy, p=1.94x10⁻⁵ 12.5Gy). d, Metabolite mass spectrometry of primary patient-derived human schwannoma cells (n=7 patient samples) after treatment with 3Gy x 1, 10Gy x 1, or 20Gy x 1 of radiotherapy validated suppression of α Ketoglutarate with ionizing radiation (Fig. 3i). Fold changes normalized to 0Gy treatment for each primary cell culture (ANOVA, p \leq 0.05). Lines represent means and error bars represent standard error of means. Source data are provided as a Source Data file.

References

1. Dagogo-Jack, I. & Shaw, A. T. Tumour heterogeneity and resistance to cancer therapies. *Nat. Rev. Clin. Oncol.* 15, 81–94 (2018).
2. Greaves, M. Evolutionary determinants of cancer. *Cancer Discov.* 5, 806–820 (2015).
3. Levine, A. J., Jenkins, N. A. & Copeland, N. G. The roles of initiating truncal mutations in human cancers: the order of mutations and tumor cell type matters. *Cancer Cell* 35, 10–15 (2019).
4. McGranahan, N. & Swanton, C. Clonal heterogeneity and tumor evolution: past, present, and the future. *Cell* 168, 613–628 (2017).
5. Nowell, P. C. The clonal evolution of tumor cell populations. *Science* 194, 23–28 (1976).
6. Vasudevan, H. N., Lucas, C.-H. G., Villanueva-Meyer, J. E., Theodosopoulos, P. V. & Raleigh, D. R. Genetic events and signaling mechanisms underlying Schwann cell fate in development and cancer *Neurosurgery* 88, nyaa455- (2020).
7. Simoes-Costa, M. & Bronner, M. E. Establishing neural crest identity: a gene regulatory recipe. *Development* 142, 242–257 (2015).
8. Agnihotri, S. et al. The genomic landscape of schwannoma. *Nat. Genet.* 48, 1339–1348 (2016).
9. Håvik, A. L. et al. Genetic landscape of sporadic vestibular schwannoma. *J. Neurosurg.* 128, 911–922 (2018).
10. Breshears, J. D. et al. Temporal dynamics of pseudoprogression after gamma knife radiosurgery for vestibular schwannomas—a retrospective volumetric study. *Neurosurgery* 84, 123–131 (2019).

11. Régis, J., Delsanti, C. & Roche, P.-H. Editorial: vestibular schwannoma radiosurgery: progression or pseudoprogression? *J. Neuro- surg.* 127, 374–379 (2016).\
12. Lewis, D. et al. Inflammation and vascular permeability correlate with growth in sporadic vestibular schwannoma. *Neurooncology* 21, 314–325 (2018).
13. Hannan, C. J. et al. The inflammatory microenvironment in vestib- ular schwannoma. *Neurooncol. Adv.* 2, vdaa023 (2020).
14. Gilbert, L. A. et al. Genome-scale CRISPR-mediated control of gene repression and activation. *Cell* 159, 647–661 (2014).
15. Replogle, J. M. et al. Maximizing CRISPRi efficacy and accessibility with dual-sgRNA libraries and optimal effectors. *eLife* 11, e81856 (2022).
16. Capper, D. et al. DNA methylation-based classification of central nervous system tumours. *Nature* 555, 469–474 (2018).
17. Choudhury, A. et al. Meningioma DNA methylation groups identify biological drivers and therapeutic vulnerabilities. *Nat. Genet.* 54, 649–659 (2022).
18. Rada-Iglesias, A. et al. Epigenomic annotation of enhancers pre- dicts transcriptional regulators of human neural crest. *Cell Stem Cell* 11, 633–648 (2012).
19. Lachmann, A. et al. ChEA: transcription factor regulation inferred from integrating genome-wide CHIP-X experiments. *Bioinformatics* 26, 2438–2444 (2010).
20. Korsunsky, I. et al. Fast, sensitive and accurate integration of single- cell data with Harmony. *Nat. Methods* 16, 1289–1296 (2019)
21. Hung, H. A., Sun, G., Keles, S. & Svaren, J. Dynamic regulation of Schwann cell enhancers after peripheral nerve injury. *J. Biol. Chem.* 290, 6937–6950 (2015)

22. Chen, Z.-L., Yu, W.-M. & Strickland, S. Peripheral regeneration. *Annu. Rev. Neurosci.* 30, 209–233 (2007).
23. Ohta, S. et al. Macrophage migration inhibitory factor (MIF) promotes cell survival and proliferation of neural stem/progenitor cells. *J. Cell Sci.* 125, 3210–3220 (2012).
24. Zhu, Z. et al. Macrophage migration inhibitory factor promotes chemotaxis of astrocytes through regulation of cholesterol 25-hydroxylase following rat spinal cord injury. *Neuroscience* 408, 349–360 (2019).
25. Zhu, D., Hunter, S. B., Vertino, P. M. & Meir, E. G. V. Overexpression of MBD2 in glioblastoma maintains epigenetic silencing and inhibits the antiangiogenic function of the tumor suppressor gene BAI1. *Cancer Res.* 71, 5859–5870 (2011).
26. Cayé-Thomasen, P. et al. VEGF and VEGF receptor-1 concentration in vestibular schwannoma homogenates correlates to tumor growth rate. *Otol. Neurotol.* 26, 98–101 (2005).
27. Aust, G., Zhu, D., Meir, E. G. V. & Xu, L. Adhesion G protein-coupled receptors, molecular, physiological and pharmacological principles in health and disease. *Handb. Exp. Pharm.* 234, 369–396 (2016).
28. Taylor, A. M. et al. Axonal mRNA in uninjured and regenerating cortical mammalian axons. *J. Neurosci.* 29, 4697–4707 (2009).
29. Spitzer, M. H. et al. An interactive reference framework for modeling a dynamic immune system. *Science* 349, 1259425 (2015).
30. Levine, J. H. et al. Data-driven phenotypic dissection of AML reveals progenitor-like cells that correlate with prognosis. *Cell* 162, 184–197 (2015).

31. Li, C. et al. Tumor-associated macrophages: potential therapeutic strategies and future prospects in cancer. *J. Immunother. Cancer* 9, e001341 (2021).
32. Liu, S. et al. Molecular and clinical characterization of CD163 expression via large-scale analysis in glioma. *Oncoimmunology* 8,
33. Debacker, J. M., Gondry, O., Lahoutte, T., Keyaerts, M. & Huvenne, W. The prognostic value of CD206 in solid malignancies: a systematic review and meta-analysis. *Cancers* 13, 3422 (2021).
34. Hamann, D. et al. Phenotypic and functional separation of memory and effector human CD8⁺T cells. *J. Exp. Med.* 186, 1407–1418 (1997).
35. Kamphorst, A. O. et al. Proliferation of PD-1⁺CD8 T cells in peripheral blood after PD-1-targeted therapy in lung cancer patients. *Proc. Natl Acad. Sci. USA* 114, 4993–4998 (2017).
36. Mesman, S., Bakker, R. & Smidt, M. P. Tcf4 is required for correct brain development during embryogenesis. *Mol. Cell Neurosci.* 106, 103502 (2020).
37. Raleigh, D. R. & Reiter, J. F. Misactivation of Hedgehog signaling causes inherited and sporadic cancers. *J. Clin. Invest.* 129, 465–475 (2019).
38. Hung, G. et al. Establishment of primary vestibular schwannoma cultures from neurofibromatosis type-2 patients. *Int J. Oncol.* 14, 409–415 (1999).
39. Hung, G. et al. Establishment and characterization of a schwannoma cell line from a patient with neurofibromatosis 2. *Int. J. Oncol.* <https://doi.org/10.3892/ijo.20.3.475> (2002).
40. Gilbert, L. A. et al. CRISPR-mediated modular RNA-guided regulation of transcription in eukaryotes. *Cell* 154, 442–451 (2013).

41. Robert, A. et al. The intraflagellar transport component IFT88/ polaris is a centrosomal protein regulating G1-S transition in non-ciliated cells. *J. Cell Sci.* 120, 628–637 (2007).
42. Delaval, B., Bright, A., Lawson, N. D. & Doxsey, S. The cilia protein IFT88 is required for spindle orientation in mitosis. *Nat. Cell Biol.* 13,461–468 (2011).
43. Zamanian-Daryoush, M. et al. The cardioprotective protein apolipoprotein A1 promotes potent anti-tumorigenic effects* ♦. *J. Biol. Chem.* 288, 21237–21252 (2013).
44. Bonacina, F. et al. Myeloid apolipoprotein E controls dendritic cell antigen presentation and T cell activation. *Nat. Commun.* 9, 3083 (2018).
45. Avraham, R. & Yarden, Y. Feedback regulation of EGFR signalling: decision making by early and delayed loops. *Nat. Rev. Mol. Cell Biol.* 12, 104–117 (2011).
46. Stolt, C. C. et al. SoxD proteins influence multiple stages of oligo- dendrocyte development and modulate SoxE Protein function. *Dev. Cell* 11, 697–709 (2006).
47. Replogle, J. M. et al. Mapping information-rich genotype-phenotype landscapes with genome-scale Perturb-seq. *Cell* 185, 2559–2575.e28 (2022).
48. Dixit, A. et al. Perturb-Seq: dissecting molecular circuits with scalable single-cell RNA profiling of pooled genetic screens. *Cell* 167, 1853–1866.e17 (2016).
49. Adamson, B. et al. A multiplexed single-cell CRISPR screening platform enables systematic dissection of the unfolded protein response. *Cell* 167, 1867–1882.e21 (2016).
50. Bouyain, S. & Watkins, D. J. The protein tyrosine phosphatases PTPRZ and PTPRG bind to distinct members of the contactin family of neural recognition molecules. *Proc. Natl Acad. Sci. USA* 107, 2443–2448 (2010).

51. Sangiuliano, B., Pérez, N. M., Moreira, D. F. & Belizário, J. E. Cell death-associated molecular-pattern molecules: inflammatory signaling and control. *Mediat. Inflamm.* 2014, 821043 (2014).
52. Berger, S. L. & Sassone-Corsi, P. Metabolic signaling to chromatin. *Cold Spring Harb. Perspect. Biol.* 8, a019463 (2016).
53. Russell, D. W. The enzymes, regulation, and genetics of bile acid synthesis. *Annu. Rev. Biochem.* 72, 137–174 (2003).
54. Cooper, Y. A. et al. Functional regulatory variants implicate distinct transcriptional networks in dementia. *Science* 377, eabi8654 (2022).
55. Jiang, C. & Pugh, B. F. Nucleosome positioning and gene regulation: advances through genomics. *Nat. Rev. Genet.* 10, 161–172 (2009).
56. Vallejos, C. A., Risso, D., Scialdone, A., Dudoit, S. & Marioni, J. C. Normalizing single-cell RNA sequencing data: challenges and opportunities. *Nat. Methods* 14, 565–571 (2017).
57. Li, Q. et al. The elongator complex interacts with PCNA and modulates transcriptional silencing and sensitivity to DNA damage agents. *PLoS Genet.* 5, e1000684 (2009).
58. Wittschieben, B. Ø. et al. A novel histone acetyltransferase is an integral subunit of elongating RNA polymerase II holoenzyme. *Mol. Cell* 4, 123–128 (1999).
59. Schep, A. N., Wu, B., Buenrostro, J. D. & Greenleaf, W. J. chromVAR: inferring transcription factor-associated accessibility from single-cell epigenomic data. *Nat. Methods* 14, 975–978 (2017).
60. Hanahan, D. Hallmarks of cancer: new dimensions. *Cancer Discov.* 12, 31–46 (2022).

61. Low, J. T. et al. Primary brain and other central nervous system tumors in the United States (2014-2018): a summary of the CBTRUS statistical report for clinicians. *Neurooncology* 9, 165–182 (2022).
62. Gelband, H., Jha, P., Sankaranarayanan, R. & Horton, S. Disease Control Priorities. in Third Edition (Volume 3): Cancer (2015). <https://doi.org/10.1596/978-1-4648-0349-9>.
63. Anaizi, A. N., Gantwerker, E. A., Pensak, M. L. & Theodosopoulos, P. V. Facial nerve preservation surgery for koos grade 3 and 4 vestibular schwannomas. *Neurosurgery* 75, 671–677 (2014).
64. Monfared, A. et al. Facial nerve outcome and tumor control rate as a function of degree of resection in treatment of large acoustic neuromas preliminary report of the Acoustic Neuroma Subtotal Resection Study (ANSRS). *Neurosurgery* 79, 194–203 (2016).
65. Fortin, J.-P., Triche, T. J. & Hansen, K. D. Preprocessing, normalization and integration of the Illumina HumanMethylationEPIC array with minfi. *Bioinformatics* 33, 558–560 (2017).
66. Aryee, M. J. et al. Minfi: a flexible and comprehensive Bioconductor package for the analysis of finium DNA methylation microarrays. *Bioinformatics* 30, 1363–1369 (2014).
67. Fortin, J.-P. et al. Functional normalization of 450k methylation array data improves replication in large cancer studies. *Genome Biol.* 15, 503 (2014).
68. Bibikova, M. et al. High-throughput DNA methylation profiling using universal bead arrays. *Genome Res.* 16, 383–393 (2006).

69. Kuleshov, M. V. et al. Enrichr: a comprehensive gene set enrichment analysis web server 2016 update. *Nucleic Acids Res.* 44, W90–W97 (2016).
70. Rada-Iglesias, A. et al. A unique chromatin signature uncovers early developmental enhancers in humans. *Nature* <https://doi.org/10.1038/nature09692> (2010).
71. Müller, S., Cho, A., Liu, S. J., Lim, D. A. & Diaz, A. CONICS integrates scRNA-seq with DNA sequencing to map gene expression to tumor sub-clones. *Bioinformatics* 34, 3217–3219 (2018).
72. Moss, J. et al. Comprehensive human cell-type methylation atlas reveals origins of circulating cell-free DNA in health and disease. *Nat. Commun.* 9, 5068 (2018).
73. Johann, P. D., Jäger, N., Pfister, S. M. & Sill, M. RF_Purify: a novel tool for comprehensive analysis of tumor-purity in methylation array data based on random forest regression. *BMC Bioinforma.* 20, 428 (2019).
74. Schneider, C. A., Rasband, W. S. & Eliceiri, K. W. NIH Image to ImageJ: 25 years of image analysis. *Nat. Methods* 9, 671–675 (2012).
75. Louis, D. N. et al. The 2016 World Health Organization Classification of tumors of the central nervous system: a summary. *Acta Neuro-pathol.* 131, 803–820 (2016).
75. Cox, J. & Mann, M. MaxQuant enables high peptide identification rates, individualized p.p.b.-range mass accuracies and proteome wide protein quantification. *Nat. Biotechnol.* 26, 1367–1372 (2008).
76. Cox, J. et al. Accurate proteome-wide label-free quantification by delayed normalization and maximal peptide ratio extraction, termed MaxLFQ*. *Mol. Cell Proteom.* 13, 2513–2526 (2014).

77. Choi, M. et al. MSstats: an R package for statistical analysis of quantitative mass spectrometry-based proteomic experiments. *Bioinformatics* 30, 2524–2526 (2014).
78. Vizcaíno, J. A. et al. 2016 update of the PRIDE database and its related tools. *Nucleic Acids Res.* 44, D447–D456 (2016).
79. MacLean, B. et al. Skyline: an open source document editor for creating and analyzing targeted proteomics experiments. *Bioinformatics* 26, 966–968 (2010).
80. Sharma, V. et al. Panorama public: a public repository for quantitative data sets processed in skyline*. *Mol. Cell Proteom.* 17, 1239–1244 (2018).
81. Schularick, N. M., Clark, J. J. & Hansen, M. R. Primary culture of human vestibular schwannomas. *J. Vis. Exp.* <https://doi.org/10.3791/51093> (2014).
82. Kim, D., Langmead, B. & Salzberg, S. L. HISAT: a fast spliced aligner with low memory requirements. *Nat. Methods* 12, 357–360 (2015).
83. Liao, Y., Smyth, G. K. & Shi, W. featureCounts: an efficient general purpose program for assigning sequence reads to genomic features. *Bioinformatics* 30, 923–930 (2014).
84. Love, M. I., Huber, W. & Anders, S. Moderated estimation of fold change and dispersion for RNA-seq data with DESeq2. *Genome Biol.* 15, 550 (2014).
85. Stuart, T. et al. Comprehensive integration of single-cell data. *Cell* 177, 1888–1902.e21 (2019).
86. Liberzon, A. et al. The molecular signatures database hallmark gene set collection. *Cell Syst.* 1, 417–425 (2015).
87. Velmeshev, D. et al. Single-cell genomics identifies cell type-specific molecular changes in autism. *Science* 364, 685–689 (2019).

88. Meyers, R. M. et al. Computational correction of copy number effect improves specificity of CRISPR-Cas9 essentiality screens in cancer cells. *Nat. Genet.* 49, 1779–1784 (2017).
89. Horlbeck, M. A. et al. Compact and highly active next-generation libraries for CRISPR-mediated gene repression and activation. *eLife* 5, 914 (2016).
90. Replogle, J. M. et al. Combinatorial single-cell CRISPR screens by direct guide RNA capture and targeted sequencing. *Nat. Biotechnol.* 38, 954–961 (2020).
91. Datlinger, P. et al. Pooled CRISPR screening with single-cell transcriptome readout. *Nat. Methods* 14, 297–301 (2017).
92. Tian, R. et al. CRISPR interference based platform for multimodal genetic screens in human iPSC-derived neurons. *Neuron* 104, 239–255.e12 (2019).
93. Melsted, P. et al. Modular, efficient and constant memory single cell RNA-seq preprocessing. *Nat. Biotechnol.* 39, 813–818 (2021).
94. Stuart, T., Srivastava, A., Madad, S., Lareau, C. A. & Satija, R. Single-cell chromatin state analysis with Signac. *Nat. Methods* 18, 1333–1341 (2021).
95. Cho, N. W. Liu et al. Epigenetic reprogramming shapes the cellular landscape of schwannoma: CyTOF data. *Mendeley Data* <https://doi.org/10.17632/hjmvnf48gh.1> (2023).
96. Liu, S. J. Epigenetic reprogramming shapes the cellular landscape of schwannoma: analysis code. *Code Ocean* <https://doi.org/10.24433/co.0193242.v1> (2023).

Publishing Agreement

It is the policy of the University to encourage open access and broad distribution of all theses, dissertations, and manuscripts. The Graduate Division will facilitate the distribution of UCSF theses, dissertations, and manuscripts to the UCSF Library for open access and distribution. UCSF will make such theses, dissertations, and manuscripts accessible to the public and will take reasonable steps to preserve these works in perpetuity.

I hereby grant the non-exclusive, perpetual right to The Regents of the University of California to reproduce, publicly display, distribute, preserve, and publish copies of my thesis, dissertation, or manuscript in any form or media, now existing or later derived, including access online for teaching, research, and public service purposes.

DocuSigned by:

Timothy Casey-Clyde

97DF2C48BBF0437...

Author Signature

8/12/2024

Date